Aalto University
School of Engineering

Jaakko Esala

Preliminary design of the new Proton Synchrotron Internal Dump core

A thesis submitted in partial fulfillment of the requirements for the degree of Master of Science in Technology.

Prévessin, 27.11.2017
Supervisor: Dr. Luc St-Pierre
Advisor: M.Sc. François-Xavier Nuiry

Aalto University
School of Engineering

Aalto University, P.O. BOX 11000, 00076 AALTO
www.aalto.fi

Abstract of master's thesis

Author Jaakko Esala		
Title of thesis Preliminary design of the new Proton Synchrotron Internal Dump core		
Degree programme Mechanical Engineering		
Major Technical Mechanics		**Code** K3006
Thesis supervisor Dr. Luc St-Pierre		
Thesis advisor M.Sc. François-Xavier Nuiry		
Date 27.11.2017	**Number of pages** 9+70	**Language** English

Abstract

The luminosity of the LHC particle accelerator at CERN is planned to be upgraded in the first half of 2020s, requiring also the upgrade of its injector accelerators, including the Proton Synchrotron (PS). The PS Internal Dumps are beam dumps located in the PS accelerator ring. They are safety devices designed to stop the circulating proton beam in order to protect the accelerator from damage due to an uncontrolled beam loss. The PS Internal Dumps need to be upgraded to be able to withstand the future higher intensity and energy proton beams.

The dump core is a block of material interacting with the beam. It is located in ultra-high vacuum and moved into the beam path in 150 milliseconds by an electromagnet and spring-based actuation mechanism. The circulating proton beam is shaved by the core surface during thousands of beam revolutions.

The preliminary new dump core design weighs 13 kilograms and consists of an isostatically pressed fine-grain graphite and a precipitation hardened copper alloy CuCrZr. The core is cooled by stainless steel water circuits. The mechanical integrity of the core is studied under proton beam impact. The temperatures and stresses induced by specified beam dumping scenarios are simulated with ANSYS finite element software, coupled with heat generation input from FLUKA simulations. The fatigue and radiation damage due to repeated beam impacts is also studied.

The simulated temperatures in the core stay below the material limits and the stresses stay within the elastic regimes, with high safety factors in CuCrZr, but low safety factors in graphite. Graphite fatigue may limit the lifetime of the core. The radiation damage levels in the core materials are considered low. Overall, the preliminary core design fulfills the requirements set and the design can proceed towards prototyping and eventual installation in 2020.

Keywords CERN, Proton Synchrotron, Proton Synchrotron Internal Dump, beam dump, proton beam–matter interaction, finite element analysis, FLUKA to ANSYS coupling

Aalto-yliopisto
Insinööritieteiden
korkeakoulu

Aalto-yliopisto, PL 11000, 00076 AALTO
www.aalto.fi
Diplomityön tiivistelmä

Tekijä Jaakko Esala		
Työn nimi Uuden Proton Synchrotron Internal Dumpin ytimen alustava suunnittelu		
Koulutusohjelma Konetekniikka		
Pääaine Teknillinen mekaniikka		**Koodi** K3006
Työn valvoja TkT Luc St-Pierre		
Työn ohjaaja DI François-Xavier Nuiry		
Päivämäärä 27.11.2017	**Sivumäärä** 9+70	**Kieli** Englanti

Tiivistelmä

CERNin LHC-hiukkaskiihdyttimen luminositeettia aiotaan nostaa 2020-luvun alussa, minkä vuoksi myös LHC:n injektiokiihdyttimet, mukaan lukien Proton Synchrotron (PS), täytyy päivittää. PS Internal Dumpit ovat säteen pysäyttimiä. Ne ovat turvalaitteita, joiden tarkoitus on pysäyttää kiihdyttimessä kiertävä protonisäde ja suojella kiihdytintä säteen kontrolloimattomalta törmäykseltä. PS Internal Dumpit täytyy päivittää, jotta ne kestävät tulevaisuuden intensiivisemmät ja energisemmät protonisäteet.

Pysäyttimen ydin on säteen kanssa vuorovaikuttava pala materiaalia. Se sijaitsee ultratyhjiössä ja sen liikuttaa säteen tielle 150 millisekunnissa elektromagneetista ja jousista koostuva mekanismi. Ytimen pinta höylää protonisädettä sen kiertäessä kiihdyttimessä, pysäytten sen usean tuhannen kierroksen jälkeen.

Alustava ydin painaa 13 kilogrammaa ja koostuu grafiitista ja kuparin lejeeringistä, CuCrZr:sta. Ydintä jäähdytetään teräsputkissa kiertävällä vedellä. Työssä tutkitaan ytimen vastetta protonisäteen törmäykseen. Lämpötila nousua ja jännityksiä ytimessä simulatiodaan määritellyissä säde-skenaarioissa ANSYS-elementtimenetelmäohjelmalla. Lämmöntuontanto syötetään malliin FLUKA ohjelmasta. Myös materiaalin väsymistä ja säteilyvaurioitumista toistuvissa säteen törmäyksissä tutkitaan.

Simuloidut lämpötilat pysyvät materiaalin sallimien lämpötilojen alapuolella ja jännitykset ovat elastisuuden rajoissa. Jännitysten turvakertoimet CuCrZr:ssa ovat korkeat, mutta grafiitissa matalat. Grafiitin väsyminen saattaakin rajoittaa ytimen elinikää. Ydin täyttää pääpiirteittään sille asetetut vaatimukset ja suunnittelu voi jatkua kohti prototyyppiä ja asennusta vuonna 2020.

Avainsanat CERN, Proton Synchrotron, Proton Synchrotron Internal Dump, säteen pysäytin, protonisäde–materiaali vuorovaikutus, elementtimenetelmä-analyysi, FLUKA–ANSYS liitäntä

Preface

This thesis has been written based on the engineering studies I have performed for the new Proton Synchrotron Internal Dump core in the framework of the LHC Injectors Upgrade project at CERN. It was written during my 14 month stay at CERN as a Technical Student in the EN-STI-TCD section.

The supervisor of the thesis is Dr. Luc St-Pierre (Aalto University) and the advisor is M.Sc. François-Xavier Nuiry (CERN). I wish to thank them for their invaluable help and guidance throughout the process. I also wish to extend my thanks to everyone else who has worked with me on the project, especially to my colleagues in EN-MME for the 3D design shown in so many pictures and in EN-STI-FDA for the FLUKA simulations that are the base of my simulations.

Thank you also to all my coworkers in the TCD section for all the help, discussions and good memories.

Kiitos tuesta ja kannustuksesta myös perheelleni, jota olen nähnyt harvoin kirjoittaessani diplomityötäni ulkomailla.

Prévessin, 27.11.2017

Jaakko Esala

Table of Contents

Symbols

A	[m]	Cross sectional area of the cooling circuits
B	[m]	Characteristic length of the thermal diffusion time
E	[GPa]	Young's modulus
E'	[GPa]	Reduced Young's modulus
E_{g}	[GPa]	Young's modulus of graphite
E_0	[MeV]	Rest energy of a proton
E_{beam}	[GeV] or [J]	Energy of a proton beam
E_{kin}	[GeV]	Kinetic energy of a proton
E_{tot}	[GeV]	Total energy of a proton
H	[MPa]	Microhardness
L	[m]	Length of a cooling pipe
N	[protons] or [ppp]	Beam intensity (ppp: protons per pulse)
N_{f}	[-]	Number of cycles to failure
Nu	[-]	Nusselt number
P	[MPa]	Contact pressure
P_{heat}	[W]	Heating power
Pr	[-]	Prandtl number
Q_{v}, Q_{h}	[-]	Vertical and horizontal tune of the accelerator
Q	[l/min]	Volumetric flow rate
R	[-]	Stress ratio in cyclic loading
R_{a}	[µm]	Arithmetic mean surface roughness
R_{RMS}	[µm]	RMS surface roughness
R_{r}	[µm]	Effective RMS surface roughness
Re	[-]	Reynolds number
$\mathrm{SF}_{\mathrm{M–C}}$	[-]	Mohr–Coulomb safety factor
$\mathrm{SF}_{\mathrm{vM}}$	[-]	Von Mises safety factor
T	[°C]	Temperature
T_0	[°C]	Temperature at the beginning of a beam impact
T_1	[°C]	Temperature at the end of a beam impact
T_{i}	[°C]	Water inlet temperature
T_{limit}	[°C]	Temperature limit of the material
T_{m}	[°C]	Mean water temperature
T_{o}	[°C]	Water outlet temperature
T_{ref}	[°C]	Reference temperature
T_{test}	[°C]	Testing temperature
ΔT	[°C]	Temperature change
X_0	[cm]	Radiation length
X_{I}	[cm]	Nuclear interaction length
X, Y, Z	[m]	Cartesian coordinates
a	[mm^2/s]	Thermal diffusivity
c	[m/s]	Speed of light in vacuum
c_0	[m/s]	Speed of sound in material
c_p	[J/(kg K)]	Specific heat
d_{i}	[m]	Inner diameter of a cooling pipe

h_s	[W/(m^2 K)]	Thermal contact conductance (graphite to CuCrZr)
h_w	[W/(m^2 K)]	Heat transfer coefficient (cooling pipe walls to water)
m	[rad]	Mean absolute asperity slope
m_r	[rad]	Effective mean absolute asperity slope
p	[GeV/c]	Beam momentum
q_V	[GeV/cm^3] or [J/m^3]	Energy deposition density or heat generation
$\dot{q}_V$	[GeV/(cm^3 s)] or [W/m^3]	Power deposition density or heat generation rate
t	[s]	Time
t_d	[s]	Thermal diffusion time
w	[m/s]	Mean flow velocity
Δt	[s]	Time step length
Δx	[mm]	Mesh size
α	[1/K]	(Mean) coefficient of thermal expansion
γ	[-]	Intermittency factor between laminar and turbulent flow
δ_{ij}	[-]	Kronecker delta
ε_{ij}	[-]	Total strain tensor components
ε_{ij}^M	[-]	Mechanical strain tensor components
ε_{ij}^T	[-]	Thermal strain tensor components
λ	[W/(m K)]	Thermal conductivity
λ'	[W/(m K)]	Effective thermal conductivity
ν	[-]	Poisson's ratio
ν_visc	[m^2/s]	Kinematic viscosity
ρ	[kg/m^3]	Density
σ_v, σ_h	[mm]	Vertical and horizontal standard deviation of proton Gaussian distribution in a beam
σ_{ij}	[MPa]	Cauchy stress tensor components
σ_C	[MPa]	Compressive strength
σ_T	[MPa]	Tensile strength
σ_vM	[MPa]	Equivalent von Mises stress
σ_y	[MPa]	Von Mises yield strength
σ_1, σ_2, σ_3	[MPa]	Principal stresses, $\sigma_1 > \sigma_2 > \sigma_3$
ψ	[-]	Plasticity index

Abbreviations

2D, 3D	Two-dimensional, three-dimensional
ALICE	A Large Ion Collider Experiment
APDL	ANSYS Parametric Design Language
ATLAS	A Toroidal LHC Apparatus
CERN	European Organization for Nuclear Research
CMS	Compact Muon Solenoid
CTE	Coefficient of Thermal Expansion
CuCrZr	Copper–Chromium–Zirconium
DPA	Displacements Per Atom
EN	Engineering (department at CERN)
FLUKA	Fluktuierende Kaskade
FDA	FLUKA Development and Applications (section at CERN)
HIP	Hot Isostatic Pressing
HL–BCMS	High Luminosity Batch Compression Merging and Splitting
HL–LHC	High Luminosity LHC
Int.	Intensity
LEIR	Low Energy Ion Ring
LIU	LHC Injectors Upgrade
Linac	Linear accelerator
LHC	Large Hadron Collider
LHCb	LHC beauty
MME	Mechanical and Materials Engineering (group at CERN)
PS	Proton Synchrotron
PSB	Proton Synchrotron Booster
RaDIATE	Radiation Damage In Accelerator Target Environments
RMS	Root Mean Square
SFTPRO	SPS Fixed Target Proton
SPS	Super Proton Synchrotron
SS	Straight Section
STI	Sources, Targets and Interactions (group at CERN)
TCC	Thermal Contact Conductance
TCD	Targets, Collimators and Dumps (section at CERN)
TIDVG#4	Target Internal Dump Vertical Graphite #4
TOF	Time of Flight
ppm	Parts per million
ppp	Protons per pulse

1 Introduction

1.1 CERN

CERN is the European Organization for Nuclear Research located in Geneva on the border between France and Switzerland. The organization was founded in 1954 and currently consists of 22 member states. They are mostly from Europe, but there are also numerous collaborating countries and organizations from all over the world. CERN employs over 2500 people and is visited by over 12000 scientists for their research. [1]

The purpose of CERN is to provide for collaboration among European states in scientific nuclear research with no concern in military applications [2]. CERN provides infrastructure for research and education in the field of nuclear and particle physics. A central part of this mission is CERN's particle accelerator complex presented in Figure 1. It consists of multiple accelerators, the most famous of which is the Large Hadron Collider (LHC). It is the world's largest particle accelerator with a circumference of 27 kilometers and it enabled the Nobel-winning discovery of the Higgs boson in 2012 [3].

There are four smaller accelerators that serve as injector accelerators to the LHC. They accelerate the proton beam to intermediate energies before it is injected into the LHC. The accelerators are in order: the Linear Accelerator (Linac2), the Proton Synchrotron Booster (PSB), the Proton Synchrotron (PS), and the Super Proton Synchrotron (SPS), as presented in Figure 1. In addition to serving the LHC, these accelerators also provide beams for the numerous other experiments at CERN. The LHC is also able to accelerate ions. [4]

In the LHC two proton beams are accelerated in opposite directions close to the speed of light and collided in four detectors called ATLAS, CMS, LHCb and ALICE. The detectors record data of the collision events. The number of recorded events is important for obtaining more data and reducing statistical errors [5]. The number of events per unit time is determined by the accelerator's luminosity. Luminosity can be increased by increasing the number of protons in the beam, by increasing the revolution frequency of the beam, or by decreasing the size of the beam. [6]

The LHC has produced collisions since 2009 [3]. Operating the LHC past the year 2020 without upgrading its luminosity would decrease the statistical errors in the existing data relatively little. To exploit the full potential of the LHC its luminosity is planned to be upgraded in the High Luminosity LHC (HL-LHC) project in the first half of the 2020s. [6]

To increase the luminosity in the LHC the injector accelerators also need to be upgraded. The luminosity increase will be achieved by increasing the beam energy, which places more demanding requirements on the accelerator equipment. The LHC Injectors Upgrade (LIU) project aims to upgrade the injector accelerators to be "capable of delivering reliably the beams required by the HL-LHC" [4]. In this framework the Proton Synchrotron presented in Figure 2 also needs to be upgraded.

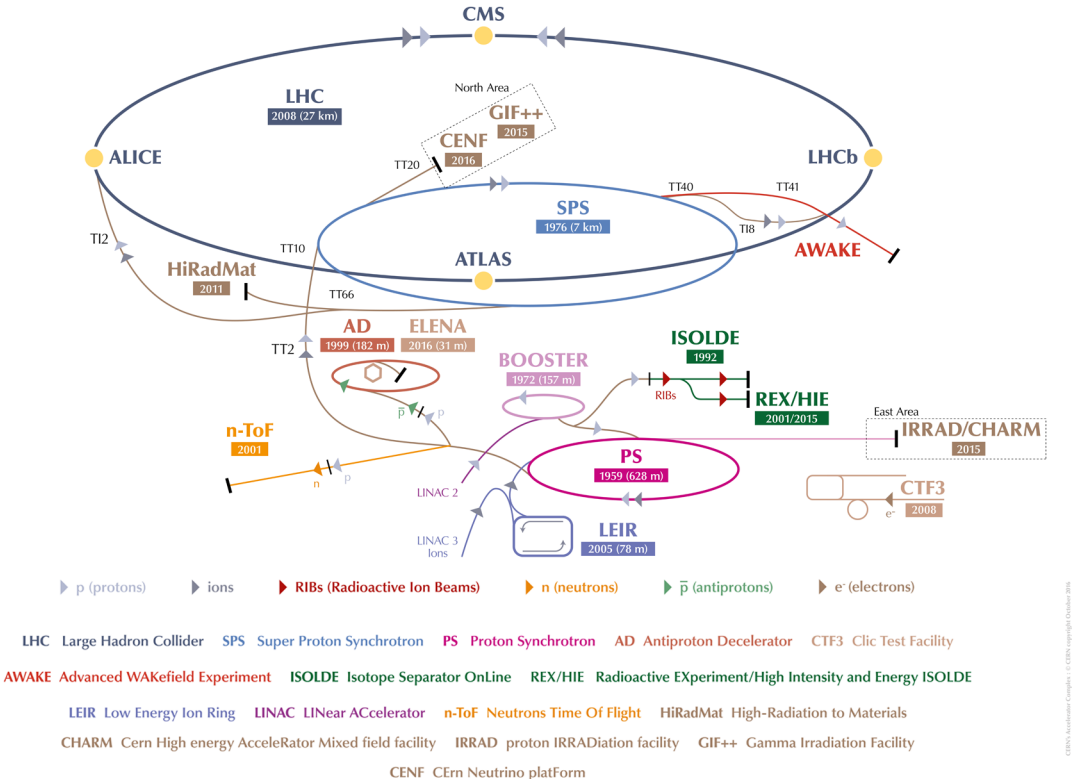

Figure 1. The CERN accelerator complex. [7]

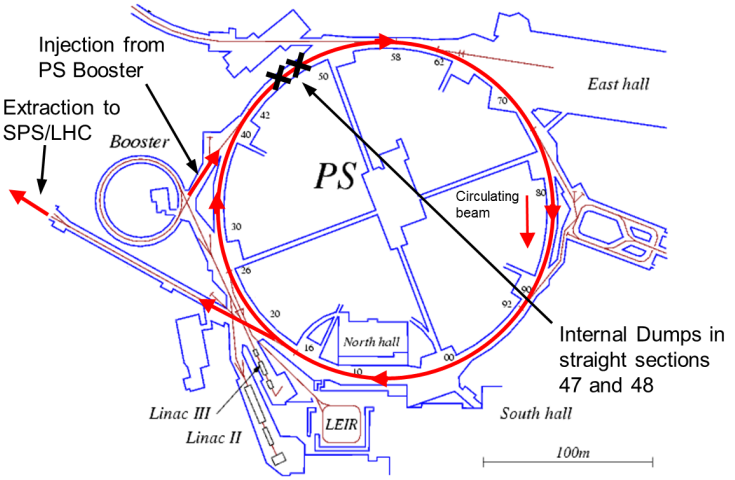

Figure 2. The Proton Synchrotron accelerator complex.

1.2 Proton Synchrotron

The Proton Synchrotron is one of the particle accelerators in CERN's accelerator complex. It is an injector accelerator in the LHC chain, but it also provides beams for other experiments at CERN. It is a circular accelerator with a circumference of 628 m and it can accelerate protons up to an energy of 25 GeV. It consists of 100 bending magnets and it is divided into 100 straight sections. The first protons in the PS were accelerated to full energy in 1959 and since then it has undergone several upgrades. An overview of the Proton Synchrotron is presented in Figure 2. [1, 8]

The Proton Synchrotron consists of different systems such as magnets, accelerating cavities, power supplies, vacuum vessels and pumps, controls, measurement instruments and many others [8]. One important piece of equipment is a beam dump. It is a device to stop the beam (i.e. dump the beam) in a controlled way to protect the accelerator from an uncontrolled beam loss. An accidental beam impact or irradiation due to beam losses could cause, for example, damage in materials, errors in electronics or radioactivation of the environment which risks the health of personnel [9]. Therefore, a beam dump is an important safety device to avoid damage that could interrupt the operation of the accelerator for a long time [10].

The general idea of a beam dump is to impact (i.e. dump) the beam into a device designed to withstand the impact. The passage of protons through the dump material causes them to lose energy and eventually stop if the material is sufficiently thick. The energy lost by the protons is mostly converted into heat, causing a thermal shock in the material. A beam dump needs to survive repeated thermal shocks from beam impacts and operate for many years with limited maintenance since they are in radioactive conditions.

The Proton Synchrotron Internal Dumps are two beam dumps currently installed in the straight sections 47 and 48 of the Proton Synchrotron as shown in Figure 2. They are called internal dumps because they are located in the accelerator ring.

1.3 Motivation and Aim

The Proton Synchrotron Internal Dumps are safety devices designed to stop the circulating particle beam to protect the accelerator from an uncontrolled beam loss. The functional part of the currently installed dumps consists of two systems as presented in Figure 3a: the dump core and the dump actuation mechanism. The core is a block of material that can be moved to block the circulating beam's path. The core is actuated by an electromagnet and spring-based mechanism. The current dump core is a block of copper weighing 5.5 kg with dimensions of 132 mm × 36 mm × 130 mm.

After the LHC Injectors Upgrade, the proton beams in the Proton Synchrotron will be more energetic. The maximum number of protons per beam pulse is estimated to be five times higher. Preliminary simulations show that the current dump core is not foreseen to survive the dumping of the new beams [4]. Additionally, the current dumps are old devices designed and produced in the 1970s. Therefore, new and upgraded dumps need to be designed, prototyped and installed by the EN-STI group of CERN [11].

The new dump design is based on the current dumps with a core and an actuation mechanism as presented in Figure 3b. The topic of this thesis is the preliminary design of the new dump core. It weighs 13 kg and consists of three main materials: graphite, copper–chromium–zirconium copper alloy, and stainless steel. The requirements and objectives for the core design are set in a functional specifications document [11], which lists three main objectives for the dump core: ensure the core mechanical integrity in beam impact, minimize the mass since the core is moved, and minimize the beam energy escaping the dump to protect other accelerator equipment.

The first aim of this thesis is to present the preliminary core design including its function, geometry, materials and cooling system. The second aim is to study the fulfillment of the first objective: the mechanical integrity of the core materials under beam impact induced thermal shock. The materials should stay below their maximum allowable temperatures, the stresses should stay in the elastic regime, the materials should not suffer fatigue damage, and they should withstand long-term radiation damage.

The temperatures and stresses in the core will be studied with finite element analysis. The aim is to identify critical load scenarios and to produce and verify a model to simulate them. Fatigue will be studied by comparing the stress state to fatigue studies found in literature. The radiation damage will be studied by comparing simulated irradiation conditions in the core materials to values found in literature.

The second objective, minimizing the core mass, stems from a requirement to sweep through the beam in less than 150 ms. This constraint has been considered in the core design, but studies of the actuation mechanism are outside the scope of this thesis. Likewise the third objective of minimizing the escaping energy has been considered, but studies on the effects of dumping on the surrounding accelerator equipment are outside the scope of this thesis.

Simulations related to the beam dynamics or beam–matter interaction are also outside the scope of this thesis. Nevertheless, some background is presented to provide understanding of the design choices and simulation inputs. The thesis is also limited to the study of proton beams, but the dump is also required to be able to dump ion beams [11].

The design of the dump core is still in the preliminary stages. Therefore, in this thesis a general perspective of the design is taken. Some aspects or details of the design will be left for further studies, influenced also by the outcomes of this thesis.

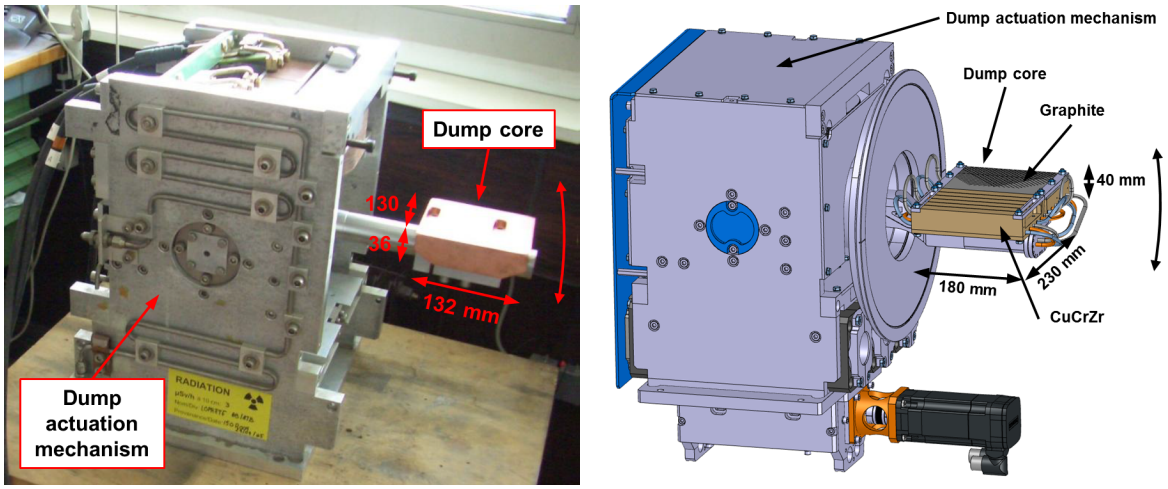

(a) (b)

Figure 3. The dump core and actuation mechanism of (a) the current and (b) the new preliminary design of the Proton Synchrotron Internal Dump.

2 Proton Synchrotron Internal Dumps

2.1 Current Proton Synchrotron Internal Dumps

Two Internal Dumps are currently installed and used in the Proton Synchrotron. They are used for two purposes: Firstly, to dump the beam when studying new beams or solving problems with the accelerator. Secondly, to act as an automatic machine protection system preventing uncontrolled beam loss or extraction from the Proton Synchrotron if the destination facilities are not ready to accept the beam. The dumping can be triggered manually by machine operators or with an interlock. With an interlock the dump is automatically triggered when a programmed criteria is fulfilled. The dumps are not used to protect personnel. [11]

The current dumps were designed in 1975 [4] and have been operating ever since with limited maintenance. They are called internal dumps because they are located in the accelerator ring between two bending magnets as shown in Figure 4. The space between the magnets is limited to approximately one meter, which needs to include the dump itself as well as a vacuum vessel and radiation shielding. Normally in the beam dumps of CERN the circulating beam is diverted with a kicker magnet into a static dump outside the accelerator ring, but this requires space for the magnet and the dump. Due to the restricted space in the Internal Dumps, the dump is moved into the beam path instead.

The current Internal Dumps can be divided into three main systems: the dump core, the actuation mechanism and the radiation shielding. The core and the actuation mechanism are located inside the radiation shielding as seen in Figure 5. The actuation mechanism is located outside vacuum, while the core is in the vacuum inside the beam vacuum chamber.

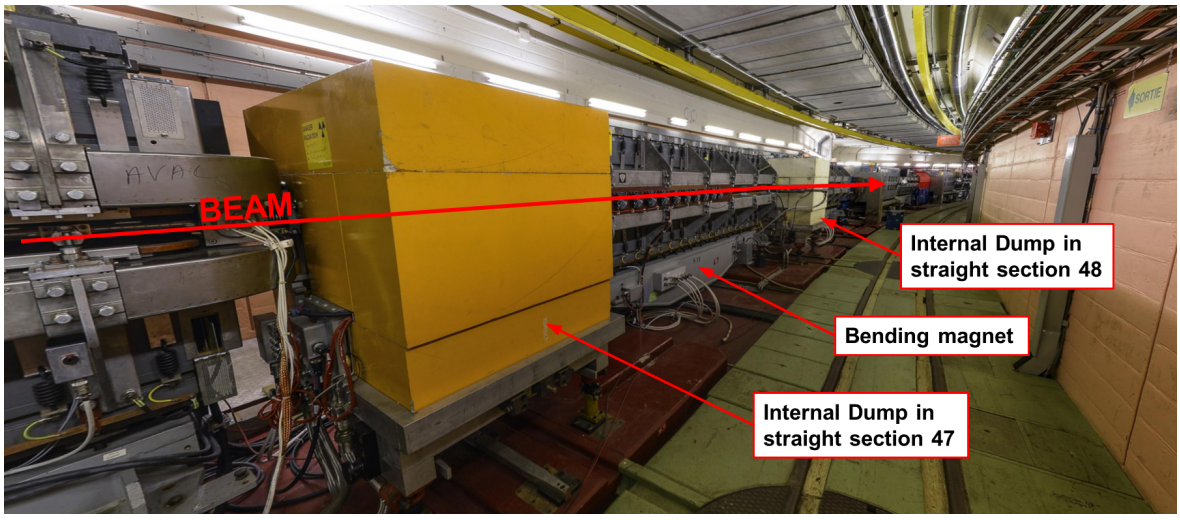

Figure 4. The current Internal Dumps are located between bending magnets in straight sections 47 and 48 of the Proton Synchrotron. From outside only the stone radiation shielding blocks can be seen.

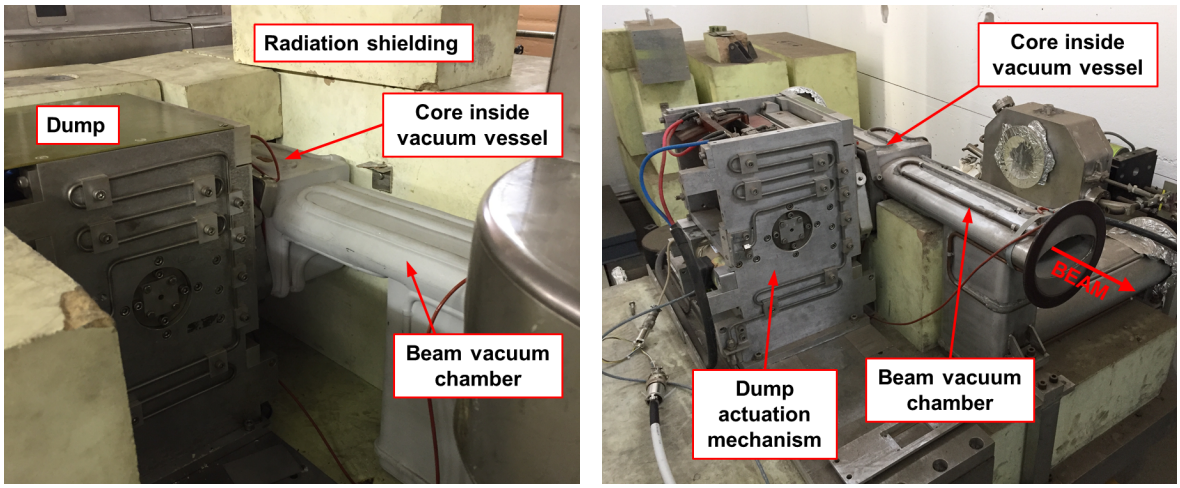

Figure 5. Photos of the current Internal Dumps.

The actuation mechanism is a system with an electromagnet and springs as presented in Figure 6. The system has three shafts that rotate around an axis. When the dump is not used, the magnet keeps the dump core in parking position out of the beam path. When the dump is triggered the current in the electromagnet is cut and the loaded springs push the shafts to rotate. Driven by the springs, the dump core sweeps through the beam pipe and returns to the parking position, where the electromagnet is activated again, recapturing the rotating system. In case of a power cut, or if the electromagnet fails to recapture the rotating system, there is a safety motor to drive the system back to the parking position.

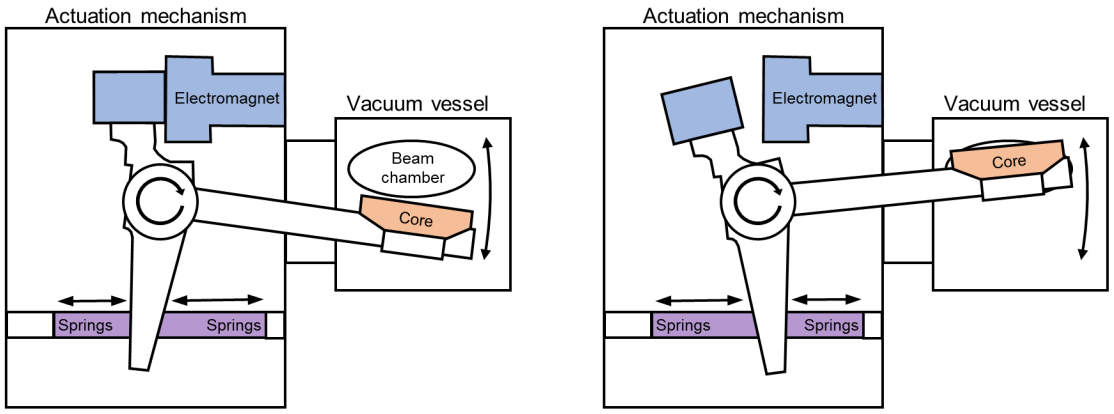

(a) Parking position. (b) Core in beam path.

Figure 6. Schematic of the current dump actuation mechanism.

The current dump core is a block of copper weighing 5.5 kg with dimensions of 132 mm × 36 mm × 130 mm as presented in Figure 7. The core is connected to the actuation mechanism with a shaft. The core in vacuum is separated from the actuation mechanism outside vacuum by a vacuum bellow. There are cooling pipes inside the shaft to cool down the core.

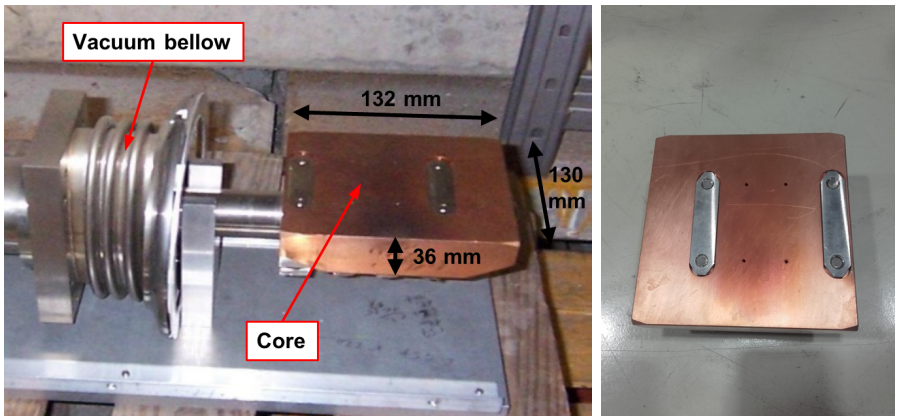

Figure 7. Photos of the current dump core.

The dumping cycle of the current dumps lasts approximately 180 ms. The movement of the core inside the beam chamber was captured with a high-speed camera, as shown in Figure 8. From the video a velocity of about 1.3 m/s in the beam chamber center can be measured.

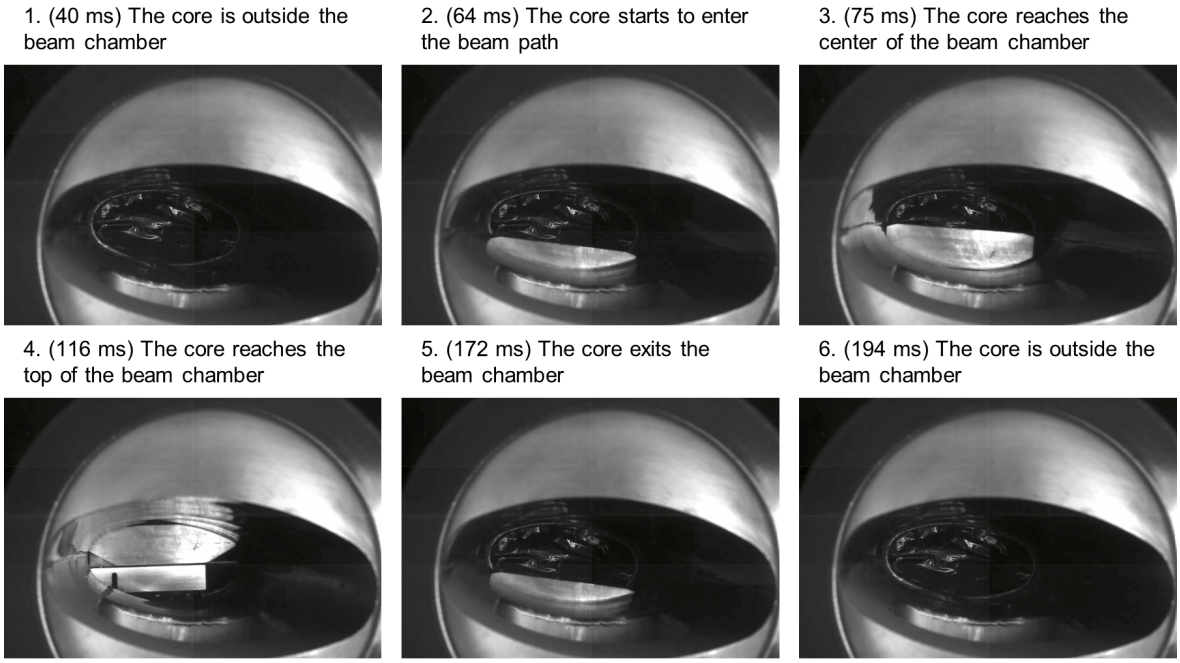

Figure 8. The current dump core inside the beam chamber during a dumping cycle.

The starting point for the design of the new dumps is the current dumps, which have been proven to work reliably in a radioactive environment with limited maintenance for over 40 years. Inspecting the current dumps in operation is unfeasible as they are in use and radioactive, but researching the old design documents and inspecting the spare dumps can offer insight into the design. Nevertheless, much of the specifics of the current dump design remain unknown, especially relating to the dump core.

2.2 New Proton Synchrotron Internal Dumps

The design of the new dumps resembles the current dumps with a core, an actuation mechanism and radiation shielding. A 3D model of the new preliminary shielding and actuation mechanism, designed by the EN-MME group of CERN, is presented in Figure 9. A section view of the mechanism is presented in Figure 10. The range of rotation of the core shaft is from $-12°$ to $12°$. A safety motor is used to drive the mechanism into parking position at the beginning of operation or in case of a power cut or failure of the electromagnet.

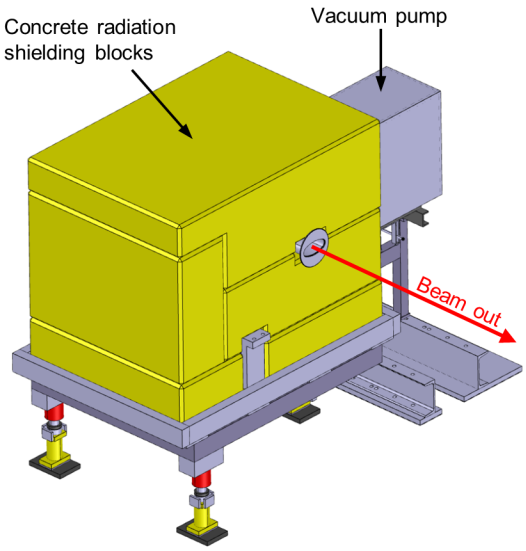

(a) Dump with radiation shielding.

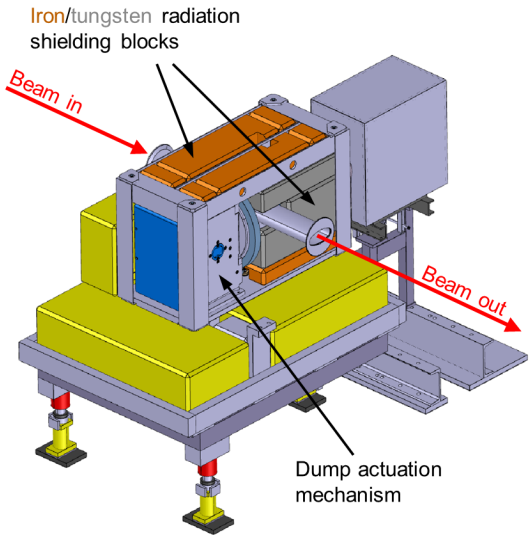

(b) Dump without concrete shielding blocks.

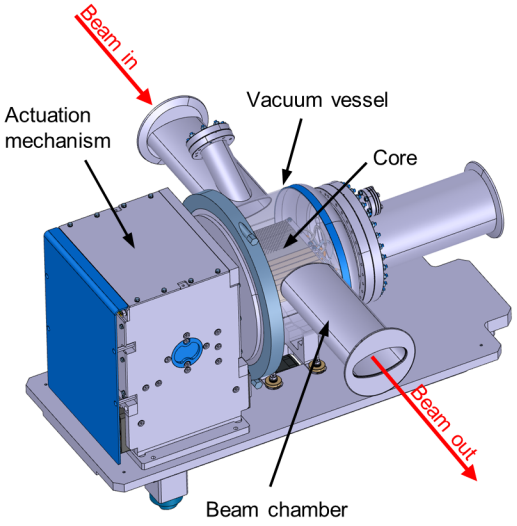

(c) Dump mechanism, vacuum vessel and core.

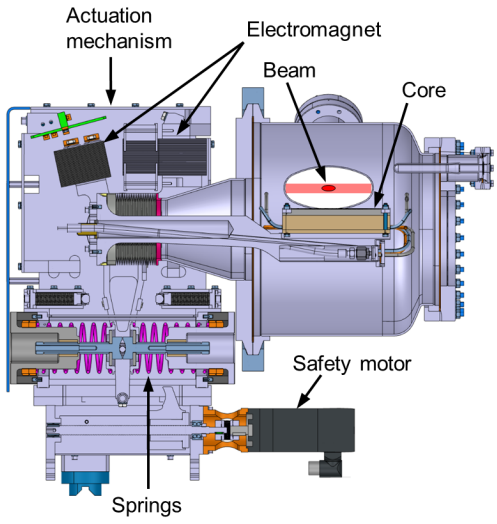

(d) Section view.

Figure 9. Overview of the preliminary new Proton Synchrotron Internal Dump design.

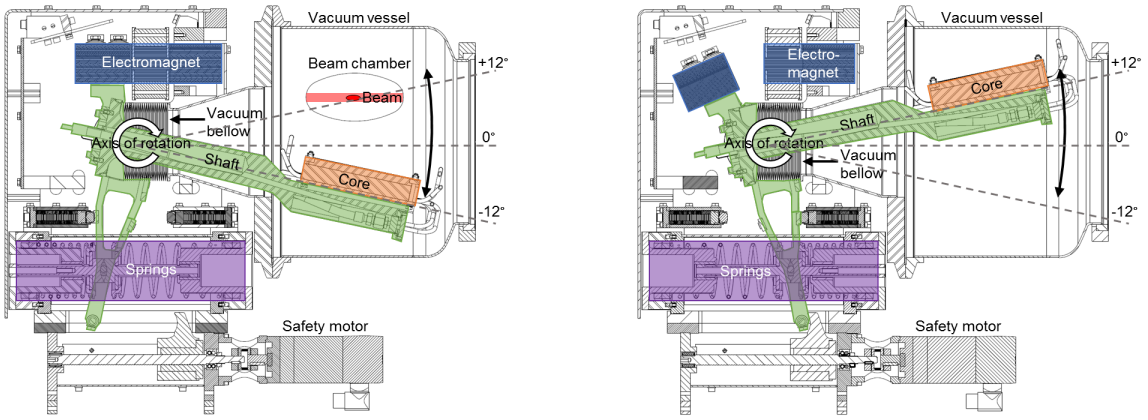

(a) Mechanism in parking position at −12°.

(b) Mechanism in top position at 12°.

Figure 10. Section view of the dump with important systems highlighted.

The terms downstream and upstream of the beam are defined to ease the description of the geometry. Downstream direction is in the direction of the beam (i.e. after the dump) and upstream is in the direction against the beam (i.e. before the dump).

The functional specifications document [11] lists three main objectives for the design of the new dump core:

1. Ensure the mechanical integrity of the dump core materials in beam impact. The materials should stay below their maximum allowable temperature and the stresses should stay in the elastic regime. The materials should also not suffer fatigue failure due to repeated beam impacts and they should withstand long-term radiation damage.

2. Minimize the dump core mass since it is has to be moved quickly by the mechanism.

3. Minimize the beam energy escaping from the dump after impact to protect the accelerator equipment downstream of the dump.

A failure of the dump core could interrupt the operation of the Proton Synchrotron and all other accelerators and facilities dependent on it for a long time. The whole dump assembly has to be replaced with a spare if the core fails as the dumps in operation will be radioactive. Therefore it is especially important to ensure the mechanical integrity of the dump core. The dump core design begins with selecting a combination of materials able to withstand a beam impact. The expected lifetime of the new dumps is at least until the end of the year of 2035 [11]. Therefore long-term radiation damage and fatigue from repeated beam impacts is also a concern.

The mass of the dump needs to be as low as possible since it has to be moved in and out of the beam path quickly. The functional specification [11] states that the dump should complete a full cycle from parking position to the beam line and back to the parking position in a maximum time of 500 ms. This is attempted to be reduced to 300 ms as it is foreseen to be the minimum time between the extraction of one beam pulse and the injection of the next one. The maximum mass is set at 20 kg. This limitation places constraints on the material density and dimensions of the core.

The purpose of a dump is to absorb beam energy in a controlled way. The beam energy escaping the dump after impact should be minimized as it can damage the equipment downstream of the dump, especially the first bending magnet. The escaping energy can be minimized in two ways: by increasing the material thickness the beam passes through, or by using denser materials. Both ways increase the mass of the dump, which is in direct conflict with the second objective. More beam energy will also be deposited in denser materials, which is in conflict with the first objective. Minimizing the escaping energy drives the design towards denser materials and larger dimensions. In actuality, the PS Internal Dump core is not massive enough to absorb a full proton beam and as such it functions more as a beam dilutor or scatterer than an actual dump.

There are several additional requirements for the design: The beam can be at any point in the vacuum chamber horizontally, as shown in Figure 10. Therefore the core should horizontally cover the whole 146 mm wide beam chamber. The beam position variation in the vertical plane is negligible and is not considered. The length of the core in beam direction is restricted to 230 mm by the size of the vacuum vessel. The core is located in ultra-high vacuum with an absolute pressure of 2×10^{-8} mbar and it operates in radioactive conditions, requiring vacuum compliant and radiation hard design. [11]

A 3D model of the preliminary new dump core designed by EN-MME is presented in Figure 11. The dimensions of the new core are 180 mm × 40 mm × 230 mm (width × height × length) and it weighs approximately 13 kg. Three main materials are used in the core: graphite SGL SIGRAFINE® R7550, copper–chromium–zirconium (CuCrZr) precipitation hardened copper alloy, and stainless steel. Graphite and CuCrZr are the main beam impacted materials, while stainless steel is used for the cooling circuits and support structures. The core is attached to the shaft from the bottom with four bolts.

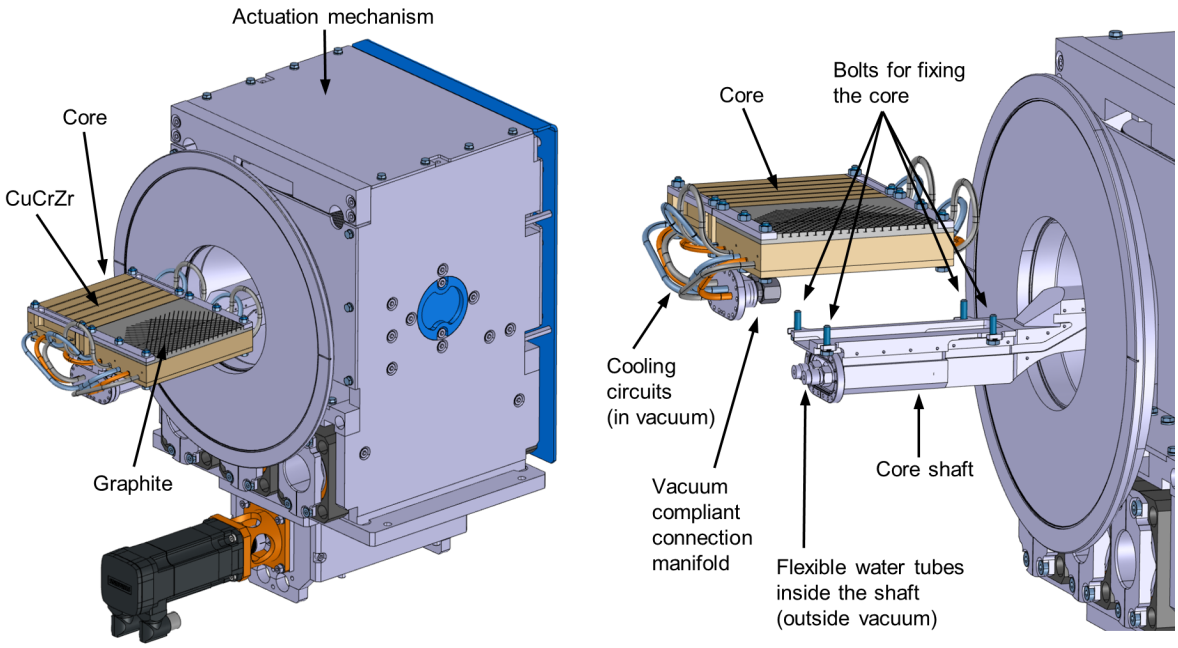

Figure 11. The new dump core attached to the actuation mechanism.

The cooling system consists of three circuits in the vacuum. Each circuit passes through the core four times. The cooling pipes are welded to a vacuum flange and connected to two flexible water pipes inside the core shaft, which is outside vacuum. The circuits are seamless with no welds or connections where water could leak into the vacuum and reduce the vacuum pressure.

This section served as an introduction to the new Internal Dump and its core. A more detailed description of the new core geometry, materials and considered beam scenarios will be presented in Section 4.

3 Theoretical Background

3.1 Proton Beams and Multi-Turn Beam Shaving

The total energy E_{tot} of a proton is the sum of its rest energy $E_0 = 938\,\text{MeV}$ [12] and its kinetic energy E_{kin} [13].

$$E_{\text{tot}} = E_0 + E_{\text{kin}} \tag{1}$$

At high enough energies the protons are often described by their momentum p which is linked to the energy through the relation [13]

$$E_{\text{tot}}^2 = E_0^2 + p^2c^2 \tag{2}$$

where c is the speed of light in vacuum. The energy of a proton beam is obtained by multiplying the protons' kinetic energy by the number of protons in the beam [5].

$$E_{\text{beam}} = N \cdot E_{\text{kin}} \tag{3}$$

where E_{beam} is the beam energy and N is the number of protons in the beam, or the beam intensity. The beam intensity can also be given as protons per pulse (ppp).

In accelerator physics, energies are usually given in electronvolts. They can be converted to joules with the relation $1\,\text{eV} = 1.602\,176 \times 10^{-19}\,\text{J}$ [12]. The energy in the Proton Synchrotron ranges from 1.4 GeV, when the beam is injected into the ring, up to a maximum momentum of 26 GeV/c after acceleration [14]. Considering the most energetic future beam foreseen in the Proton Synchrotron with an intensity of 5×10^{13} protons and a momentum of 26 GeV/c [11], a maximum beam energy of 1.25×10^{15} GeV or 201 kJ can be calculated with Equations (1) – (3).

The beams in the Proton Synchrotron are structured in pulses. During one pulse the beam is injected, accelerated, and then either extracted or dumped before the next pulse. The Proton Synchrotron operates in basic cycles lasting 1.2 s. The length of a pulse, or the pulse period, is a multiple of the basic cycle (i.e. 1.2, 2.4 or 3.6 s). The beam pulses are further divided in bunches. An example LHC filling beam pulse is presented in Figure 12 [4]. The protons are injected in 4+2 bunches from the Proton Synchrotron Booster, which are then split into 72 bunches. The magnetic field is ramped up and the protons are accelerated to the maximum momentum of 26 GeV/c before extraction to the SPS, the next accelerator in the LHC chain. A beam dump can be triggered at any point of the pulse.

Beam pulses can have a single or multiple bunches depending on the beam type. Some beams contain only a single bunch, but for example the LHC filling pulse can have 72 bunches that are 4 ns long and are spaced by 25 ns (measured in time in a static observational frame of reference) [4]. The different lengths and timings of beam bunches and pulses are illustrated in Figure 13. For simplicity, the beam pulses in the simulations will be considered fully debunched [11], i.e. the distribution of protons is uniform along the ring and the beam is continuous.

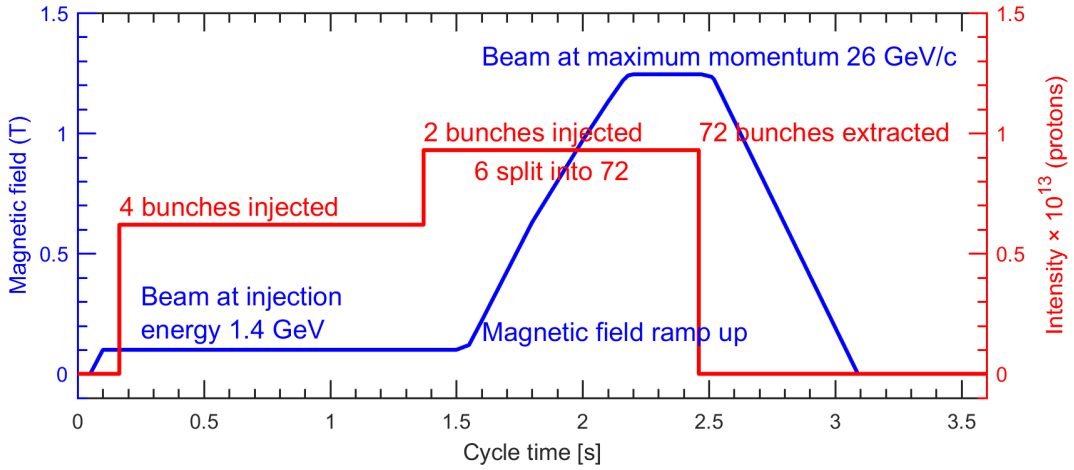

Figure 12. An example beam pulse headed to the LHC with a pulse period of 3.6 s. The beam is injected in 4+2 bunches with an energy of 1.4 GeV. The beam is accelerated to a momentum of 26 GeV/c before extraction. A beam dump can be triggered at any time of the pulse. Figure adapted from [4].

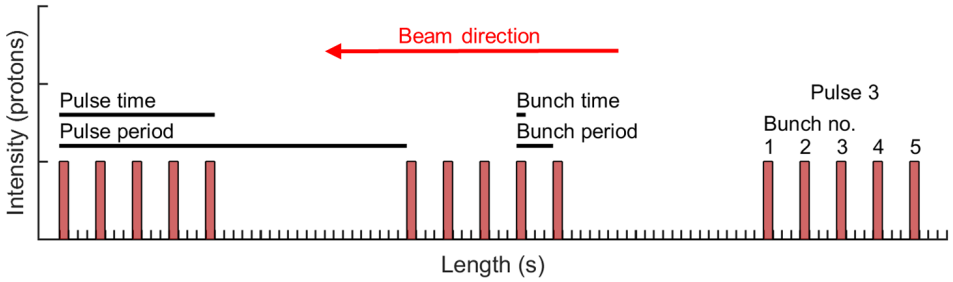

Figure 13. The beams are structured in pulses and bunches. The characteristic lengths of simplified example beam pulses are illustrated.

The machine operators can set different beam pulse types to be injected into the Proton Synchrotron, one after another, to build supercycles around 30 s to 60 s in length. The series of different beam pulses is then repeated in the accelerator. The beam pulse types can have very different intensities, energies, sizes and pulse periods depending on the pulse destination. The dump can be triggered for each beam pulse separately.

The distribution of the protons in a beam can be approximated to be Gaussian. The size of the beam is usually given as the vertical and horizontal standard deviations σ_{v} and σ_{h} of the Gaussian distribution, commonly also called the spot size or the "sigma" of the beam. The spot sizes at extraction in the Proton Synchrotron vary from 0.65 mm to 5.24 mm. The beams are typically larger at injection and they are squeezed before extraction. The beam spot sizes vary between odd and even straight sections of the Proton Synchrotron. [14]

The orbit of the protons in the Proton Synchrotron machine is not completely circular. They are oscillating harmonically around their orbit as they circulate as shown in Figure 14. The vertical and horizontal tunes Q_{v} and Q_{h} of the machine are parameters

describing how many times a proton oscillates during one revolution around the machine [5]. The tune has an effect on where the protons hit the dump core. Current operational tunes in the Proton Synchrotron vary vertically within $Q_{\mathrm{v}} = [6.1, 6.24]$ and horizontally within $Q_{\mathrm{h}} = [6.1, 6.245]$ [4].

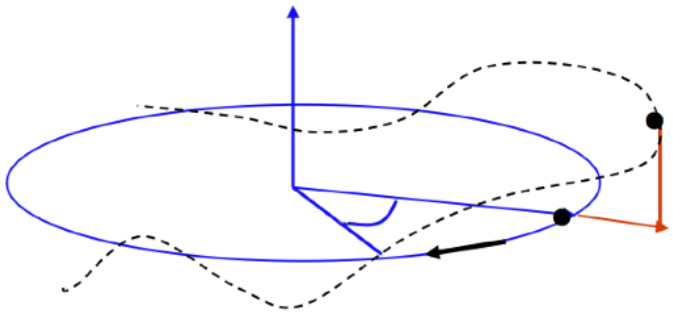

Figure 14. Trajectory of a circulating proton in an accelerator [15].

The working principle of the Proton Synchrotron Internal Dumps is different from the more common static dumps at CERN: The core is located outside of the beam path while the beam is circulating in the accelerator. When the dump is triggered, the core is moved into the beam path. The time it takes for a proton to circulate once in the Proton Synchrotron at top energy is 2.1 µs [11]. Based on simulations of the actuation mechanism and measurements made with a high-speed camera(see Figure 8), the core of the current dump moves with an approximate velocity of 1.3 m/s when in the beam path. Thus the distance the dump core moves during one proton revolution is $1.3\,\mathrm{m/s} \cdot 2.1\,\mu\mathrm{s} = 2.7\,\mu\mathrm{m}$. The beam spot sizes are in the order of millimeters and as such it takes several milliseconds and thousands of beam revolutions for the dump to cover the whole beam cross section.

Considering this result, the dumping process can be described as multi-turn beam shaving. The beam impacts on the same surface area of the core turn after turn. The protons might also traverse through the core material multiple times before eventually being stopped or lost somewhere in the accelerator. A simplified illustration of the multi-turn beam shaving process is shown in Figure 15. In actuality, the beam shaving process is more complex due to the protons' interaction with the dump and the beam dynamics in the Proton Synchrotron.

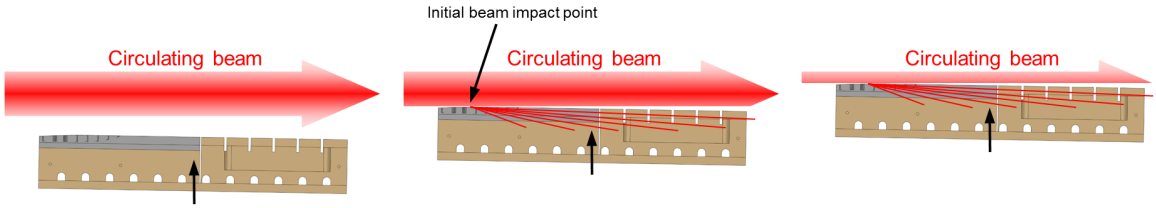

(a) Core out of beam path. (b) Start of beam shaving. (c) End of beam shaving.

Figure 15. Simplified illustration of the multi-turn beam shaving process. The core starts from outside the beam path and is moved into the circulating beam. The core moves slowly compared to the circulating protons, causing the beam to be shaved by the core surface during multiple beam turns.

The only possibility for the core to be impacted centrally in a direct impact is if the dump is triggered before beam injection. In this case the core can be in the beam path when the beam is injected. This is considered to be a rare unintended event and the beam energy at injection is lower than at extraction. As such a direct impact is not considered as critical case for the dump core design at this stage.

A method to simulate the circulating protons and their interaction with the core material has been developed in FLUKA code by the EN-STI-FDA section of CERN. FLUKA is a Monte Carlo code used to simulate the transport of particles and their interaction with matter [16]. The FLUKA simulations of the dump core presented in this thesis are performed by the FDA section. In addition to the topics discussed in this section, many other aspects of beam dynamics have to be considered in the simulations but describing them is outside the scope of this thesis.

To validate the simulation approach in FLUKA, beam intensity losses were measured during dumping with the current dumps. The geometry of the current dump core was modeled and the beam scenarios were recreated in FLUKA using the measured beam parameters. The measured and simulated intensity losses over time are presented in Figure 16. The matching time-scales and slopes of the intensity losses support the simulation approach. Some differences are observed at the beginning and end of the dumping process that are still to be fully understood. [17]

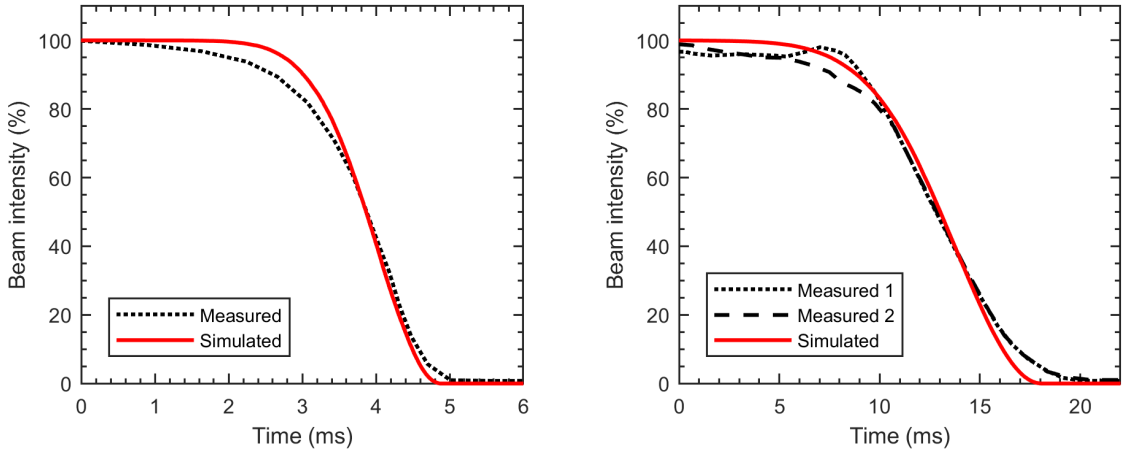

Figure 16. Comparison of measured and simulated beam intensity losses during the dumping of (a) a LHC beam pulse at extraction momentum and (b) TOF beam pulses at injection energy. Measurements were performed with the current Internal Dumps with the current beams. FLUKA simulations performed by EN-STI-FDA section of CERN. [17]

3.2 Beam–Material Interaction

When high-energy particles pass through material they lose energy through interaction with material [9]. The lost energy is mostly converted into heat in the material leading to a temperature increase. Due to the high temperature increase (up to a few thousand degrees) and the short time-scales (milliseconds or less), the response to a beam impact in material can be described as a thermal shock.

The extended physics behind beam–material interaction are beyond the scope of this thesis, but some background is provided for understanding of design choices and simulation inputs. The theory presented in this section is relevant for high-energy protons in the range of the Proton Synchrotron from 1.4 GeV to 26 GeV/c.

Characteristic of a beam impact in material are hadronic cascades, protons being a type of hadron, and electromagnetic showers. Together they can be called a particle shower: The primary beam protons interact with the material, depositing energy, changing their trajectory and generating secondary particles. The particle shower results in a widening pattern of energy deposition in the material along the beam axis as seen in Figure 17a. As the protons traverse deeper into the material the interactions avalanche and a peak energy deposition is reached deep inside the material. [9]

In general, the higher the material density is, the more interactions the protons suffer. The length scale of the hadronic cascades along the beam axis is the nuclear interaction length X_I [9]. After traversing one interaction length in the material on average 63% of the protons have suffered a nuclear interaction [18]. The interaction length depends on the material's atomic density and the size of the atoms. Denser materials have a shorter interaction length. For example, the nuclear interaction length for graphite is approximately 38.8 cm and for copper 15.3 cm, which are similar to the materials used in the dump core [12].

For electromagnetic showers the length scale is the radiation length X_0 which is the mean distance over which a high-energy electron loses around 63% of its energy. The values for graphite and copper are 19.3 cm and 1.44 cm respectively. [12]

While more particles can be stopped with a denser material, the trade-off is a higher energy deposition per unit volume and a higher resulting temperature increase, as observed in Figure 17b. One approach to beam dump design is to combine materials so that lighter materials dilute the beam first before denser materials absorb more energy of the subsequent particle shower. This approach allows the use of dense materials for more energy absorption while the lower density materials protect them from a too strong thermal shock.

The interaction of protons with material is simulated with the FLUKA code: Numerous individual protons are simulated and their combined statistical energy deposition map is recorded. The obtained energy deposition map is normalized for one proton and can then be scaled by the intensity of the beam to obtain the energy deposition map in a beam impact. The number of protons simulated in FLUKA depends on the statistical accuracy required and is typically in the order of 10^6 in the dump core simulations, while in the Proton Synchrotron maximum beam intensities are in the order of 10^{13}. The geometry in FLUKA is divided into a number of finite volumes where the energy deposition is recorded. This energy deposition map can then be imported into finite element software. A cross section of an example energy deposition map from FLUKA is shown in Figure 17a.

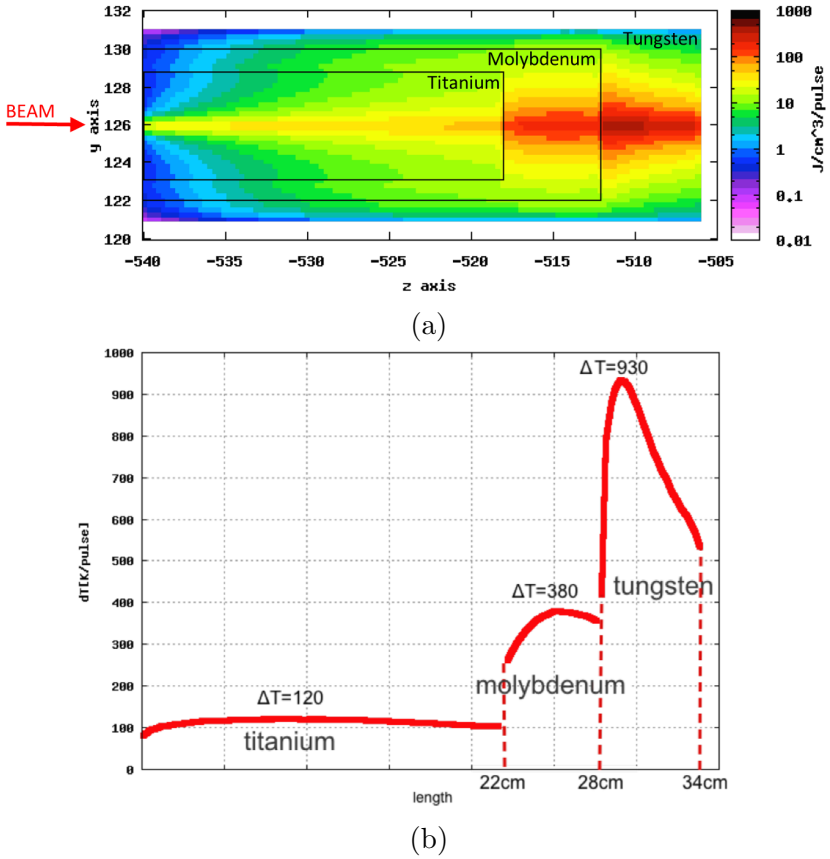

Figure 17. FLUKA simulation results from a previous design iteration of the Proton Synchrotron Internal Dump core. The design combines titanium with denser molybdenum and tungsten. (a) A cross section of an energy deposition map from FLUKA. The particle shower generated in the impact can be seen as a widening energy deposition. (b) Adiabatic peak temperature increase along the core length calculated from the energy deposition. Figure adapted from [4].

3.3 Material Behavior in Beam Impact

3.3.1 Beam Impact Induced Damage

Interaction with high-energy protons induce a thermo-mechanical response in the material. The severity of the thermal shock depends on the energy of the beam and the time-scale of the impact. At lower energies and longer time-scales the effects may include vibrations, stress waves and permanent deformations of the material. At higher energies and shorter time-scales the effects can be more extreme, such as material phase transitions, changes in material density, fragmentation and even explosive failure of the material. [10]

An example of beam induced damage in a copper block can be seen in Figure 18. The damage ranges from no visible damage (A) and colorization (B) to melting (D and C). Figure 19 shows an incident from 2004, where a beam was extracted from the SPS to the LHC on a wrong trajectory due to a magnet switch-off, causing an accidental beam impact on a vacuum chamber [10]. These examples highlight the need to protect the accelerator machine from accidental beam impacts with safety devices, including beam dumps.

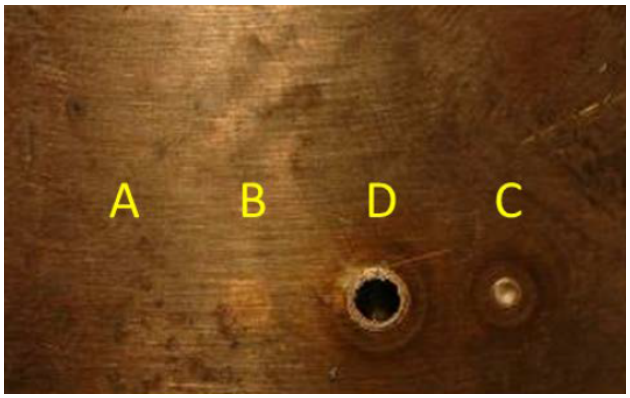

Figure 18. Beam impact induced damage in a copper block corresponding to a 450 GeV beam with a size of 1 mm and intensities of (A) 1.32×10^{12} protons, (B) 2.64×10^{12} protons, (C) 5.28×10^{12} protons, (D) 7.92×10^{12} protons. [10]

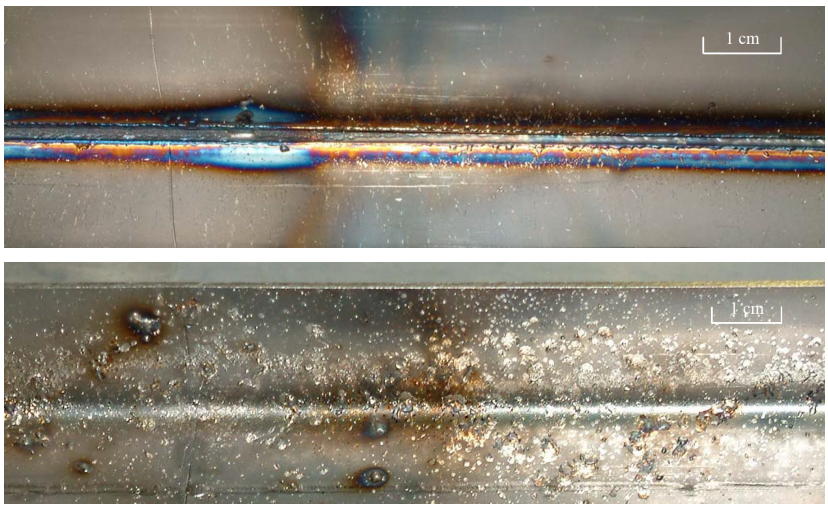

Figure 19. An accidental 450 GeV beam impact on a steel vacuum chamber with an intensity of 3.4×10^{13} protons. Top: a 110 cm long groove on the vacuum chamber cut by the beam. Bottom: projected molten steel on the vacuum chamber wall on opposite side to the beam impact. [10]

In addition to instantaneous damage as a result of the thermal shock, beam impacts cause accumulating irradiation damage in the material through atomic displacements and gas production [9]. Radiation displaces atoms from the equilibrium position in the crystalline lattice of the material forming interstitial atoms and vacancies in the lattice. The amount of damage is quantified as a function of displacements per atom (DPA). The DPA is heavily dependent on the particle type, energy and charge, as well as the material and its temperature. [19]

The effects of irradiation in metals include hardening, embrittlement, void swelling and degradation of thermal conductivity [9, 19, 20]. Often in literature the material characteristics in relation to DPA are reported for neutron irradiation, which is not directly comparable with proton irradiation. Regardless, the DPA values obtained from FLUKA simulations can be compared with neutron irradiation data from literature to estimate the damage in the dump core materials. Research is ongoing, for example

by the RaDIATE collaboration, to assess radiation damage in materials in proton accelerator environment, including CuCrZr and several graphite grades [21].

Neutron irradiation of copper and its alloys, including CuCrZr, at temperatures below 280 °C cause radiation hardening due to formation of small dislocations and faults [20, 22]. The resulting increase in yield strength is accompanied with a reduction in ductility [20, 22]. The yield strength in copper and its alloys increase until a saturation value of around 0.1–0.5 DPA is reached [20, 22–24]. Contrarily, neutron irradiation at temperatures above 280 °C cause softening in CuCrZr [20, 22]. The change in yield strength with respect to the irradiation temperature is plotted in Figure 20.

A stress-strain curve for CuCrZr irradiated with neutrons at 80 °C is presented in Figure 21. The condition of CuCrZr is solution annealed and aged condition, similarly to the CuCrZr foreseen to be used in the dump core. Radiation hardening and embrittlement is observed, i.e. the yield strength increases while the maximum elongation decreases with DPA.

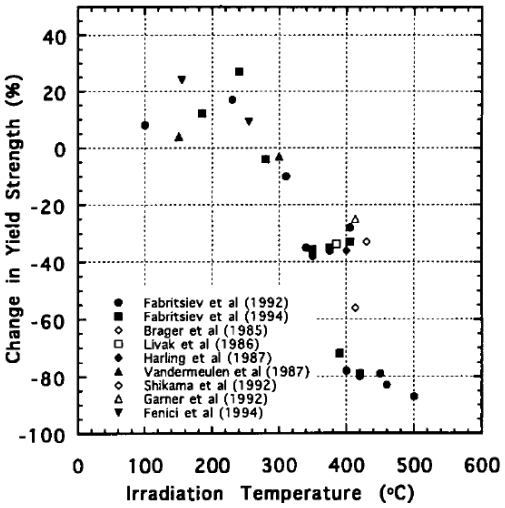

Figure 20. Change in yield strength of CuCrZr due to neutron irradiation at various temperatures. Filled symbols mean tensile measurements made near irradiation temperature and open symbols mean tensile measurements made at room temperature. [20]

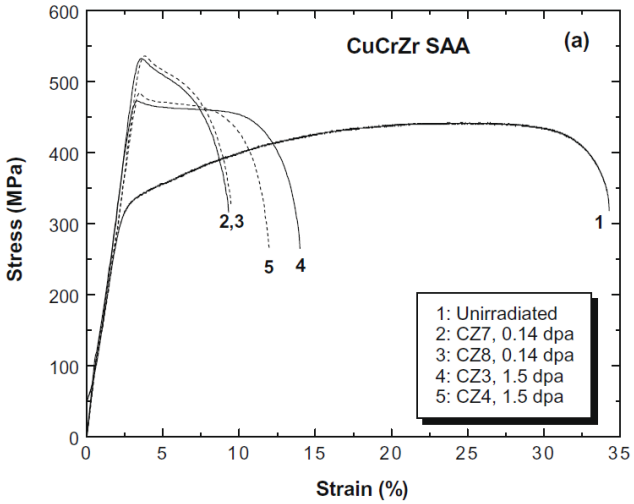

Figure 21. Stress–strain curves for CuCrZr in solution annealed and aged (SAA) condition before irradiation and after neutron irradiation at 80 °C. Tensile tests performed at room temperature. [23]

Hydrogen and helium gas produced during irradiation causes void swelling (i.e. volume increase) [19, 20]. Copper alloys show swelling due to microscopic void formation in the material at irradiation temperatures between 180 °C and 550 °C, with a peak swelling rate at around 300 °C. A swelling rate of 0.5% density change per DPA is typical for pure copper, but precipitation hardened copper alloys such as CuCrZr show an increased swelling resistance due to the impurity particles promoting the correction of the vacancies and interstitial atoms in the crystalline lattice. Swelling of below 2% density change in CuCrZr has been measured for DPA levels up to 50 DPA at irradiation temperatures around 400 °C. [20, 22]

Irradiation also degrades thermal conductivity in CuCrZr through several mechanisms. Fabritsiev et al. [22] reported a 5–10% decrease in thermal conductivity due to irradiation defects for DPA values above 0.1 at irradiation temperatures below 150 °C. In [20], a 34% decrease in thermal conductivity due to solid transmutations was calculated for 30 DPA. Void swelling also decreases thermal conductivity, but CuCrZr is resistant to void swelling [20, 22].

Similarly to CuCrZr, irradiated graphite shows swelling, an increase in strength and degradation of thermal conductivity. Also, the Young's modulus is increased. The thermal conductivity is reduced more if the irradiation temperature is higher. Unirradiated graphite exhibits nonlinear stress-strain behavior, but after irradiation the behavior becomes more linear. Some properties can be recovered by annealing the graphite at high temperatures for several hours, but the temperatures are considered too high and the time-scales too long for annealing to happen in the dump core during dumping operation. Qualitative values for the changes in material properties under irradiation were not found that were directly comparable to the simulated DPA values and the graphite type in question. [25]

3.3.2 Thermal Problem

At the core of the thermal problem is the energy density q_V deposited by the beam and the time-scale of the beam impact. In short time-scales, a quasi-static temperature increase without thermal conduction can be calculated with the equation [10]

$$q_V(x) = \int_{T_0}^{T_1} \rho \cdot c_p(T(x)) \cdot dT(x) \tag{4}$$

where ρ and $c_p(T)$ are the density and the specific heat of the material, $T(x)$ is the temperature at location x, and T_0 and T_1 are temperatures at the beginning and at the end of the energy deposition process [10].

Generally, the specific heat depends on temperature. If it is assumed to be constant, an instantaneous temperature increase ΔT can be calculated from Equation (4) [10].

$$\Delta T(x) = \frac{q_V(x)}{\rho \cdot c_p} \tag{5}$$

Equation (5) assumes no thermal conduction. It can be useful to calculate analytically an adiabatic temperature increase from the applied energy deposition, especially at the location of peak energy deposition. Over time the temperature evolution in the system is determined by the diffusion process which is governed by the heat equation or Fourier's equation [10]

$$\rho c_p \frac{\partial T}{\partial t} = \nabla \cdot (\lambda \nabla T) + \dot{q}_V \tag{6}$$

where λ is the thermal conductivity of the material, t is time and $\dot{q}_V$ is the heat generation rate. From Equation (6) it can be determined that the necessary properties for a thermal characterization of a material are density ρ, specific heat c_p and thermal conductivity λ. Assuming a homogeneous and isotropic material, Fourier's equation simplifies to [10]

$$\frac{\partial T}{\partial t} = a\nabla^2 T + \frac{\dot{q}_V}{\rho \cdot c_p} \tag{7}$$

where $a = \lambda/\rho c_p$ is the thermal diffusivity. [10]

Characteristic of the PS Internal Dumps, compared to many other beam interacting devices at CERN, is a very high and very localized energy deposition on the surface due to the multi-turn shaving impact. Additionally, the time-scales in multi-turn shaving are longer than in usual direct beam impact (milliseconds instead of microseconds). Longer time-scales means that the thermal conduction plays a more important role, as supported by the calculation of the thermal diffusion time, which is defined as [10]

$$t_\mathrm{d} = \frac{B^2}{a} \tag{8}$$

The thermal diffusion time is related to the time required to reach an uniform temperature distribution through diffusion in a material with a characteristic length B (e.g. a disk with radius of B) [10]. In Section 3.1 it was calculated that the dump core is moving a few microns into the beam path during one proton revolution. Assuming energy deposition in a surface thickness of $B = 100\,\mu\mathrm{m}$ and graphite as material with an approximate thermal diffusivity of $a = 50\,\mathrm{mm}^2/\mathrm{s}$ [10, p. 169], the resulting thermal diffusion time is 0.2 ms. The resulting time is one order of magnitude lower than the multi-turn shaving process as shown for example in Figure 16. As such the thermal problem cannot be considered as quasi-static and thermal conduction plays a role.

3.3.3 Structural Problem

A temperature increase in an unconstrained body causes thermal expansion. The free thermal strains ε_{ij}^T of an unconstrained body heated from a reference temperature T_ref (usually uniform ambient room temperature) is in index notation [10]

$$\varepsilon_{ij}^T = \alpha \delta_{ij} \Delta T \tag{9}$$

where α is the coefficient of thermal expansion (CTE) and δ_{ij} is the Kronecker delta. A body can also deform due to mechanical strains ε_{ij}^M. The total strain is the sum of the thermal and mechanical strains [10]

$$\varepsilon_{ij} = \varepsilon_{ij}^M + \varepsilon_{ij}^T \tag{10}$$

An expression for the total strain in an isotropic and homogeneous body is obtained by substituting Equation (9) and Hooke's law into Equation (10). An expression for stresses is also obtained by inverting the relation. [10]

$$\varepsilon_{ij} = \frac{1}{E}[(1+\nu)\sigma_{ij} - \nu\delta_{ij}\sigma_{kk}] + \alpha\delta_{ij}\Delta T \tag{11}$$

$$\sigma_{ij} = \frac{E}{(1+\nu)(1-2\nu)}[(1-2\nu)\varepsilon_{ij} + \nu\delta_{ij}\varepsilon_{kk}] - \delta_{ij}\frac{E\alpha\Delta T}{1-2\nu} \tag{12}$$

where E is the Young's modulus and σ_{ij} are the stress tensor components. From Equation (9) it can be seen that temperature change causes only volumetric deformation ($\varepsilon_{ij}^T = 0$ if $i \neq j$) and if the temperature change is uniform the original body shape is generally

maintained. Free thermal expansion also causes no shear strains. Generally in beam dumps, the temperature increase from a beam impact is not uniform. Temperature gradients in the body lead to non-uniform thermal expansion, causing internal mechanical stresses. In the case of the PS Internal Dump core, mechanical loads are considered negligible, and stresses are caused mainly by a non-uniform temperature increase or differences in material CTEs. [10]

Equation (12) shows that to obtain the stress state in the material, the coefficient of thermal expansion α, Young's modulus E and Poisson's ratio ν need to be specified, in addition to the thermal properties specified in Section 3.3.2. Good materials to withstand thermal shocks are materials with high stress limit and high thermal conductivity, while having a low CTE and Young's modulus as they determine the stresses induced by a temperature increase.

The theory presented above assumes that the material response is quasi-static, i.e. no inertia effects are taken into account. The assumption of no inertia effects needs to be confirmed. Zazula [26] estimates that the results are quasi-static for time-scales above 0.1 ms, while the time-scales for multi-turn beam shaving is expected to be in the order of milliseconds, as seen in Figure 16. The strain rates obtained from the simulations can also be compared with the table presented in Figure 22, which shows aspects to consider in dynamic material testing with respect to strain rates.

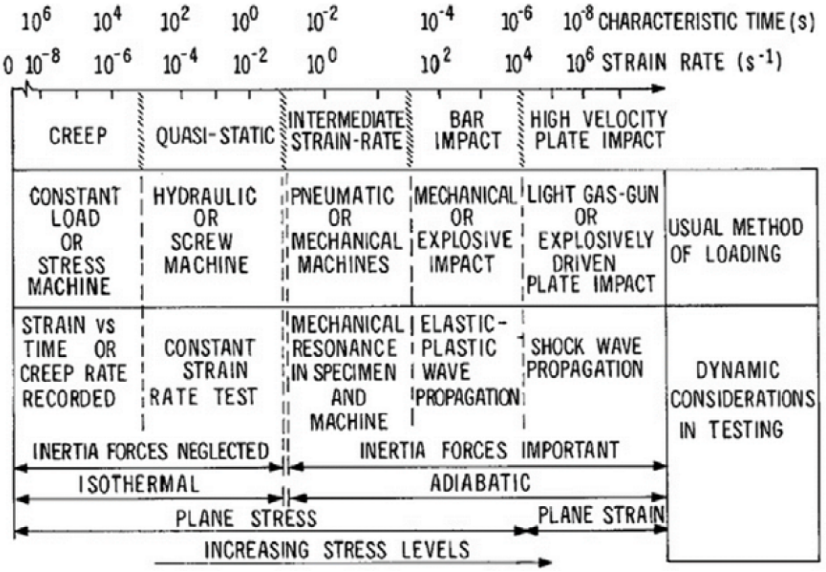

Figure 22. Dynamic aspects to consider in material testing. [10]

When inertia effects are considered, the thermal expansion of the material is partly prevented by its mass inertia. This generates elastic stress waves in the material that propagate through the structure at the speed of sound in the material, $c_0 = \sqrt{E/\rho}$. The elastic stress waves cause tensile and compressive stress states, analogous to a pulse traveling in a spring. At high enough energies a beam impact may cause stresses exceeding the elastic regime limits and cause quasi-static plastic strains, as well as plastic stress waves. The rate of deformation may also be high enough for the material behavior to become strain-rate dependent. [10]

At even greater energies the beam impact might cause shock waves or hydrodynamic tunneling. In this case, the material starts to behave like a fluid and loses mechanical strength. The material may also exhibit changes in density, phase transition (e.g. melting), fragmentation or explosive failure. The simulation of such effects require the use of wave propagation codes or hydrocodes. Examples of such extreme damage are presented in Figures 18 and 19. [10]

3.4 Yield and Failure Criteria

To study the limits of the materials, an appropriate yield or failure criterion needs to be chosen. For the ductile materials, such as CuCrZr and stainless steel, the maximum distortion energy theory, also known as the von Mises yield criterion, is suitable. According to the criterion, the material starts to yield when the equivalent von Mises stress σ_{vM} reaches the yield stress σ_{y}. After yielding the material does not instantly fail, but suffers plastic deformation and hardening. The von Mises yield criterion is defined as [10]

$$\sigma_{\mathrm{vM}} = \frac{1}{\sqrt{2}}\sqrt{(\sigma_1-\sigma_2)^2+(\sigma_2-\sigma_3)^2+(\sigma_3-\sigma_1)^2} = \sigma_{\mathrm{y}} \tag{13}$$

where $\sigma_1 > \sigma_2 > \sigma_3$ are the principal stresses. A safety factor can be defined by comparing the yield strength to the maximum von Mises stress, taking into account the decrease of yield strength with temperature.

$$\mathrm{SF}_{\mathrm{vM}} = \frac{\sigma_{\mathrm{y}}(T)}{\sigma_{\mathrm{vM}}} \tag{14}$$

For brittle materials, such as graphite, the Mohr-Coulomb failure criterion is appropriate. It is especially suitable for brittle uneven materials in mostly compressive state [10]. The Mohr–Coulomb safety factor is defined as [27]

$$\mathrm{SF}_{\mathrm{M\text{–}C}} = \left(\frac{\sigma_1}{\sigma_{\mathrm{T}}} + \frac{\sigma_3}{\sigma_{\mathrm{C}}}\right)^{-1} \tag{15}$$

where the σ_1 is compared against the tensile strength σ_{T} and σ_3 is compared against the compressive strength σ_{C}. If σ_1 is not tensile, that term is omitted, and likewise for the compressive term if σ_3 is not compressive.

Christensen [28] formulated another failure criterion considering different tensile and compressive strengths of the material. The failure criterion is defined as

$$\left(\frac{1}{\sigma_{\mathrm{T}}}-\frac{1}{\sigma_{\mathrm{C}}}\right)(\sigma_{11}+\sigma_{22}+\sigma_{33}) + \frac{1}{\sigma_{\mathrm{T}}\cdot\sigma_{\mathrm{C}}}\left\{\frac{1}{2}\left[(\sigma_{11}-\sigma_{22})^2+(\sigma_{22}-\sigma_{33})^2+(\sigma_{33}-\sigma_{11})^2\right] + 3(\sigma_{12}^2+\sigma_{23}^2+\sigma_{31}^2)\right\} \le 1 \tag{16}$$

and

$$\sigma_1 \le \sigma_{\mathrm{T}} \quad \text{if} \quad \frac{\sigma_{\mathrm{T}}}{\sigma_{\mathrm{C}}} < \frac{1}{2} \tag{17}$$

The Christensen and Mohr–Coulomb yield surfaces are compared in a two-dimensional case in Figure 23. The material strengths correspond to the graphite used in the dump core with a tensile strength of 40 MPa and compressive strength of $\sigma_C = 130$ MPa. Compared to the Mohr–Coulomb criterion, the Christensen failure surface shows reduced strength in multiaxial tension but increased strength especially in multiaxial compression. [28]

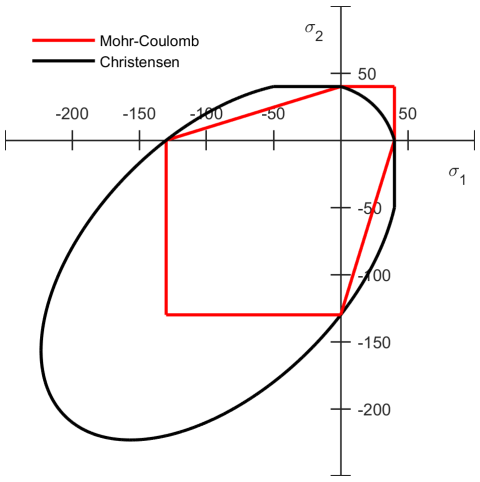

Figure 23. Comparison of the Mohr–Coulomb and Christensen failure surfaces in two-dimensional case for a material with $\sigma_T = 40$ MPa and $\sigma_C = 130$ MPa.

3.5 Previous Studies

Design documents and technical drawings are available from the time the current dumps were designed in the 1970s. Although the design tools of the time differ from today, they can offer ideas and comparison points for the design of the new dumps. The most efficient material of the core for medium lengths around 15 cm was found to be copper [29]. This reflects the current dump core which has a length of 13 cm in the beam direction. The peak temperature in the dump core was foreseen to stay below 400 °C [30].

Some usage limits for the current Internal Dumps were proposed in 1985: The current dumps can be used at all proton energies with intensities up to 1.25×10^{13} protons/second, excepting the following restrictions: The number of protons dumped annually should not exceed 5×10^{18}. For comparison, the new dumps are estimated to dump 2.4×10^{17} protons annually spread over the two dumps [11]. Additionally, the temperature limits of the magnets immediately downstream of the dumps should not be exceeded. These limits as dumped protons per second are estimated as: [31]

- 6 hours at 3×10^{12} protons/s
- 1 hour 30 minutes at 6×10^{12} protons/s
- 20 minutes at 1×10^{13} protons/s

If the limits are exceeded the dump should not be used until time for cool down is allowed.

In the beginning of the new dump design project the status of the current dumps with a copper core with future post-LIU beams was studied with FLUKA. Parameters for a worst-case current and future beam were chosen as presented in Table 1. The future worst-case beam intensity is five times higher than currently.

Table 1. Comparison of the worst-case current and future beams used in the previous FLUKA simulations [32].

		Current beam	Future beam
Intensity	[ppp]	1×10^{13}	5×10^{13}
Momentum	[GeV/c]	26	26
Spot size ($\sigma_\mathrm{h} \times \sigma_\mathrm{v}$)	[mm × mm]	2×2	2×2
Pulse period	[s]	2.4	2.4

The dumps in straight sections 47 and 48 were modeled along with the nearby magnets as shown in Figure 24. The dump core and the radiation shielding were modeled. The adiabatic peak temperature increase was calculated for the future and the current beam using Equation (5) with $c_p = 385\,\mathrm{J/(kg\,K)}$ and $\rho = 8960\,\mathrm{kg/m^3}$. For the current beam, a peak temperature increase of 79 °C was calculated in a single beam impact. For the future beam, a temperature increase of 395 °C was calculated. Thus the core would exceed in a single impact the maximum allowable temperature in copper, which was assumed to be 300 °C. Based on these studies it was decided that a new dump core and radiation shielding are needed [4].

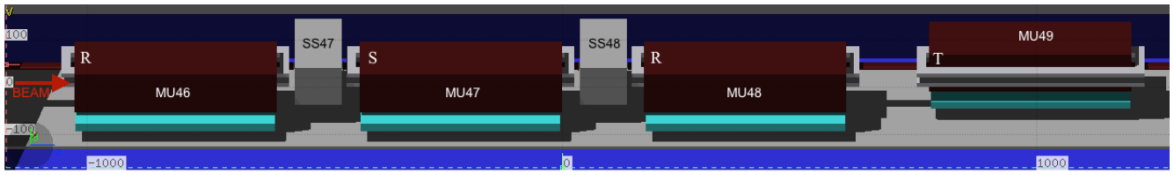

Figure 24. Geometry used in the previous FLUKA simulations. The geometry includes the dumps in straight sections 47 and 48, as well as the surrounding magnets. [32]

According to the previous simulations, the dumps act more as beam scatterers or dilutors than actual dumps: The current dump and shielding in straight section 47 absorb only 20% of the dumped beam energy. The magnet 47 downstream absorbs 21% and the magnets 48 and 49 absorb 13% combined. Around 21% escapes the simulated geometry, mostly continuing downstream along the vacuum pipe. The remaining 25% is deposited elsewhere, mostly in the tunnel walls. [32]

The effect of the particle showers from the dumping on the downstream magnets was also studied. The most critical magnet in terms of energy deposition is the first magnet after the dump (magnet MU47 for the dump SS47), as shown by the energy deposition map in Figure 25. The energy deposition leads to temperature increase that can damage various components of the magnet. For example, the yoke lamination should not exceed 60 °C and the coil insulation should not exceed 50 °C [4]. It was suggested that the new dump design "should be sufficient to prevent the magnet MU47 from the extensive heating, in the best case it should keep the same values of the power

dissipated during dumps for an increased beam intensity" [32]. Another suggested goal is to "avoid the possible material damage in the dump core" [32]. In addition to instantaneous energy deposition and temperature increase, the radiation dose and radioactivation of the surroundings was studied. [32]

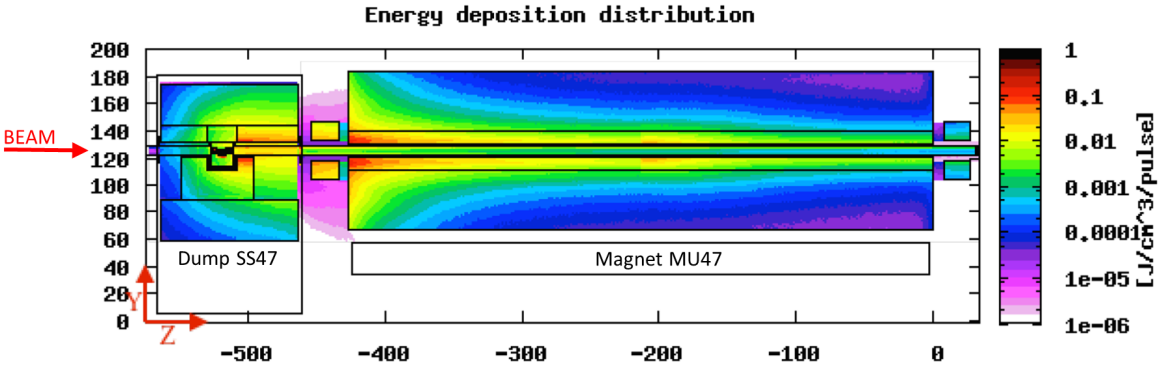

Figure 25. Energy deposition map from FLUKA in the dump in the straight section 47 and the magnet downstream. Energy escaping from the dump is shown to be deposited in the magnet downstream. Figure adapted from [32].

The previous FLUKA studies discussed above assumed a direct impact in the center of the dump core. Some preliminary core designs have been studied based also on the assumption of a direct impact [32–34]. The outcomes of the previously studied designs are not directly applicable to the design presented in this thesis as the multi-turn beam shaving process is fundamentally different to a direct impact in the center.

4 Design of the New Dump Core

4.1 Design and Requirements

The preliminary design of the new Proton Synchrotron Internal Dump and its core was introduced in Section 2.2. The core consists of two main beam impacted materials: graphite and CuCrZr. Additionally, stainless steel is used for the cooling circuits and support structures. The new dump core design is presented and annotated in Figure 26.

The dump core will shave the circulating beam during multiple beam revolutions as described in Section 3.1. The protons will first impact in the the low-density graphite, suffering interactions and depositing energy. The purpose of the graphite is to dilute the beam and protect the denser CuCrZr downstream, which will absorb more energy. The core acts in actuality more as dilutor than a dump, absorbing only approximately 10% of the beam energy.

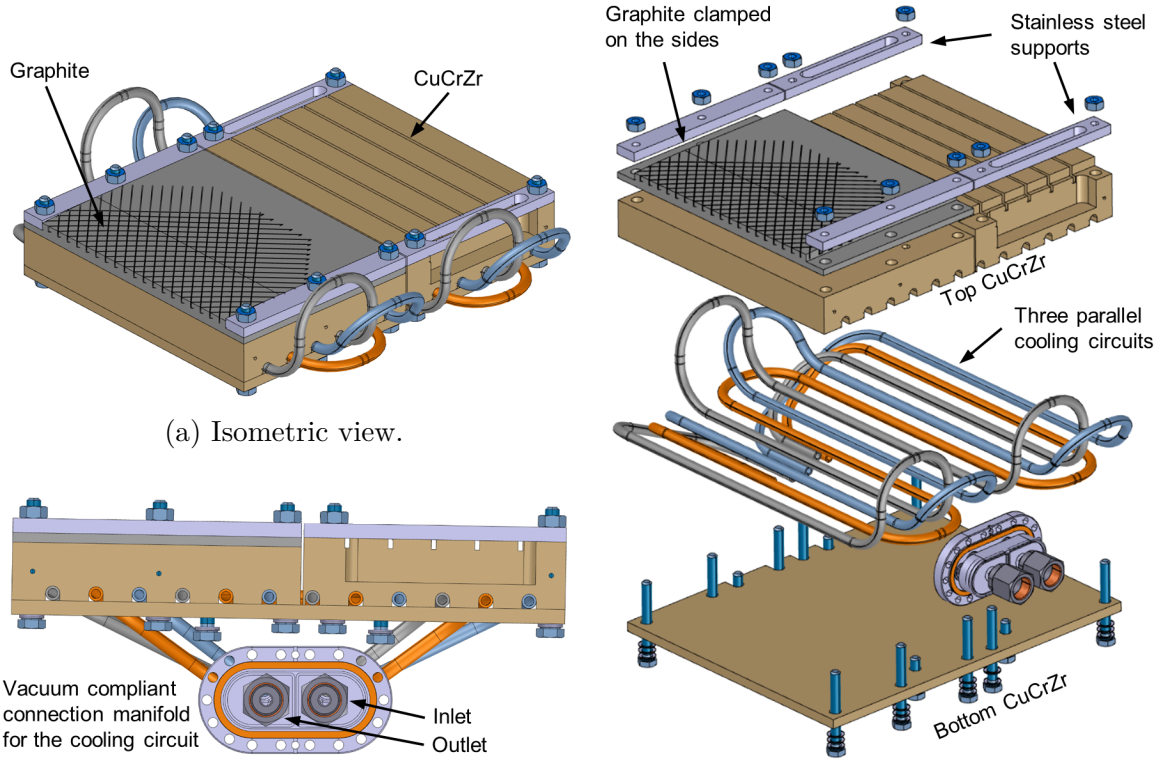

(a) Isometric view.

(b) Side view.

(c) Exploded view.

Figure 26. Overview of the new dump core.

The new dump core design weighs approximately 13 kg and has the dimensions of 180 mm × 40 mm × 230 mm as presented in Figures 27 and 28. The graphite is 120 mm long, which was found to be sufficient to dilute the beam and protect the downstream CuCrZr. The remaining 110 mm in length is CuCrZr. The thickness of the graphite is 10 mm and the total thickness is 40 mm in order to have space for the cooling pipes away from the particle showers generated during the dumping.

The dump core is aligned with a one degree angle with respect to the beam as shown in Figure 28. A surface completely parallel to the beam would be unfeasible to manufacture and align. An incorrect alignment could cause the protons to impact the downstream edge of CuCrZr, possibly damaging the material and increasing the escaping energy as the beam scatters from the downstream edge. Therefore, a controlled alignment angle is set.

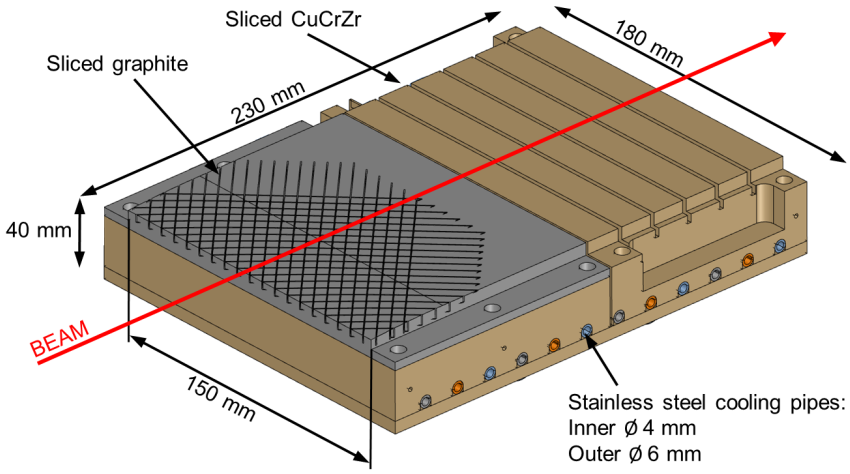

Figure 27. Isometric view of the beam interacting materials of the new dump core.

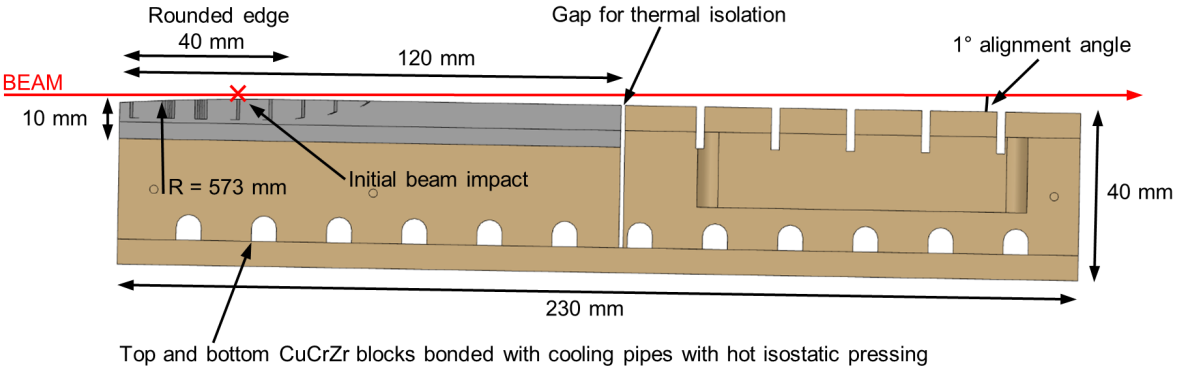

Figure 28. Side view of the beam interacting materials of the new dump core.

The CuCrZr downstream heats up more than the graphite upstream, which should be kept as cool as possible to reduce outgassing to vacuum. Therefore, the downstream half of the core is isolated from the upstream half with a gap to disallow thermal conduction.

The graphite part will be clamped to the CuCrZr part with bolts on the sides. Applying pressure on the contact surface is critical as it increases thermal conduction through the contact [35]. The pressure should be as uniform as possible and guaranteed for the lifetime of the core. The clamping design is still preliminary and further improvements are foreseen. There are also other possible methods to bond the graphite to CuCrZr for a better thermal contact, for example with brazing.

The stainless steel cooling circuits are located between the top and bottom CuCrZr blocks. Three ways of bonding the pipes have been considered: The simplest way is to clamp the pipes between the two CuCrZr blocks. The second way is to braze the pipes to the CuCrZr, resulting in a better thermal contact. Neither of these methods guarantee an uniform thermal contact and result in a thermal barrier between the top and bottom CuCrZr blocks. This may result in high stresses and deformations at elevated temperatures due to temperature mismatches.

The preferred method of bonding the cooling circuits is diffusion bonding by hot isostatic pressing (HIP). During the process the materials are heated to 950 °C for 3 hours under a pressure of 100 MPa, resulting in a perfect contact. CuCrZr to stainless steel pipe bonding by HIP has been successfully tested in another project at CERN [36]. The compatibility of the preliminary core design with the HIP process is under study. Bonding by HIP is the baseline considered in the simulations of the design.

Demineralized water is used in the cooling circuits. The flow rate in the circuits is undefined at this stage, but the current dumps have a flow velocity of approximately 1.5 l/min in the core, resulting in a velocity of 0.66 m/s. The flow velocity should be in the range of 0.5–2 m/s to prevent corrosion according to [37].

The surfaces of graphite and CuCrZr are proposed to be sliced to allow free thermal expansion and as a result alleviate stresses. The graphite is planned to be sliced bidirectionally in 5 mm by 5 mm blocks with a slice depth of 5 mm. The CuCrZr is sliced perpendicular to the beam with 2 mm wide and 10 mm deep slices.

The first main objective of dump core design, as introduced in Section 2.2, is to ensure the mechanical integrity of the dump core material in beam impact. The survival of the core will be studied from the point of view of maximum temperature, failure criteria, fatigue and long-term radiation damage. The methods of study and proposed material limits are presented in Table 2.

Table 2. Proposed design criteria, methods of study and material limits.

		Limit	
Criteria	Method of study	Graphite	CuCrZr
Maximum temperature	Finite element analysis	2000 °C	300 °C
Failure	Finite element analysis	Mohr–Coulomb failure criterion $\sigma_T = 40$ MPa $\sigma_C = 130$ MPa	Von Mises yield criterion $\sigma_y = 282$ MPa (at 25 °C)
Fatigue	Compare simulation stress results with literature	Sufficient lifetime (not explicitly defined)	
Radiation damage	Compare simulated DPA values with literature	No critical damage (not explicitly defined)	

The dump actuation mechanism is required to perform 200 000 movement cycles per year [11]. Most of these cycles are either dumping low intensity beams or no beam at all. The number of high intensity beam dumps is not precisely defined, but is expected to be in the order of few hundreds or thousands per year.

4.2 Material Selection

Material selection is an important aspect of dump design. The materials should be able to withstand beam impacts considering the theory presented in Section 3. The approach for the material selection of the core is to place low-density and high thermal shock resistant material upstream of the beam and higher density material downstream of the beam. The low-density material protects the high-density materials by diluting the beam before it impacts the high-density material, which absorbs more beam energy. The considered materials should also have a high thermal conductivity as it lowers the temperatures reached in the shaving surface and is also beneficial to the cooling performance. Other material considerations include good availability, vacuum compatibility, radiation hardness, reliable manufacturing processes and good characterization of properties at high temperatures.

After studying several candidates two materials were selected for the new dump core as described in Section 4.1: graphite SGL SIGRAFINE® R7550 and a precipitation hardened copper alloy copper–chromium–zirconium. Additionally, stainless steel 316L was selected for the cooling pipes. The properties of the materials at room temperature are summarized in Table 3. The properties varying with temperature are plotted in Figure 29 and the material data values are tabled and referenced in Appendix 1.

Table 3. Material properties at room temperature ($T = 22\,°\mathrm{C}$).

			Graphite SGL SIGRAFINE® R7550	CuCrZr	Stainless steel 316L
Density	ρ	[kg/m^3]	1830	8895	7977
Thermal conductivity	λ	[W/(m K)]	107	330	12.9
Specific heat	c_p	[J/(kg K)]	707	418	475
Mean CTE	α	[ppm/K]	4.0	15.2	16.0
Young's modulus	E	[GPa]	12.8	137	195
Poisson's ratio	ν	[-]	0.14	0.34	0.3
Yield strength	σ_y	[MPa]	–	282	297
Tensile strength	σ_T	[MPa]	40	400	602
Compressive strength	σ_C	[MPa]	130	–	–
Temperature limit	T_limit	[°C]	2000	300	–

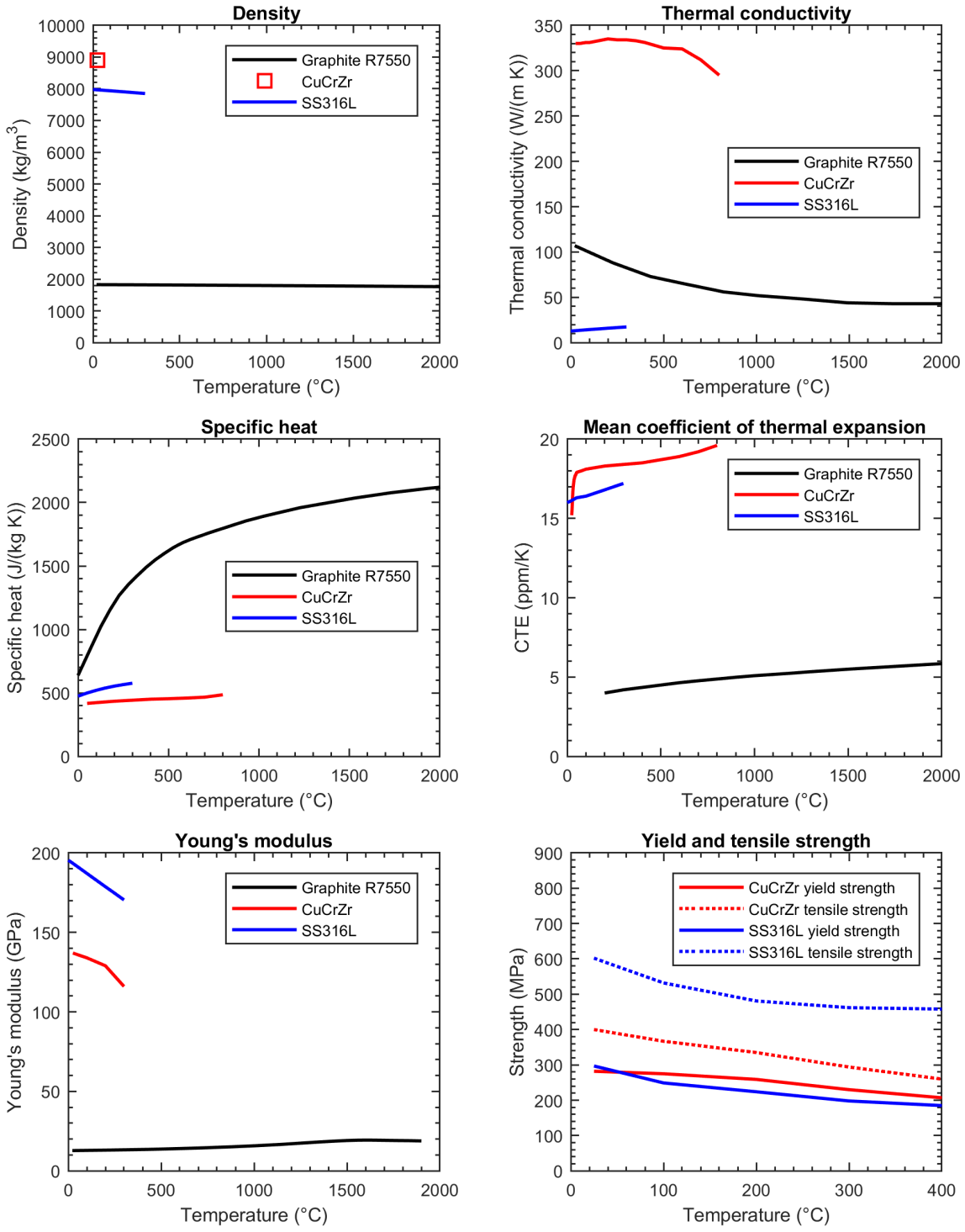

Figure 29. Temperature dependent material properties. The values are referenced and tabled in Appendix 1.

Graphite R7550 is a fine-grain isostatically pressed graphite from SGL Group made for high-temperature applications. Graphite was selected as the material for the shaving surface due to its low density leading to low energy deposition. The material has high temperature resistance and good stability at temperatures up to at least 2000 °C. The stresses induced in graphite by a temperature increase are also low due to its low CTE and Young's modulus. Graphite R7550 is also known at CERN and it is used in other

beam interacting devices, for example in the SPS internal dump TIDVG#4 [38]. [39]

Graphite exhibits nonlinear elastic and plastic behavior as presented in Figure 30. Even at low stresses permanent strains are set after unloading. The stress-strain curve is then continued after the previous maximum stress is exceeded. The plastic strains can be recovered by annealing at high temperatures, but the temperatures and time-scales needed are considered too high to be reached in the core during dumping operation. Additionally, the strength of graphite is increased at elevated temperatures [39]. [25]

Graphite is a porous material with a high gas content [40]. These gases can desorb from graphite into vacuum and increase the vacuum pressure, disturbing the beam and other accelerator equipment [41, 42]. The outgassing rate is increased at elevated temperatures. The outgassing rate can be reduced by removing absorbed gas molecules by baking-out the graphite at a high temperature for an extended time [41, 42]. To limit the outgassing, the operational temperature and volume of the graphite should be minimized.

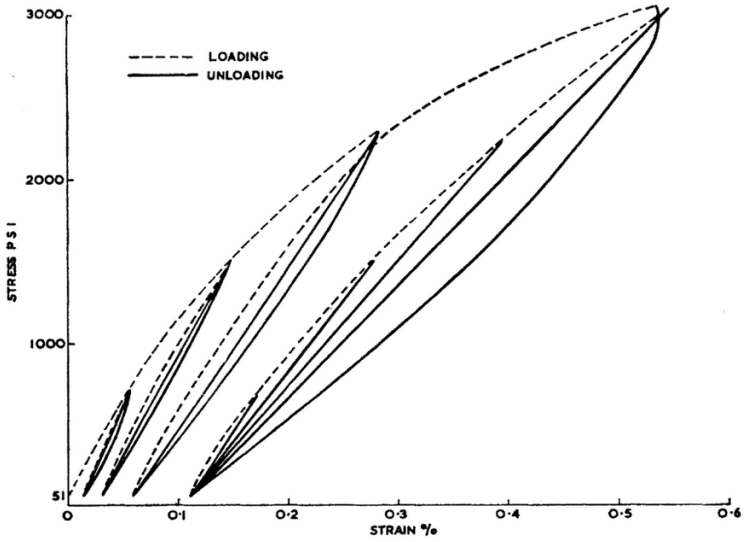

Figure 30. Stress-strain curve for a nuclear graphite under repeated compressive loading showing nonlinear elastic and plastic behavior [25].

CuCrZr is a precipitation hardened copper alloy with added 0.5–1.5 weight percent chromium and 0.03–0.3 weight percent zirconium [24]. It has a density higher than graphite and therefore it absorbs more beam energy. Similarly to pure copper, CuCrZr has a good thermal conductivity, making it ideal for cooling performance. The material also shows high strength, ductility and radiation resistance [23]. CuCrZr has been used in other CERN projects (e.g. TIDVG#4 [38]) and its properties have been characterized in a testing campaign at CERN in 2017. To obtain a good combination of strength, ductility and thermal conductivity, the CuCrZr will be solution annealed, quenched and aged. The maximum allowable temperature in CuCrZr is considered to be 300 °C to avoid softening due to annealing [20].

Stainless steel 316L was selected as the material of the cooling pipes due to its good availability, low cost, ease of manufacturing and resistance to water flow corrosion.

For the study of the radiation damage, peak DPA values of 0.03 DPA/year in graphite and 0.002 DPA/year in CuCrZr have been simulated in FLUKA. The accumulated total over a 20 year lifetime is 0.6 DPA in graphite and 0.04 DPA in CuCrZr. The peaks occur locally on the shaving surface and were calculated assuming a beam always impacting in the same position. The values were calculated considering 2.4×10^{17} protons dumped per year per dump, which is conservative as the dumped protons should be spread over the two dumps [11].

As the dump core has to withstand numerous beam impacts, fatigue of the materials is a concern. The fatigue lifetime of the core is evaluated by comparing the simulation stress results with fatigue lifetime curves found in literature. The fatigue characteristics of a material are affected by both the temperature of the material and by the irradiation damage.

Example fatigue lifetime curves for CuCrZr tested at 300 °C with different treatments, irradiation conditions and holdtimes are presented in Figure 31. Irradiation is found to increase the number of cycles to failure due to the increase in yield strength, although at higher a testing and irradiation temperature the effect is no longer noticeable. [43]

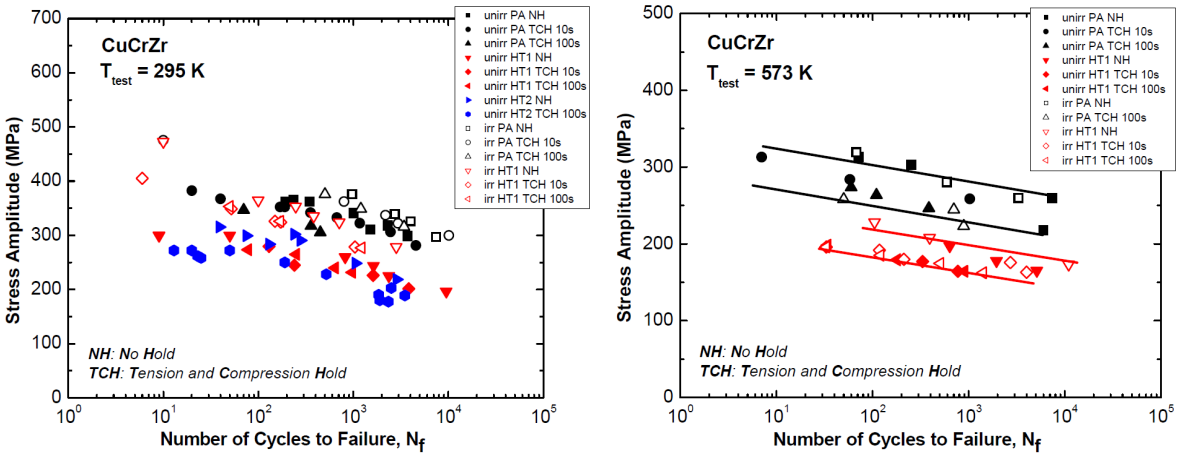

(a) (b)

Figure 31. Fatigue testing of CuCrZr samples with different treatments, irradiation conditions and holdtimes. Samples tested at (a) 295 K and (b) 573 K with fully reversed load cycles (R=−1). Samples neutron irradiated at (a) 333 K and (b) 573 K to a dose range of 0.2 − 0.3 DPA. Conditions: prime aged (PA) and prime aged and annealed in vacuum at 873 K for 1 hour (HT1) or 4 hours (HT2). [43]

Fatigue data for the exact graphite grade used in the core, SGL SIGRAFINE® R7550, was not found. Roberts [44] measured fatigue characteristics for another fine-grain graphite NBG18 from SGL Group. In multiaxial compressive loading, the strength and fatigue life is shown to improve, i.e. the minimum principal stress reaches values higher than the ultimate compressive stress. This supports the conclusion of the Christensen failure criterion of increased strength in multiaxial compression.

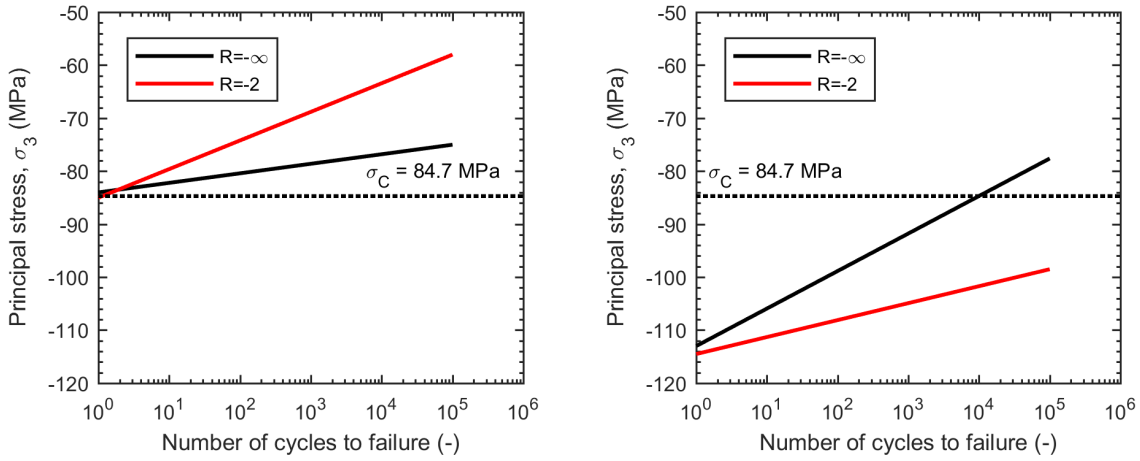

Figure 32. Fatigue lifetime curves for fine-grain NBG18 graphite for (a) uniaxial and (b) multiaxial compressive loading with R=$-\infty$ and R=-2. The minimum principal stress in multiaxial compressive loading is shown to exceed the compressive strength $\sigma_C = 84.7$ MPa. Figure adapted from [44].

4.3 Beam Scenarios

The beam scenarios to be considered for the design, as set in the functional specifications document [11], are presented in Table 4. The beams have been selected from [14], considering high intensity, high momentum and a small size to be critical for the core integrity as they lead to a higher energy density in the beam. The beam scenarios are assumed to be dumped at their maximum momentum. The beam energies are calculated with Equations (1) – (3). The beam sizes are based on the odd numbered straight sections of the PS, corresponding to the dump in the straight section 47. The vertical beam spot sizes are smaller in odd straight sections than in even, which leads to higher temperatures since the beam is shaved faster. The beam profiles are plotted in 33. The other dump will be installed in the even straight section 48.

LHC 25ns HL–LHC is the baseline beam considered for the design, as it combines high intensity with a small spot size and it is an operational beam that could be dumped regularly. It is accelerated to a maximum momentum of 26 GeV/c and extracted to the SPS on the way to the LHC.

The Highest Intensity beam is the most intense beam foreseen possible to be accelerated to 26 GeV/c in the Proton Synchrotron. The dumping of such a beam is considered as an accidental scenario that will not occur regularly [11]. Therefore, it is also not considered in fatigue studies.

SFTPRO and LHC 25ns HL–BCMS are studied but considered less critical than the HL-LHC beam. The SFTPRO beam has a lower momentum and intensity than HL–LHC, but the pulse period is the lowest of the beams at 1.2 s. The destination of the SFTPRO beam is the fixed targets in the North experimental area. The HL–BCMS beam has a smaller size than HL-LHC, but it is also less intense. The LHC is the destination of the HL–BCMS beam. [11]

The dumps should also be capable of dumping ion beams (mainly lead ions), but they are not studied at this time as they are not considered critical for the design due to their low intensity (1×10^{11} ions per pulse). [11]

Table 4. Proton beam scenarios to be considered for the design according to the functional specifications document [11].

	Highest Intensity	LHC 25ns HL–LHC	SFTPRO	LHC 25ns HL–BCMS
Particle type	Proton	Proton	Proton	Proton
Pulse intensity [ppp]	5×10^{13}	2.4×10^{13}	2×10^{13}	1.6×10^{13}
Number of continuously dumped pulses to consider	Min. 3	Min. 4	Min. 2	Min. 4
Beam revolution time [µs]	2.1	2.1	2.1	2.1
Pulse period [s]	2.4	3.6	1.2	3.6
Number of bunches	Considered fully debunched in the simulations			
Beam spot size in odd sections ($\sigma_h \times \sigma_v$) [mm × mm]	3.10×1.45	1.74×0.87	3.68×1.99	1.65×0.77
Max. beam momentum [GeV/c]	26	26	14	26
Beam energy [kJ]	201	96.4	80.4	64.3

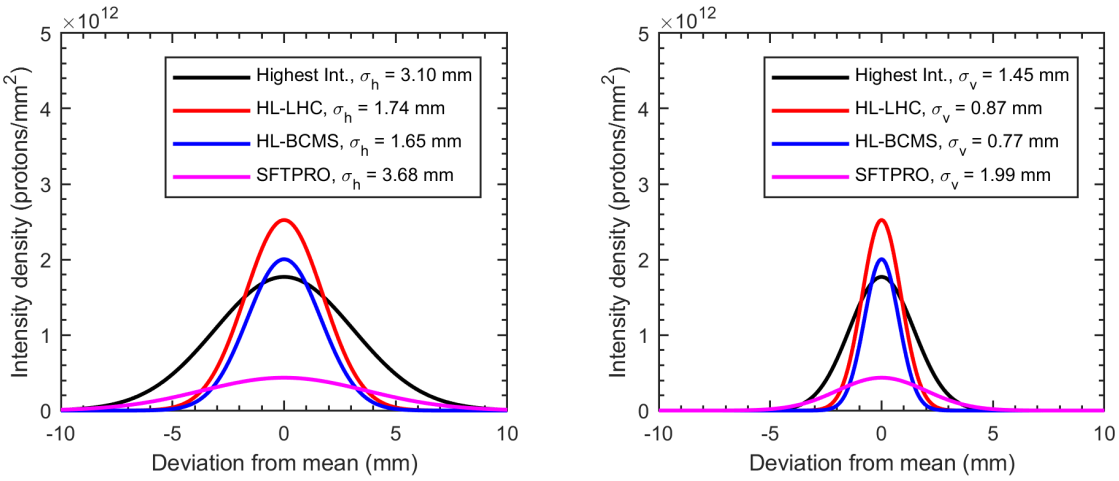

(a) Horizontal. (b) Vertical.

Figure 33. The (a) horizontal and (b) vertical Gaussian profiles of the considered beam scenarios. The spot sizes correspond to the dump in the odd straight section 47 of the Proton Synchrotron.

5 Simulation Methodology

5.1 Overview

The fulfillment of the design criteria presented in Table 2 are studied with finite element simulations. Several simulation cases are selected based on the requirements and the beam scenarios presented in Section 4.3. The LHC 25ns HL–LHC beam is taken as a baseline beam for the simulations, as it is the worst-case operational beam foreseen to be dumped regularly. The studied simulation cases and their topics of study are presented in Table 5. ANSYS Workbench 17.1 software is used to perform the finite element simulations.

Table 5. Studied simulation cases and their topic of study.

Simulation case	Topic of study
Dumping one pulse of LHC 25ns HL–LHC beam (thermal and structural)	Maximum temperatures and mechanical integrity of the core during the dumping of a single pulse
Continuous dumping operation until a steady-state is reached (thermal only)	Performance of the cooling system
Dumping four pulses of LHC 25ns HL–LHC beam after steady-state (thermal and structural)	Maximum temperatures and mechanical integrity of the dump core in continuous dumping operation
Dumping one pulse of Highest Intensity beam (thermal and structural)	Maximum temperatures and mechanical integrity of the core during the dumping of a single accidental pulse
Dumping one pulse of LHC 25ns HL–BCMS and SFTPRO beam (thermal only)	Comparison of the considered beam scenarios
Sliced graphite block geometry. Dumping one pulse of LHC 25ns HL-LHC and Highest Intensity beams (thermal and structural)	The effect of slicing the graphite

The basis of all simulations is the heat generation load imported from FLUKA simulations. The load application process is described in Section 5.3. The simulations are one-way coupled: Heat generation input from FLUKA is imported to the thermal simulations. The temperatures obtained from thermal simulations are then imported to the structural simulations to calculate the stresses and deformations.

A simplified core geometry modeled in ANSYS is presented in Figures 34 and 35. The geometry is based on the dump core design presented in Section 4.1. Only half of the geometry is modeled and a symmetry plane is applied. The beam is assumed to impact centered on the symmetry plane. The geometry differs slightly and the supporting structures are omitted in order to simplify the model. The slices in CuCrZr are modeled, but the graphite is not sliced in the full model. Instead the slicing of the graphite will be studied by modeling a single sliced block of graphite, as described in Section 6.8.

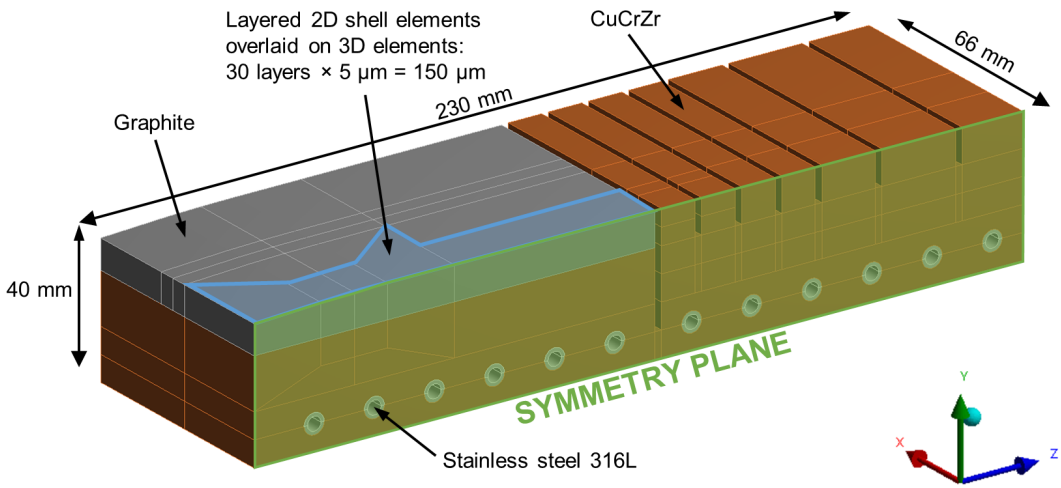

Figure 34. Isometric view of the core model in ANSYS.

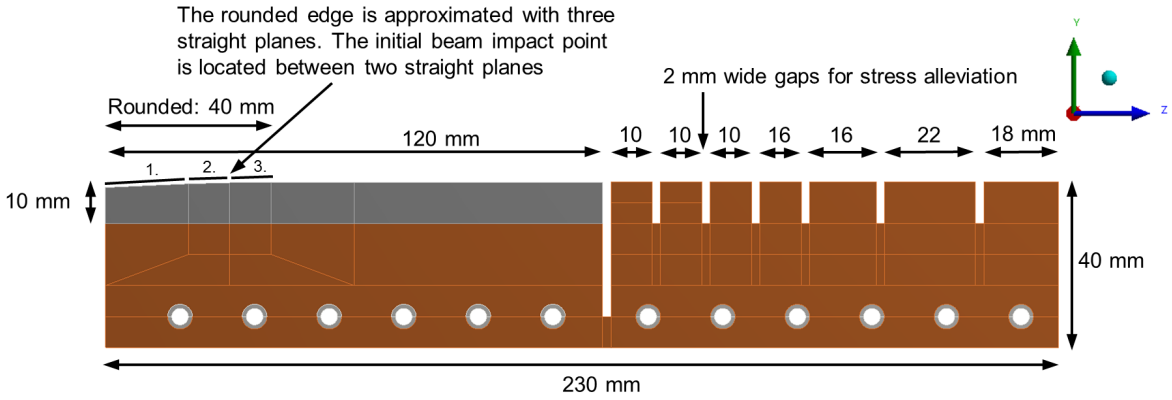

Figure 35. Side view of the core model in ANSYS.

Two-dimensional layered shell elements (SHELL131/SHELL181 thermal/structural elements [27]) are overlaid on the 3D elements on the beam shaving surface. They contain 30 layers with a thickness of 5 µm each, for a total thickness of 150 µm. The layered shell elements allow through thickness thermal conduction, different heat generation input on every layer, and modeling of structural effects. Therefore, they are used for the import of the very localized heat generated by the multi-turn shaving beam impact. With the layered shell elements, the shaving shaving can be modeled with a reasonable number of elements with acceptable aspect ratios.

The thermal and structural simulations are transient with implicit time integration. The multi-turn shaving process is divided into 20–60 time steps in FLUKA and ANSYS with a length of 150 µs each, for a total dumping time of 3–9 ms. The number of time steps needed depends on the size of the beam and the velocity of the dump core. A core velocity of 0.8 m/s is obtained from simulations of the actuation mechanism, corresponding to an angular movement from −6° to 6° degrees. The range is less than what was presented in Section 2.2, as the range was decided to be reduced to slow down the core. Slower velocity leads to lower temperatures as there is more time for the heat to conduct.

The one degree alignment angle is not implemented in ANSYS, but it is already considered in the FLUKA simulations. A horizontal tune of $Q_\mathrm{h} = 6.33$ is used in FLUKA simulations as it was found to be a worst-case tune. A vertical tune of $Q_\mathrm{v} = 6.23$ is used. The ambient temperature is set at 22 °C as it is the temperature outside the vacuum chamber [11].

5.2 Material Modeling

A temperature dependent isotropic material model for all the materials is implemented in ANSYS, with data ranging from room temperature to the material limit temperatures (300 °C for CuCrZr and 2000 °C for graphite). The implemented material properties are plotted in Figure 29 and tabled and referenced in Appendix 1.

A linear elastic material model is used for all the materials, although graphite exhibits nonlinear elastic–plastic behavior (see Figure 30). The dynamic Young's modulus (tangent at the start of the stress-strain curve) from measurements is used for graphite, as opposed to the measured static Young's modulus (tangent between two points on the stress-strain curve). The approach is conservative as the static Young's Modulus is lower and would lead to lower stresses. The assumption is made to simplify the simulations and as the exact elastic-plastic behavior of the graphite is unknown. Graphite also shows increased strength at elevated temperatures [39], but the strengths will be considered at room temperature in order to be conservative. [25]

The von Mises yield criterion is used to evaluate the integrity of the CuCrZr. A safety factor is calculated by comparing the von Mises yield stress from simulations results to the yield strength with Equation (14). To model the plasticity of CuCrZr and stainless steel, a multilinear isotropic hardening model was implemented in ANSYS, as described in Appendix 1. The accuracy of the plastic model is not of critical importance since the design goal is to remain in the elastic region of the materials.

The Mohr–Coulomb failure criterion is used to evaluate the integrity of the CuCrZr. A safety factor is calculated by comparing the principal stresses from simulation results with the tensile and compressive stresses with Equation (14). No model for the failure or fracture of graphite is implemented in case the stresses exceed the failure criterion.

5.3 Load Application

In these preliminary studies, only the heat load generated by the beam impact is considered. Loads stemming from the movement of the core, fixation or other sources are neglected.

FLUKA is used to obtain the heat generation rate $\dot{q}_V$ required by Equation (6). The core geometry is modeled in FLUKA and volumes where the energy deposition is recorded are set up in either Cartesian or cylindrical coordinates. The volumes are divided into smaller finite volumes called bins. The energy deposited by the proton impact generated particle shower is recorded in these bins. The energy is recorded during 150 µs long time steps and the resulting FLUKA output files contain the deposited power density in GeV/(cm^3 s). An example output file from FLUKA is annotated in Figure 36.

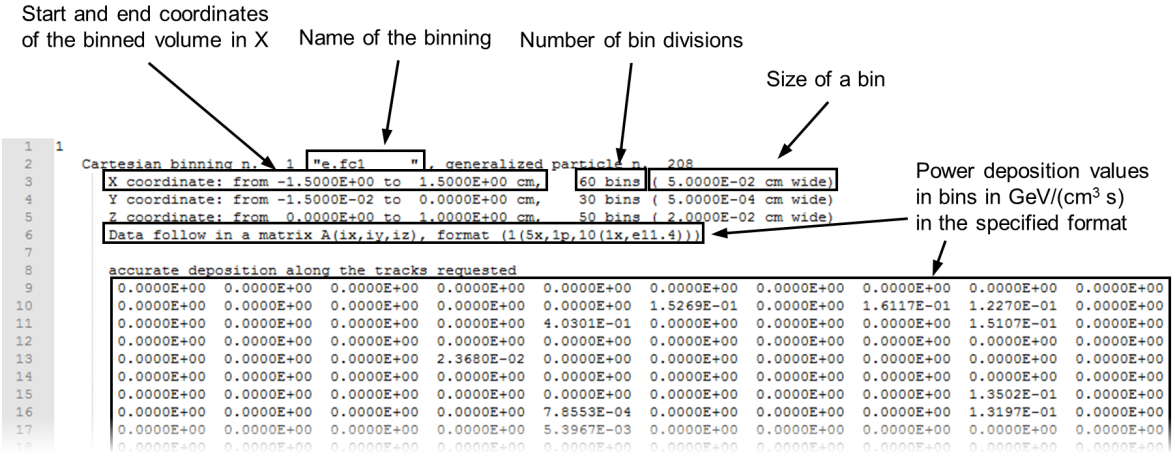

Figure 36. An example FLUKA output file annotated.

The FLUKA file is read into a load table in ANSYS with a script. The load table contains the coordinates of the centers of the bins and the values of the power deposition in those bins. The coordinate system of the load table has to match with FLUKA. The units are converted from GeV/(cm^3 s) to W/m^3 before applying the load to nodes or elements in ANSYS. The heat generation load is applied for the duration of the load step. In case of the PS Internal Dump core simulations, a new FLUKA file is read and applied for each of the 20–60 load steps. An example script to read and apply the FLUKA files is found in the Appendix 3.

In case the mesh nodes do not coincide exactly with the center of the FLUKA bin, ANSYS interpolates the heat generation value linearly from adjacent bins as illustrated in Figure 37. This might lead to unrealistic interpolated values, for example between material and vacuum or on interfaces between different materials.

Some areas of the dump core have higher heat generation, especially on the shaving surface in graphite. Separate finer binnings are used in these areas in FLUKA. As a result, there are multiple FLUKA files covering the complete geometry. The resulting load tables have to be applied to the corresponding nodes or elements in ANSYS. If a load table is applied to nodes or elements outside the FLUKA binning, they use the value of the nearest FLUKA bin, as illustrated in Figure 37.

In practice, to ensure accurate import, the mesh size should match the FLUKA binning. Additionally, the FLUKA binning should be fine enough to not contain large differences in adjacent bins.

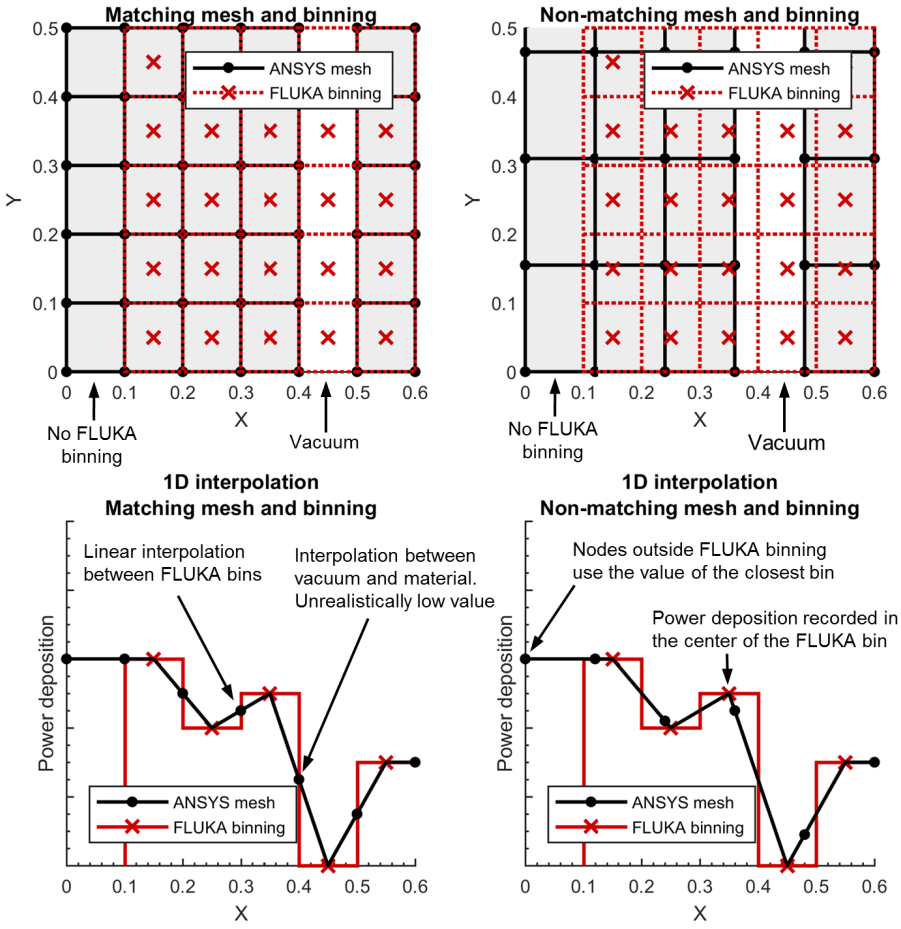

Figure 37. Power deposition import and interpolation from FLUKA to ANSYS with matching and non-matching mesh and binning.

5.4 Elements and Mesh

The geometry is meshed with linear 3D and linear 2D layered shell elements. The same mesh is used in the thermal and structural simulations. The element type used for the 3D elements is SOLID70/SOLID185 (thermal/structural) and for the 2D layered shell elements the type is SHELL131/SHELL181 (thermal/structural).

The thermal layered shell elements SHELL131 have in-plane and through-thickness thermal conduction capability. The elements can be divided into up to 31 layers with temperature degrees of freedom between the layers and a linear temperature distribution through a layer. The nodes of the shell elements are overlaid on the nodes of the 3D elements and the bottom layer temperature is coupled with the 3D elements. The temperature of each layer can then be imported to the structural layered shell elements SHELL181, which allow the bending of shells and the solving of stress results per layer. The displacements of the shell nodes are coupled with the 3D elements, but the rotations are not coupled. However, the rotation of the shells were found to follow the deformation of the 3D elements. [27]

An overview of the mesh and the critical areas in graphite and in CuCrZr are shown in Figure 38. The smallest element size in CuCrZr is 0.5 mm × 0.25 mm × 0.5 mm (X ×

Y × Z). The smallest 3D element size in graphite is 0.5 mm × 0.24 mm × 0.2 mm (X × Y × Z). The 2D layered shell elements on the surface have the same size in X × Z, but they have a virtual thickness of 150 µm divided into 30 layers. The mesh contains approximately 700 000 elements.

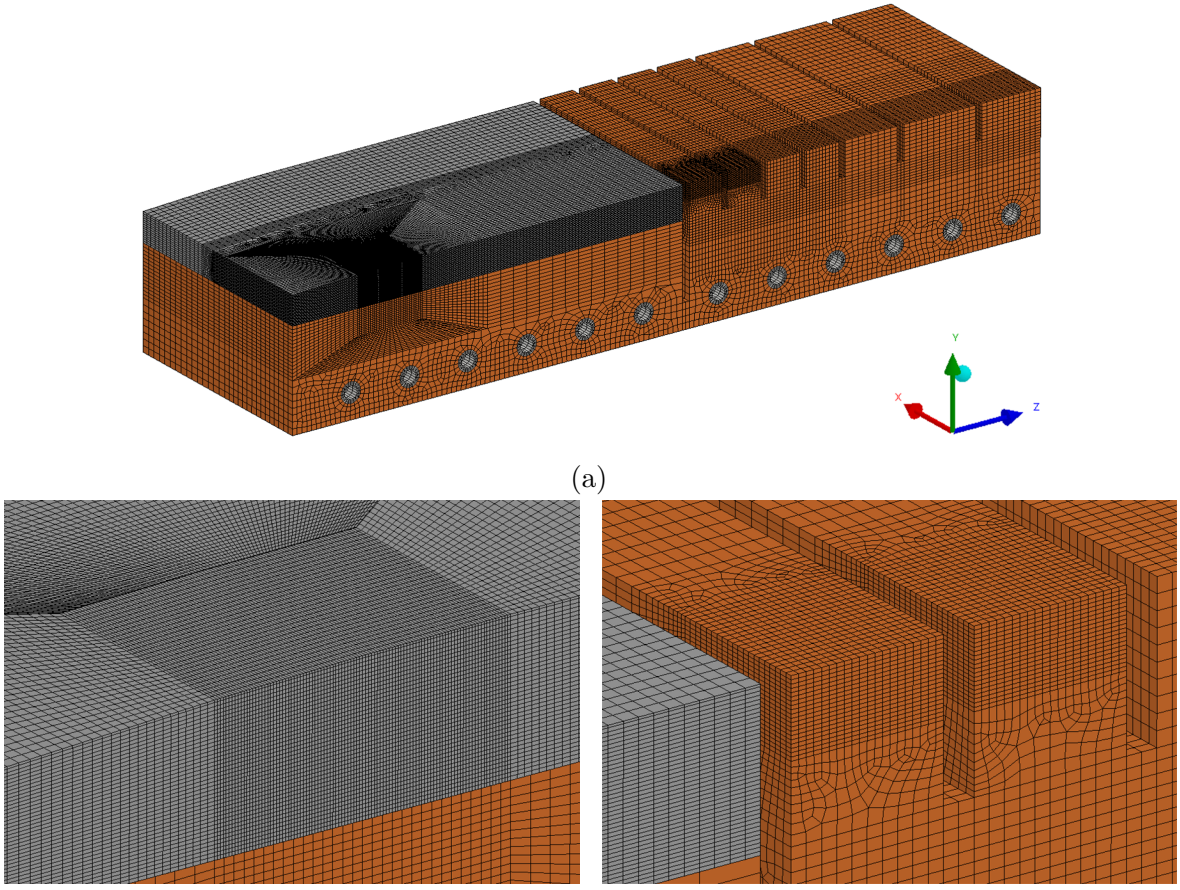

(a)

(b) (c)

Figure 38. (a) Mesh overview and critical areas in (b) graphite and (c) CuCrZr.

5.5 Contacts and Boundary Conditions

There are four thermal interfaces in the core design as presented in Figure 39: between graphite and CuCrZr, between top and bottom CuCrZr blocks, between CuCrZr and cooling pipes and between cooling pipes and water. The heat transfer coefficients for these interfaces are presented in Table 39. The thermal contacts and boundary conditions in the model were setup considering a steady-state where the input and output power are equal. Only the cooling through the cooling pipes is considered. Other thermal boundary conditions, such as radiation or conduction through the shaft, are not considered.

A heat transfer coefficient of 2900 $W/(m^2 K)$ is used between the cooling pipes and water based on analytical calculations performed in Appendix 2. The value corresponds to a volumetric flow rate of 1.5 l/min or a mean flow velocity of 0.66 m/s. A water inlet temperature of 26 °C and an outlet temperature of 48 °C is taken into account. The pipe wall temperature should be limited below the boiling point of water.

A thermal contact conductance of 1000 W/(m^2 K) is used for the graphite to CuCrZr contact. This corresponds to a smooth contact surface with a contact pressure of less than 0.05 MPa as calculated analytically in Appendix 2. For comparison, a contact pressure of around 0.2 MPa was achieved between a graphite block and CuCrZr in the SPS internal dump TIDVG#4 [38].

The CuCrZr is planned to be diffusion bonded with the cooling pipes by hot isostatic pressing, resulting in a perfect bond. As such they are meshed together as one body.

In structural simulations the graphite is bonded with CuCrZr through a "No Separation" contact that allows sliding, but no separation. It is used as it is a linear contact and thus computationally efficient. The graphite is fixed to CuCrZr on the backside as shown in Figure 39. The dump core is fixed from the bottom in a simplified way as shown in Figure 39.

The boundary conditions and contacts in the model are simplified and considered estimates. The cooling performance is planned to be measured during prototyping and commissioning and the heat transfer coefficients will adjusted accordingly.

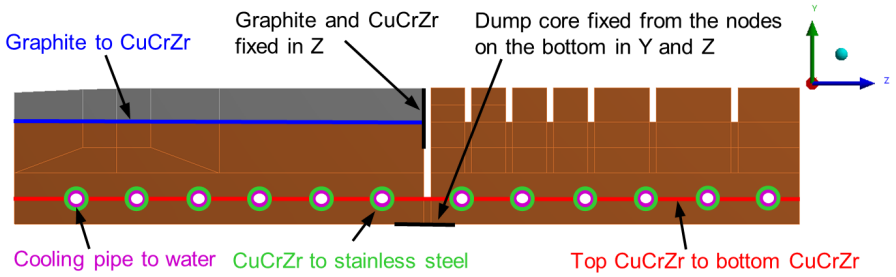

Figure 39. Thermal interfaces and boundary conditions in the model.

Table 6. The thermal interfaces in the model and their heat transfer coefficients.

Contact	Heat transfer coefficient [W/(m^2 K)]	Notes
Graphite to CuCrZr	1000	Selected considering analytical calculations (see Appendix 2).
Top CuCrZr to bottom CuCrZr	Perfect contact	Perfect contact by diffusion bonding.
CuCrZr to stainless steel	Perfect contact	Perfect contact by diffusion bonding.
Cooling pipe wall to water	2900	Calculated analytically (see Appendix 2). Water inlet at 26 °C and outlet at 48 °C.

6 Results

6.1 Load Application Verification

To verify the load import and application, the total energy and the peak power density are compared between ANSYS and FLUKA. The total energy imported to ANSYS is obtained by fixing the material density and the specific heat and simulating the dumping of a full beam pulse. Sufficiently long time is simulated after the beam pulse to allow the heat to distribute uniformly. The total energy can then be obtained by calculating an average energy density with Equation (5) and multiplying it with the volume of the model, read from ANSYS (times two to account for the half model).

For the calculation of the peak power density, one time step is selected. A special material with fixed density, specific heat and no thermal conduction is used. The adiabatic temperature increase in the selected time step is calculated with ANSYS and converted to energy density with the equation Equation (5). The peak power density is then obtained by dividing the peak energy density with the length of the time time step.

The total energy and peak power density are compared between FLUKA and ANSYS for the baseline HL-LHC beam in Table 7. The integrated energy deposition map for a complete beam pulse is presented in Figure 40. The power deposition density on the shaving surface along the symmetry plane is plotted in Figure 41. A total energy of 8.07 kJ is deposited in the dump core, which is 8.4% of the total beam energy of 96.4 kJ from Table 4. A high and sharp peak temperature can be observed at 30 mm in length, at the joint of two straight planes used to approximate the rounded edge as described in Figure 35. It is also the location where the protons first impact the dump core.

The total energy and peak power density imported are in fairly good agreement between FLUKA and ANSYS. Individually applied energy deposition by material shows some error, possibly due to the change in material density at the interface, and the resulting interpolation error. There is a −19% relative error in the peak power deposition in CuCrZr due to the statistical noise in the FLUKA input, as seen in Figure 41, that is smoothened in the import process.

Table 7. Results of the load import verification studies for a HL–LHC beam pulse.

		FLUKA	ANSYS	Relative error
Total energy deposited	[J]	8068	8066	−0.025%
in graphite	[J]	600.7	643.0	7.04%
in CuCrZr and stainless steel	[J]	7468	7407	−0.82%
Peak power density deposited (in 28th time step)				
in graphite	[GeV/(cm^3 s)]	3083	3021	−2.1%
in CuCrZr	[GeV/(cm^3 s)]	53.11	42.94	−19%
in graphite (sliced block model)	[GeV/(cm^3 s)]	3083	2988	−3.1%

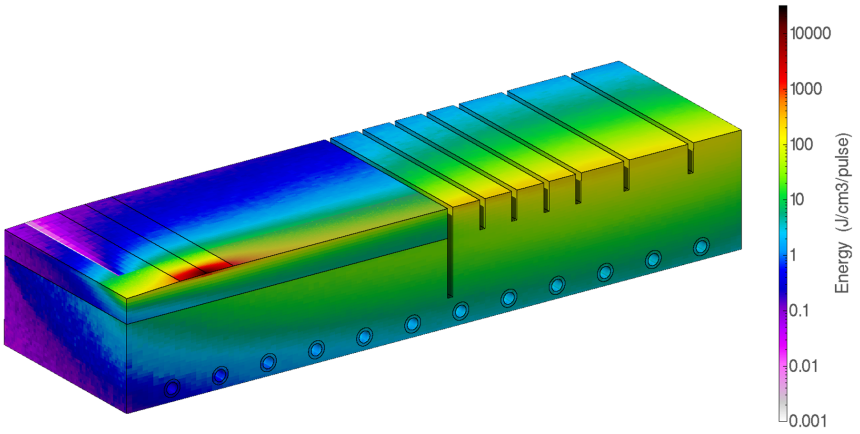

Figure 40. Integrated energy deposition map from FLUKA for the dumping of a single HL–LHC beam pulse.

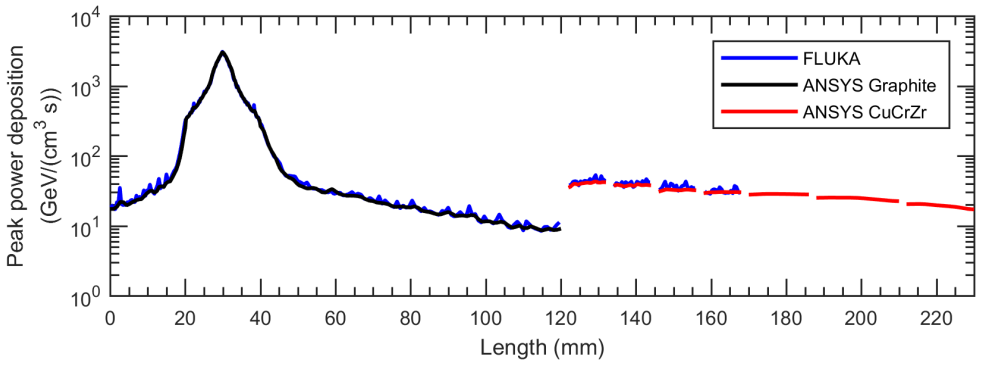

Figure 41. Peak power deposition along the shaving surface for the 28th time step of a HL–LHC beam pulse.

6.2 Mesh Sensitivity

The sensitivity of the maximum temperature and the Mohr-Coulomb safety factor to the mesh size is studied with the sliced graphite block model introduced in Section 6.8. The mesh convergence curves are plotted in Figure 42. The convergence studies were performed with 2D elements on the shaving surface. For comparison, the results for 3D elements on the surface, with a size corresponding to the 2D elements, are also presented. The results for the full model is also presented for comparison. The mesh is refined in the two surface directions (X and Z) and in the thickness direction (Y) separately. The mesh size in thickness (Y) refers to the elements below the 2D shells.

Based on the convergence curves, refining the mesh in X or Z does not affect the results significantly, while refining in the thickness direction (Y) has more effect. The mesh size in Y shows little change with sizes below 0.05 mm. Therefore, the mesh size used (0.05 mm in all directions) in the graphite block simulations is considered converged. Additionally, the results with 3D elements show good agreement with results of the 2D layered shell elements, supporting the modeling approach. The mesh size used in the full model is not completely converged, and a slight increase in maximum temperature or decrease in Mohr–Coulomb safety factor could be expected with further refinement.

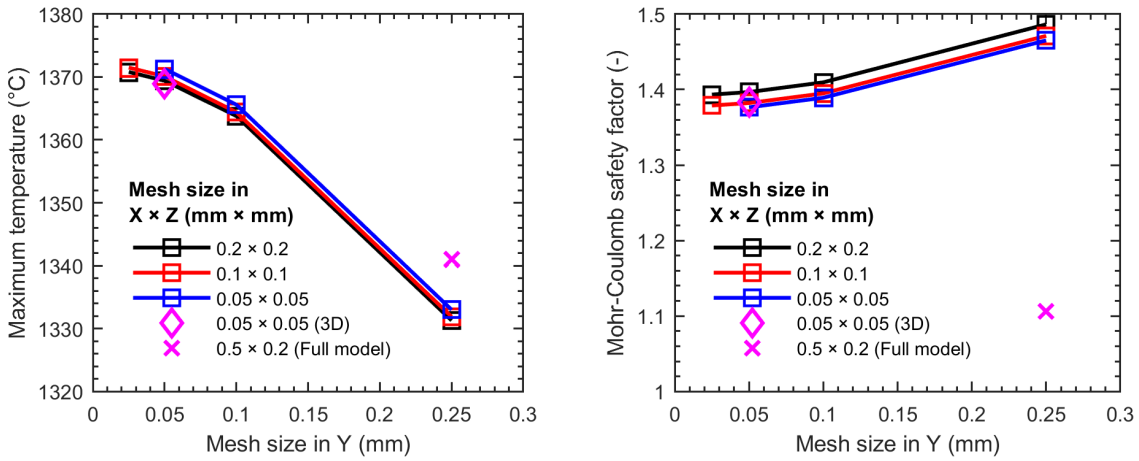

(a) (b)

Figure 42. Mesh sensitivity curves for (a) the maximum temperature and (b) the Mohr–Coulomb safety factor in graphite. The sensitivity study was performed with the graphite block model using 2D layered elements on the surface. Each curve represents refinement of the 3D elements below the surface shells in thickness (Y), while keeping the size on the surface plane (X and Z) fixed. For comparison, the results of the full model and the graphite block with 3D elements on the surface are included.

No mesh sensitivity study for the CuCrZr part was performed, as the temperatures and stresses in the critical areas of CuCrZr are well below the limits. The mesh size is already small and the mesh matches the FLUKA binning in the critical area. Additionally, the heat generation is more evenly distributed in the material bulk, compared to the highly local heat generation on the graphite surface.

6.3 Time Step Sensitivity

ANSYS documentation [27] suggest a conservative time step size in transient thermal simulations based on the Fourier modulus [45]. Using a too high time step in implicit simulations results in numerically too high thermal conduction. ANSYS issues a warning when the time step exceeds 100 times the time step expressed as [27]

$$\Delta t = \frac{\Delta x^2}{a} = \frac{\Delta x^2 \cdot c_p \cdot \rho}{\lambda} \tag{18}$$

where Δt is the time step length and Δx is element size. Assuming graphite with an element length of 5 µm (thickness of one layer of the shell element), and material properties as specified in Table 3, results in a step size of $\Delta t \approx 2 \times 10^{-7}$ s. The 150 µs time step is 750 times longer than the suggested time step. A sensitivity study was performed in a previous simulation iteration of the dump core with time steps of 50, 100, 150 and 200 µs, the shortest being 250 times the suggested maximum time step.

The maximum temperature over time and the resulting Mohr–Coulomb safety factor with the different time steps are plotted in Figure 43. The results with different time steps are in fairly good agreement. Solving the model with the suggested time step size would require approximately 30 000 time steps, which is unfeasible considering the number of elements in the model. Therefore, the used time step of 150 µs is considered

a reasonable compromise between accuracy and solving time.

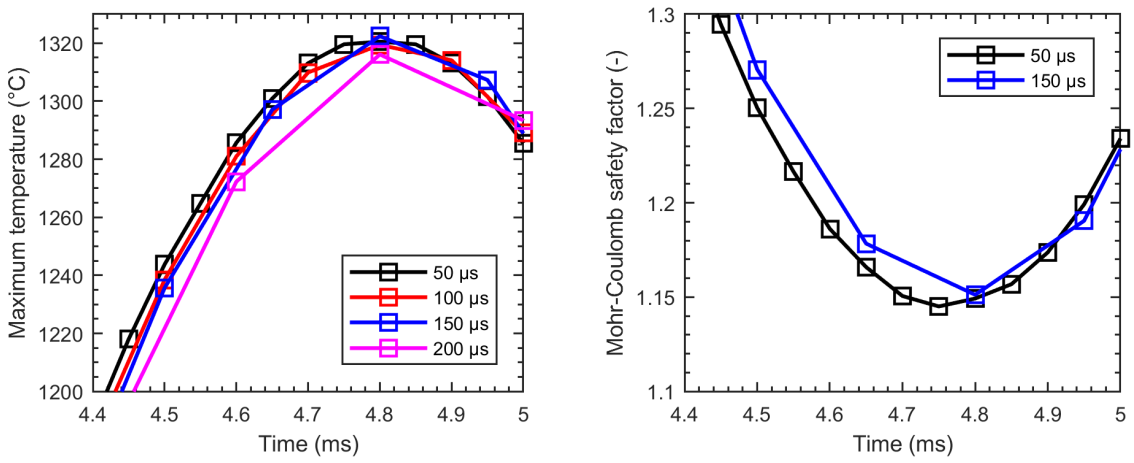

(a) (b)

Figure 43. Comparison of (a) the peak temperature and (b) the minimum Mohr–Coulomb safety factor during the dumping of a HL-LHC beam pulse with different time step lengths.

The maximum strain rate reached during the dumping of one pulse of HL–LHC is approximately $5\,\mathrm{s}^{-1}$. It it is the range of intermediate strain rates in Figure 22. Therefore, no elastic or plastic waves are expected, but inertia forces might play some role. For solving wave propagation effects, ANSYS documentation [27] suggests time steps small enough to capture the wave traveling through an element. The elastic waves propagate at the speed of sound in material as described in Section 3.3.3. Therefore, the time it takes for the wave to propagate through one element is

$$\Delta t = \frac{\Delta x}{c_0} = \Delta x \sqrt{\frac{\rho}{E}} \tag{19}$$

Considering graphite with the smallest mesh size of 0.2 mm and material properties from Table 3, results in a time step of $\Delta t \approx 8 \times 10^{-8}\,\mathrm{s}$, which is several orders of magnitude shorter than the the used time step of 150 µs. While the material behavior is assumed to be quasi-static, the time step is too large to capture any possible dynamic effects. Additionally, the through thickness stress is always zero in the shell elements, preventing any stress waves from being generated through the thickness. However, the simulations use a time integration scheme that is unconditionally stable regardless of time step size [27].

6.4 Dumping One Pulse of LHC 25ns HL–LHC Beam

The LHC 25ns HL–LHC beam is the baseline for the design. It has an intensity of 2.4×10^{13} ppp with a pulse period of 3.6 s and a maximum momentum of 26 GeV/c. The thermo-mechanical response of the core during the dumping of a single beam pulse is studied. The FLUKA heat generation input consists of 40 time steps for a total dumping time of 6 ms, after which the core cools down until the pulse period.

The maximum temperature over time in graphite and CuCrZr during the pulse period is plotted in Figure 44a. The maximum temperatures during the multi-turn beam

shaving, lasting 6 ms, are plotted in Figure 44b. The maximum temperature is observed to increase fast during the first milliseconds of dumping, reaching a peak temperature of 1341 °C in graphite at 4.65 ms and 83.6 °C in CuCrZr at 4.95 ms. The temperature distribution in the core at the time of maximum at 4.65 ms is shown in Figure 45. The temperature distribution at this time on the shaving surface along the symmetry plane is plotted in Figure 46.

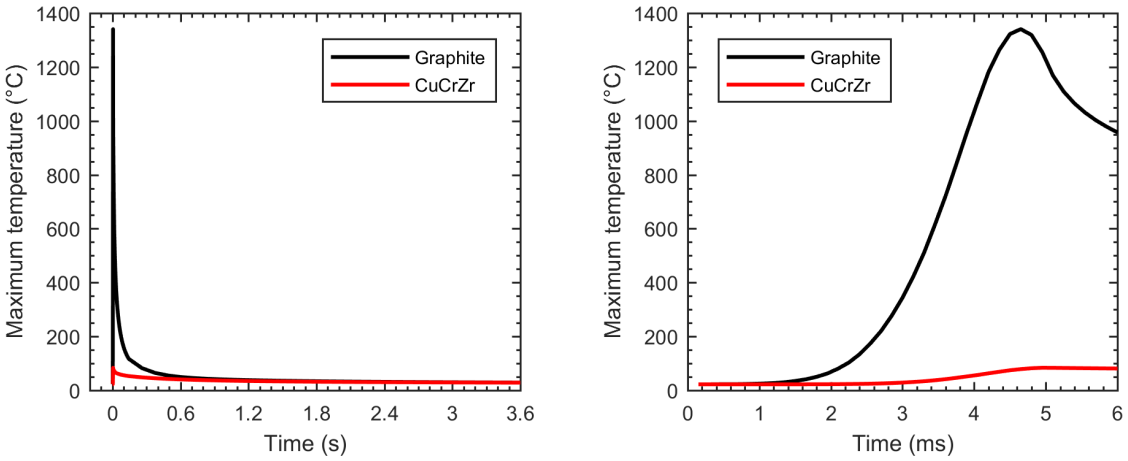

(a) (b)

Figure 44. Maximum temperatures over time in graphite and CuCrZr during the dumping of a single pulse of HL–LHC. The maximum temperatures are plotted (a) during the pulse period and (b) during the multi-turn beam shaving lasting 6 ms.

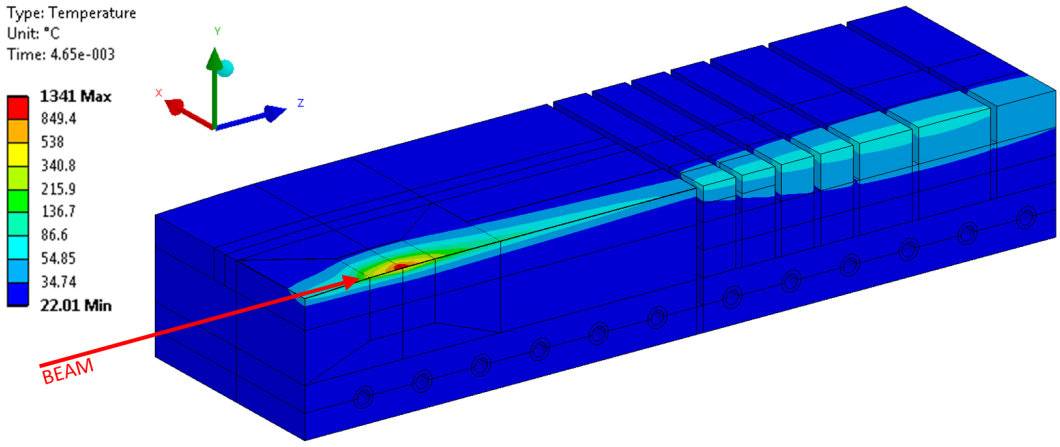

Figure 45. Temperature distribution during the dumping of one pulse of HL–LHC at the time of the peak temperature at 4.65 ms. Note: logarithmic scale.

The peak temperature in graphite occurs at 30 mm in length in a joint between two planes used to approximate the rounded edge in FLUKA and ANSYS, as illustrated in 35. As the planes have a corner at the location of the maximum, the temperature peak seen in Figure 46 is artificially too sharp. The peak temperature in CuCrZr occurs on the surface of the first slice downstream of the graphite.

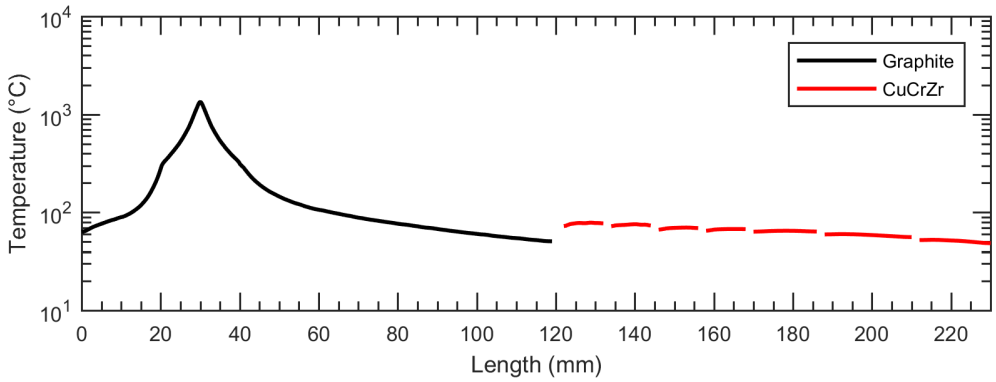

Figure 46. Temperature path on the shaving surface along the symmetry plane during the dumping of one pulse of HL–LHC at the time of the peak temperature at 4.65 ms. Note: logarithmic scale.

The equivalent von Mises stress distribution in graphite induced by the temperature increase is plotted at the time of the peak temperature at 4.65 ms in Figure 47. The maximum stress coincides with the peak temperature. The normal stress components in time at the most critical node of graphite are plotted in Figure 48a. A stress path in thickness below the critical node is plotted in Figure 48b.

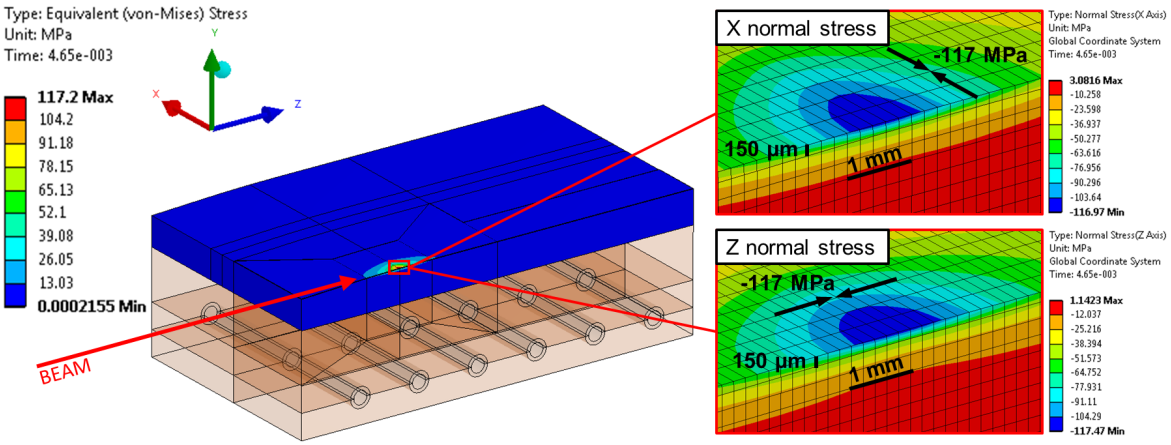

Figure 47. Stress distribution in graphite during the dumping of one pulse of HL–LHC at the time of the maximum at 4.65 ms.

The stress state on the graphite surface plane (XZ) is biaxial compression. The normal stress perpendicular to the surface is zero, as it is a free surface and the surface shell elements do not model through-thickness stresses. The shear stresses are negligible. The minimum principal stress is −118 MPa, resulting in a Mohr–Coulomb safety factor of 1.10, as calculated with Equation (15).

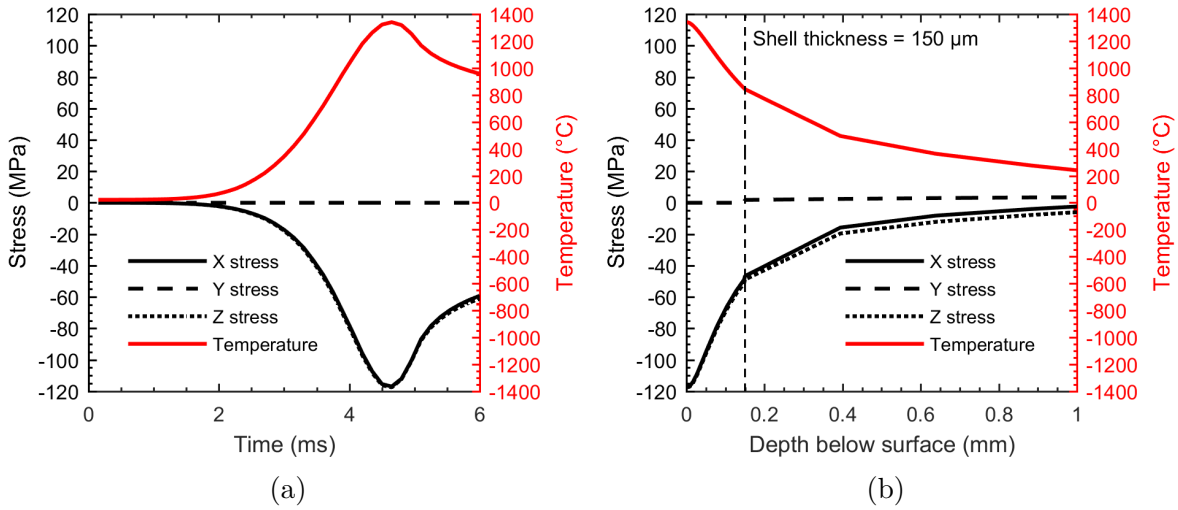

Figure 48. Temperature and stress results for graphite during the dumping of one pulse of HL–LHC. (a) Temperature and stress results over time at the most critical node in graphite. (b) Stress and temperature distribution below the most critical graphite node at the time of the maximum stress at 4.65 ms.

The von Mises stress distribution in CuCrZr at the time of the maximum stress at 4.95 ms is plotted in Figure 49. A representative maximum stress of 58.6 MPa is taken from first slice of CuCrZr. The safety factor calculated with Equation (14) is 4.69, considering the yield strength at 100 °C. Higher stress peaks are observed on the bottom of the gaps, but they are not studied in detail as the mesh in that location is too coarse and the geometry does not include any fillets.

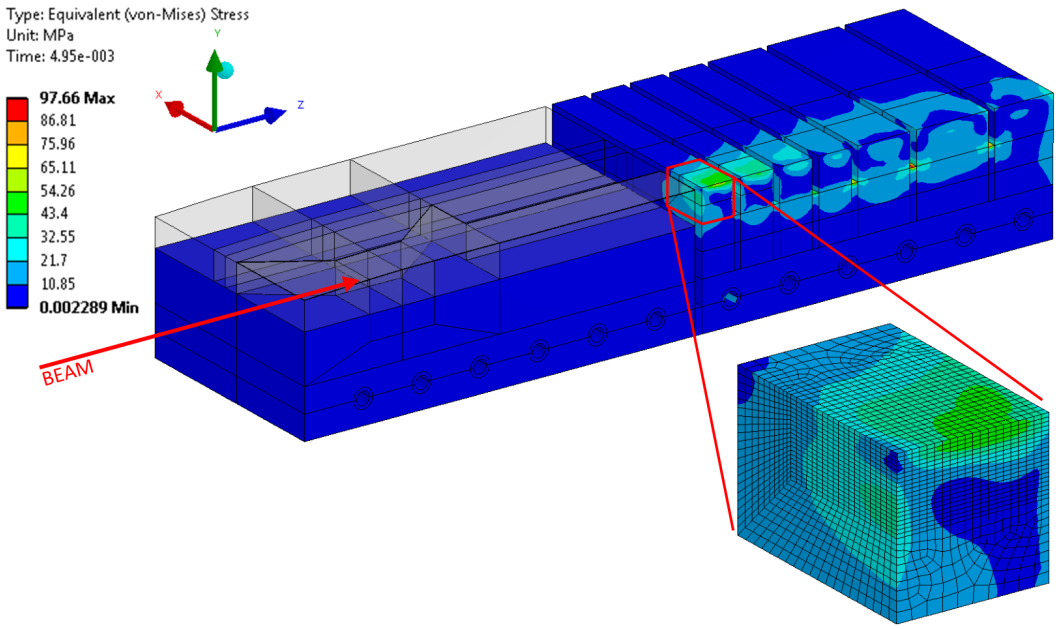

Figure 49. Von Mises stress distribution in CuCrZr during the dumping of one pulse of HL–LHC at the time of the maximum at 4.95 ms.

The simulation results are collected in Table 8.

Table 8. Results of the simulation of one pulse of HL–LHC.

LHC 25ns HL–LHC	2.4×10^{13} ppp, 26 GeV/c, 1.74 mm × 0.87 mm ($\sigma_h \times \sigma_v$)		
		Graphite	CuCrZr
Global results			
Temperature limit	[°C]	2000	300
Maximum temperature	[°C]	1341	83.7
Maximum representative von Mises stress	[MPa]	–	58.6
Critical graphite node			
X normal stress	[MPa]	−117	
Y normal stress	[MPa]	0	
Z normal stress	[MPa]	−117	
Maximum principal stress	[MPa]	0	
Minimum principal stress	[MPa]	−118	
Safety factors			
Material strength	[MPa]	$\sigma_T = 40/\sigma_C = 130$	$\sigma_y = 275$ (at 100 °C)
Safety factor	[-]	$SF_{M\text{-}C} = 1.10$	$SF_{vM} = 4.69$

6.5 Steady-State and Cooling Performance

The performance of the cooling system is studied with thermal simulations reaching a steady-state where the input and output power are equal and the maximum temperature over time stays constant. In the steady-state simulations the energy deposited by a beam pulse is averaged over the pulse period and applied in large time steps. This approach requires much less computation time than simulating pulses individually, thus allowing the simulation of longer times. The averaged power is obtained by superposing the FLUKA energy deposition map of each time step and dividing the summed energy by the pulse period.

An average power corresponding to dumping a HL–LHC beam continuously every 3.6 seconds is used. The beam has an intensity of 2.4×10^{13} ppp or 0.667×10^{13} protons/s. The total deposited energy per pulse is 8089.4 J (see Table 7), leading to a heating power of 2240 W. The dumping rate of 0.667×10^{13} protons/s is considered a reasonable upper limit. It corresponds to a supercycle lasting 25.2 s with three machine development beam dumps triggered manually (at 5×10^{13} ppp each) and three East area beam dumps triggered by an interlock (at 0.45×10^{13} ppp each). The resulting intensity rate of this supercycle is 0.65×10^{13} protons/s.

The maximum averaged temperatures over time in graphite, CuCrZr and the cooling pipe walls are plotted in Figure 50. The maximums reached at steady-state are 112 °C in CuCrZr, 109 °C in graphite and 91 °C in the cooling pipe wall. The steady-state is reached in less than 15 minutes of continuous dumping operation. The temperature distribution in the core after 900 s is shown in Figure 51. The cooling pipe wall temperature stays below the boiling point of water at atmospheric pressure or higher [45] and the maximum heat flux from the pipe wall to water is 160 kW/m^2. The boundary conditions were specified considering the steady-state as described in Section 5.5, and as such the results are unrealistic before the steady-state is reached.

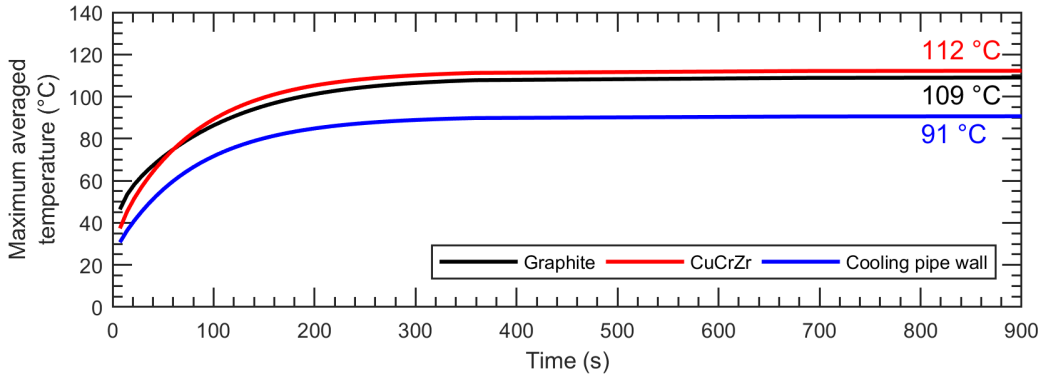

Figure 50. Maximum averaged temperatures over time.

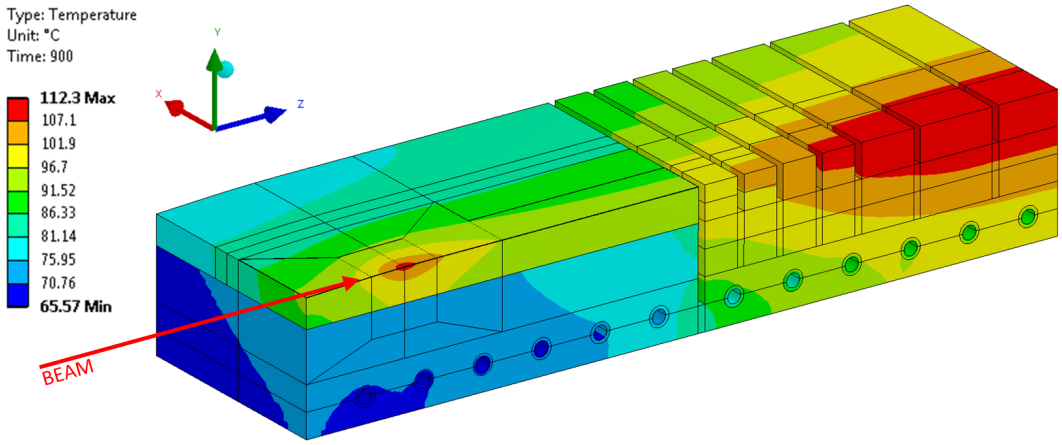

Figure 51. Steady-state averaged temperature distribution.

The sensitivity to the heat transfer coefficients was studied by changing the coefficients individually and comparing the maximum averaged steady-state temperature reached. The results for graphite are plotted in Figure 52a and for CuCrZr in Figure 52b. The temperatures are found to be more sensitive to the cooling pipe to water contact than the graphite to CuCrZr contact.

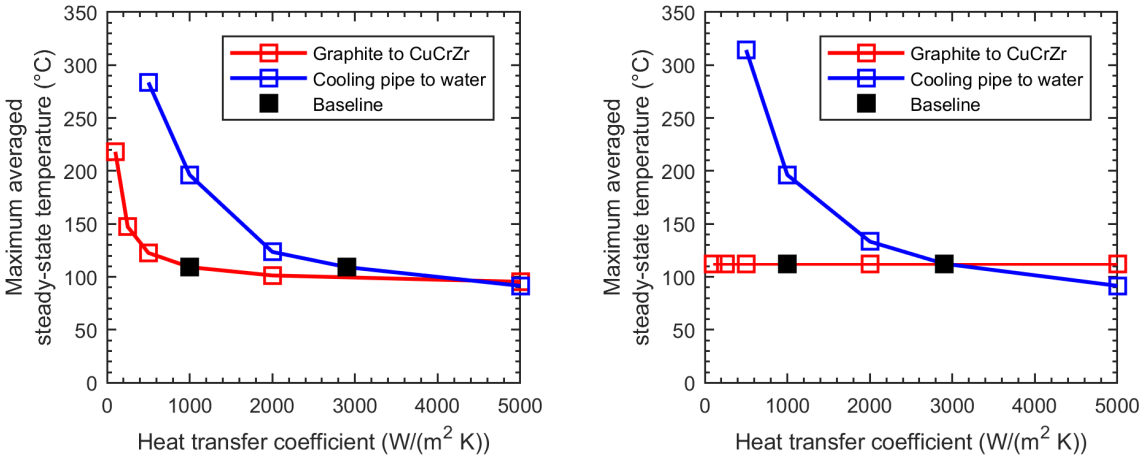

(a) Graphite. (b) CuCrZr.

Figure 52. Sensitivity of the maximum averaged steady-state temperature in (a) graphite and (b) CuCrZr to the heat transfer coefficients of the interfaces. A curve represents changing the heat transfer coefficient of the corresponding interface while keeping the other one constant.

6.6 Dumping Four Pulses of LHC 25ns HL–LHC Beam After Steady-State

The functional specification [11] states that the dump core should withstand minimum four consecutive dumps of the HL–LHC beam. The temperatures in continuous dumping operation is studied by simulating four pulses of HL–LHC after reaching the steady-state (at 3600 s). The last pulse is then studied also in a structural simulation. In steady-state simulations the heat generation is averaged over the pulse period, which differs from simulating the pulses individually. It takes time to transition between the two approaches, and therefore the results of the fourth pulse are the most realistic.

The maximum temperatures during the four pulse periods are plotted in Figure 53a and during the dumping of the last pulse in 53b. A peak temperature of 1381 °C is reached in graphite 4.65 ms after the start of the dumping of the last pulse. The temperature distribution at this time is shown in Figure 54. The maximum temperature reached in CuCrZr is 157 °C.

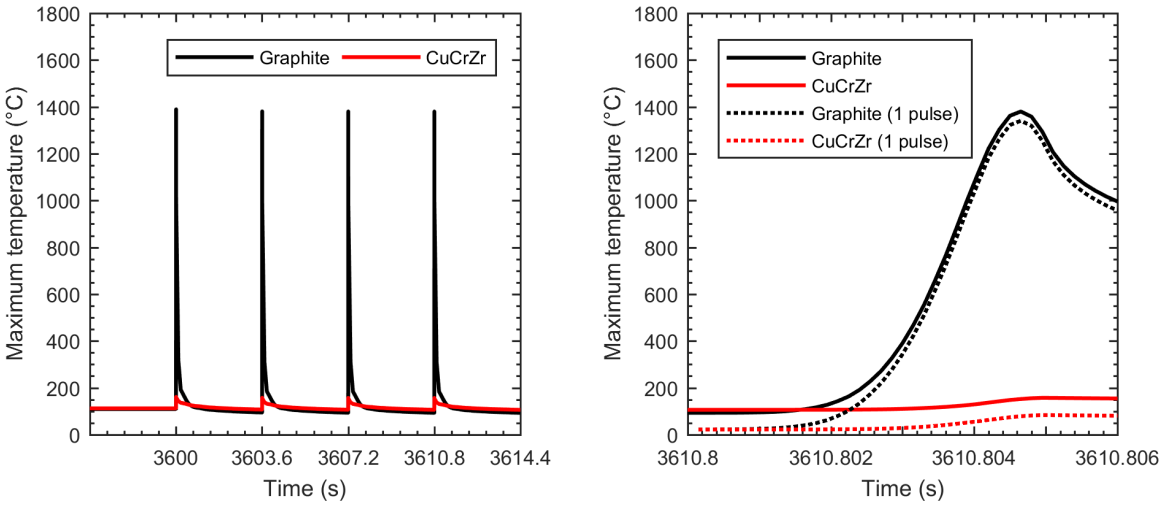

Figure 53. Maximum temperatures over time in graphite and CuCrZr during the dumping of four pulses of HL–LHC after steady-state. The maximum temperatures are plotted (a) during the four pulse periods and (b) during the dumping of the last pulse, lasting 6 ms.

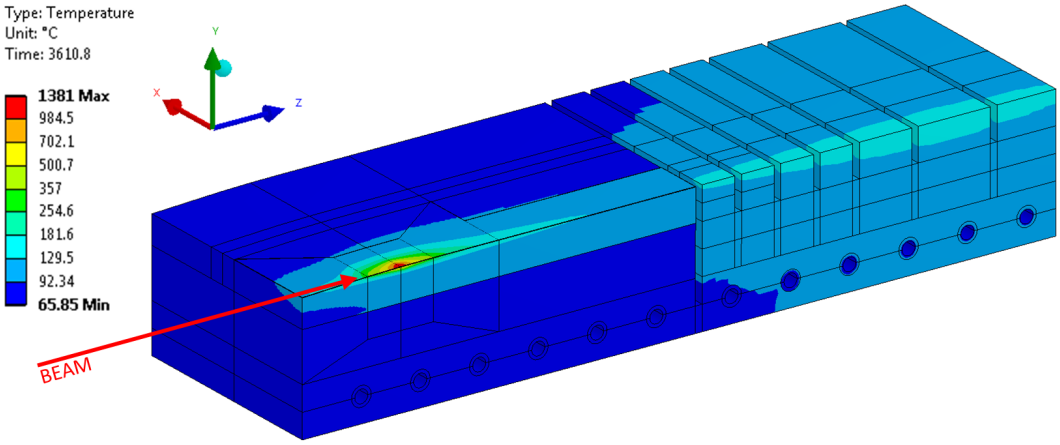

Figure 54. Temperature distribution during the dumping of the fourth pulse of HL–LHC after steady-state at the time of the peak temperature at 4.65 ms after the start of the dumping. Note: logarithmic scale.

The temperature increase causes the dump core to deform as shown in Figure 55. The deformations are low in magnitude but might lead to several issues: The CuCrZr has a higher CTE than graphite and therefore it expands more. For example the top surface of CuCrZr expands upwards around 20 µm more than graphite. This might cause a change in how the protons interact with the core geometry. Additionally, the CTE mismatch may cause issues in the graphite to CuCrZr interface. Since the interface and the supports are not modeled in detail, the deformations are not analyzed further.

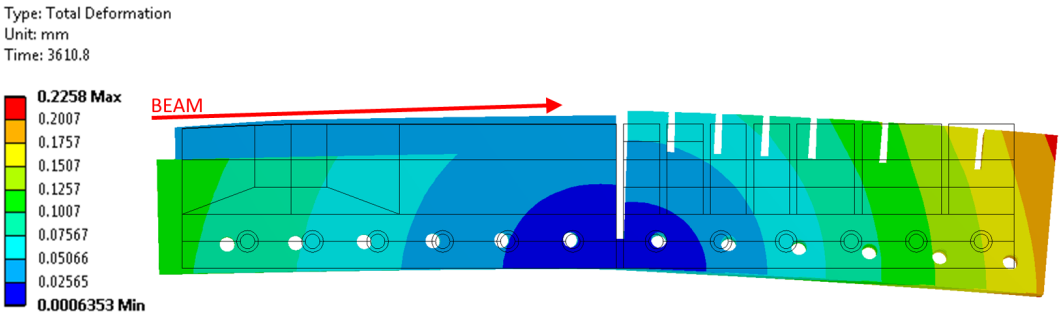

Figure 55. Deformations in the dump core during the dumping of the fourth pulse of HL–LHC after steady-state, at the time of the peak temperature at 4.65 ms after the start of the dumping. Note: the shape change is exaggerated.

The equivalent von Mises stress distribution in the core at the time of the peak temperature is plotted in Figure 56. The stress state in graphite is biaxial compression on the surface plane, similarly to the dumping of one pulse of HL–LHC as described in Section 6.4. The minimum principal stress is −133 MPa, resulting in a Mohr–Coulomb safety factor of 0.977, as calculated with Equation (15). The maximum representative stress in CuCrZr is 52.7 MPa. The resulting von Mises safety factor calculated with Equation (14) is 3.33, considering yield strength at 200 °C.

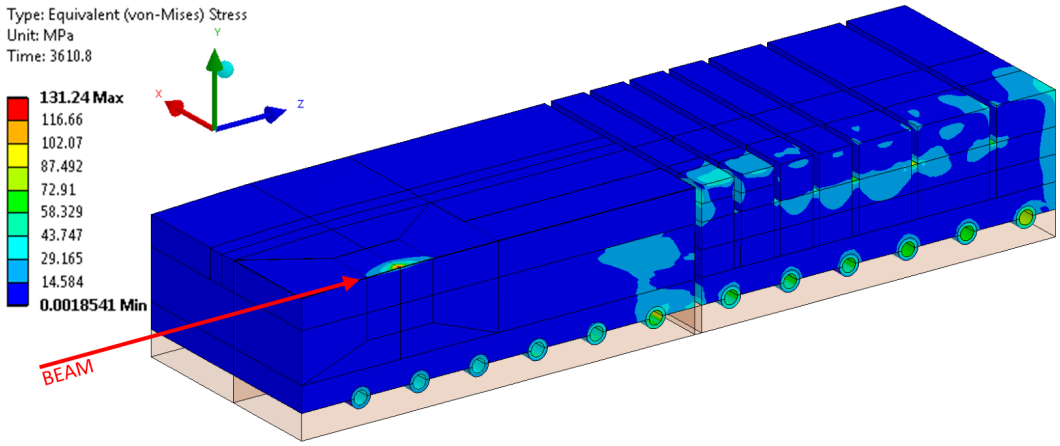

Figure 56. Stress distribution in the core during the dumping of the fourth pulse of HL–LHC after steady-state, at the time of the maximum at 4.65 ms after the start of the dumping.

The simulation results are collected in Table 9.

Table 9. Results of the simulation of the fourth pulse of HL–LHC after steady-state.

LHC 25ns HL–LHC	2.4×10^{13} ppp, 26 GeV/c, 1.74 mm × 0.87 mm ($\sigma_h \times \sigma_v$)		
		Graphite	CuCrZr
Global results			
Temperature limit	[°C]	2000	300
Maximum temperature	[°C]	1390	157
Maximum representative von Mises stress	[MPa]	–	52.7
Critical graphite node			
X normal stress	[MPa]	−130	
Y normal stress	[MPa]	0	
Z normal stress	[MPa]	−133	
Maximum principal stress	[MPa]	0	
Minimum principal stress	[MPa]	−133	
Safety factors			
Material strength	[MPa]	$\sigma_T = 40/\sigma_C = 130$	$\sigma_y = 259$ (at 200 °C)
Safety factor	[-]	$SF_{M\text{-}C} = 0.977$	$SF_{vM} = 4.91$

6.7 Dumping Other Beams

The Highest Intensity beam scenario is an accidental scenario that is not foreseen to be dumped regularly. It has an intensity of 5×10^{13} ppp, which is over two times the intensity of the HL–LHC beam. While the size of the beam is also larger, the higher intensity poses a threat to the dump core integrity. The dumping of a single pulse from ambient temperature is simulated. The FLUKA heat generation input consists of 55 time steps, for a total dumping time of 8.25 ms.

The maximum temperatures over time in graphite and CuCrZr are plotted in Figure 57a. The stresses and temperatures at the critical node on the graphite surface are plotted in Figure 57b. The temperature distribution at the time of the peak temperature at 7.2 ms is shown in Figure 58. The von Mises stress distribution at the same time is shown in Figure 59.

The results of interest for the Highest Intensity beam are presented in Table 10. The temperature distribution is wider and the maximum temperatures are higher than for the HL–LHC, due to the bigger size and higher intensity. The resulting stresses are also higher, resulting in a safety factor of 0.81 in graphite and 3.33 in CuCrZr.

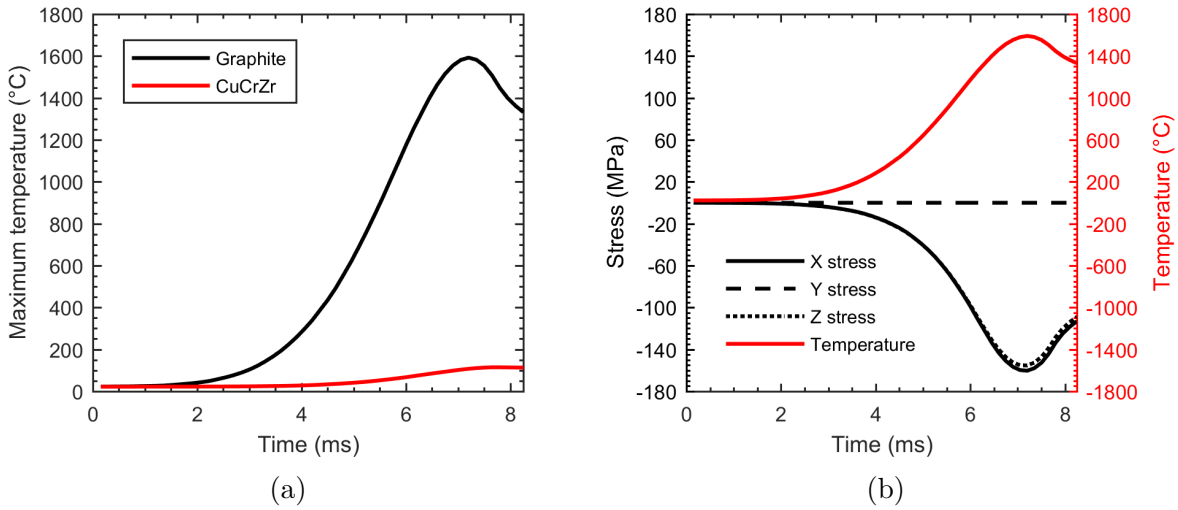

Figure 57. (a) Maximum temperatures in the core over time and (b) temperature and stresses at the critical node of graphite during the dumping of one pulse of the Highest Intensity beam.

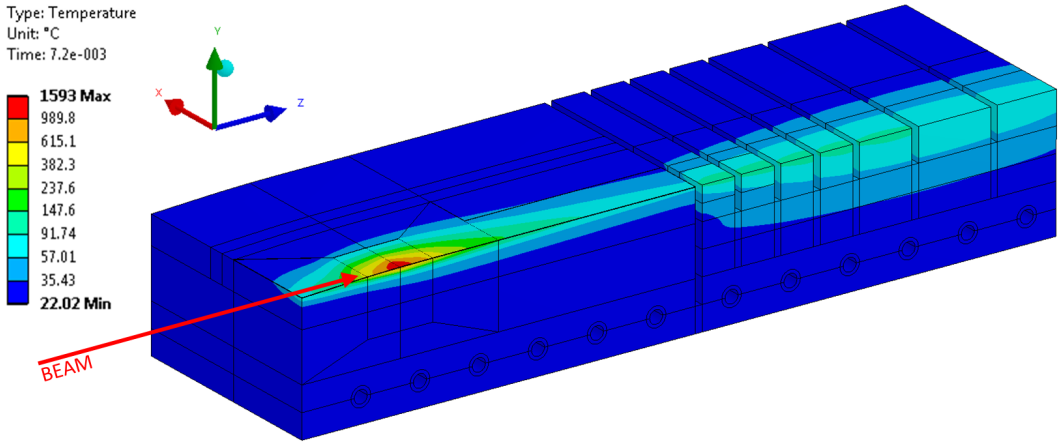

Figure 58. Temperature distribution during the dumping of one pulse of the Highest Intensity beam at the time of the peak at 7.2 ms. Note: logarithmic scale.

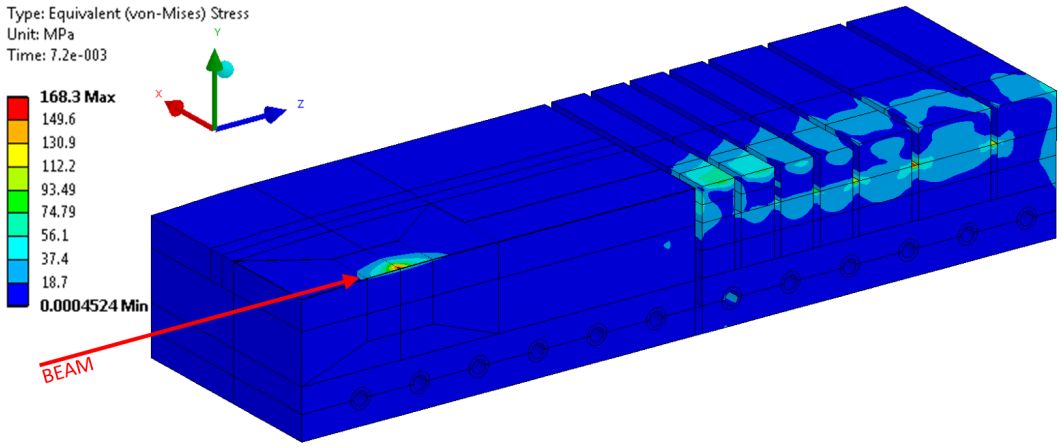

Figure 59. Von Mises stress distribution in the core during the dumping of one pulse of the Highest Intensity beam at the time of the peak at 7.2 ms.

Table 10. Results of the simulation of one pulse of Highest Intensity beam.

Highest Intensity	5×10^{13} ppp, 26 GeV/c, 3.10 mm × 1.45 mm ($\sigma_h \times \sigma_v$)		
		Graphite	CuCrZr
Global results			
Temperature limit	[°C]	2000	300
Maximum temperature	[°C]	1593	144
Maximum representative von Mises stress	[MPa]	–	77.6
Critical graphite node			
X normal stress	[MPa]	−160	
Y normal stress	[MPa]	0	
Z normal stress	[MPa]	−155	
Maximum principal stress	[MPa]	0	
Minimum principal stress	[MPa]	−160	
Safety factors			
Material strength	[MPa]	$\sigma_T = 40/\sigma_C = 130$	$\sigma_y = 259$ (at 200 °C)
Safety factor	[-]	$SF_{M\text{-}C} = 0.81$	$SF_{vM} = 3.33$

The other considered beam scenarios presented in Section 4.3, HL–BCMS and SFTPRO, were simulated in a previous design iteration with a model closely resembling the one presented in this thesis. The maximum temperatures in graphite during the dumping of all the considered beam scenarios are plotted in Figure 60. The maximum temperatures reached are significantly lower in case of HL–BCMS and SFTPRO compared to the other beams. The temperatures in CuCrZr were similarly lower. The resulting stresses were also significantly lower and as such these beam scenarios are not expected to be critical for the dump core integrity.

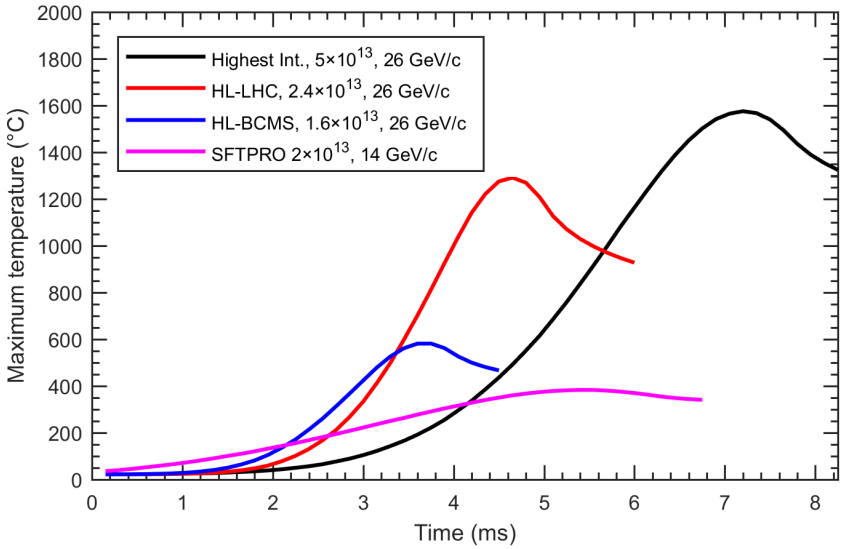

Figure 60. Maximum temperature in graphite over time for all the considered beam scenarios. The simulations were performed in a previous design iteration with a model closely resembling the one presented in this thesis.

6.8 Effect of Slicing the Graphite

The graphite surface is proposed to be sliced bidirectionally to allow for thermal expansion and therefore alleviate the stresses. The effect of slicing is studied with a smaller scale model of a single graphite block as presented in Figure 61. The slicing is not included in the FLUKA geometry, and the same input files are used as in the full model. The heat generation peak seen Figure 41 is located in the middle of the block surface, which was found to be the most critical location as there is more material around constricting the thermal expansion. 3D elements are used on the shaving surface, as opposed to the layered 2D shell elements used in the full model, since the block geometry is small enough to be meshed with reasonable number of elements with reasonable aspect ratio.

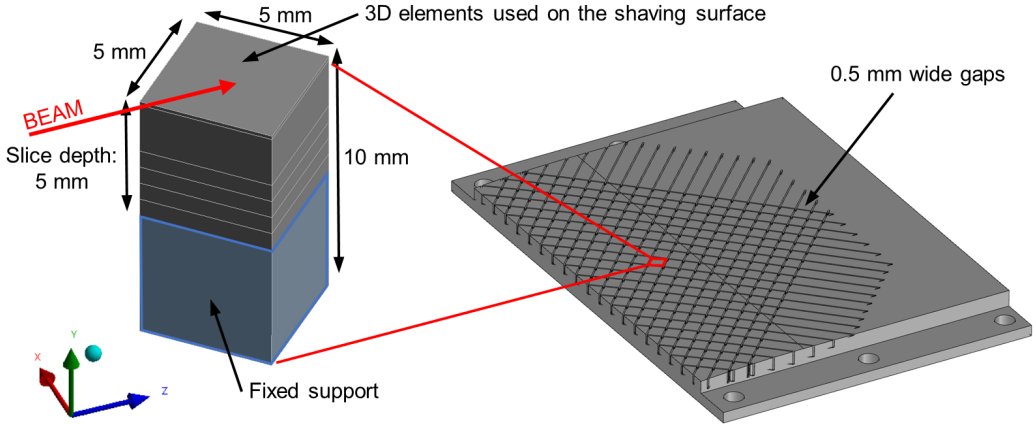

Figure 61. Geometry of the sliced graphite block model.

The temperature results for the dumping of one pulse of HL–LHC are presented in Figure 62. A maximum temperature of 1369 °C is reached, compared to 1341 °C without slicing.

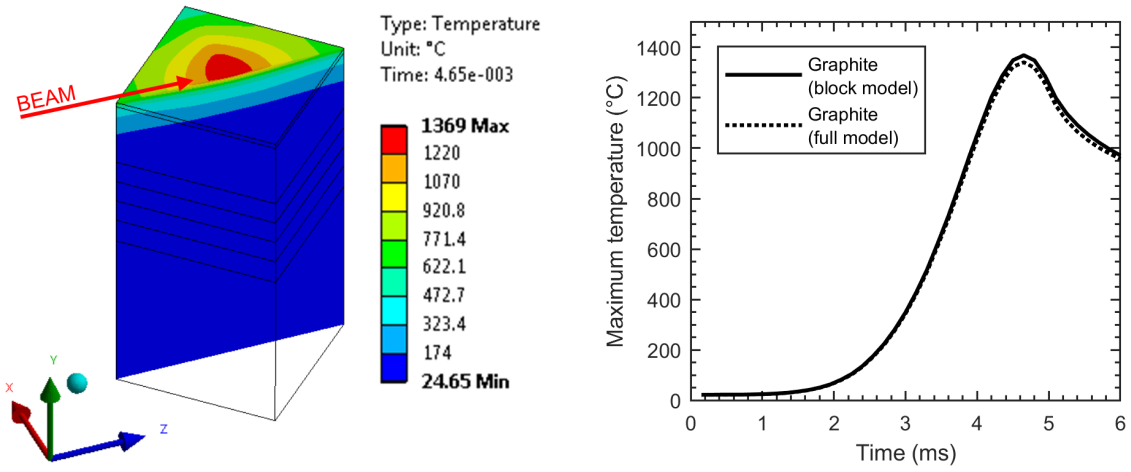

(a) (b)

Figure 62. Temperature results of a sliced graphite block model for the dumping of one pulse of HL–LHC. (a) Temperature distribution in a block section at time of the peak temperature at 4.65 ms. (b) The maximum temperature over time, compared with the full model.

The temperature and stress state in the block were studied with stress path results in the three main directions, as presented in Figure 63. The stress state is biaxial compression on the surface plane, similarly to the full model as presented in Section 6.4. The temperature and stress distribution is sharper in Z, supposedly due to the joint between the straight planes used to approximate the rounded shape. The high temperatures and stresses are located very superficially on the surface of the block, as seen from Figure 63c.

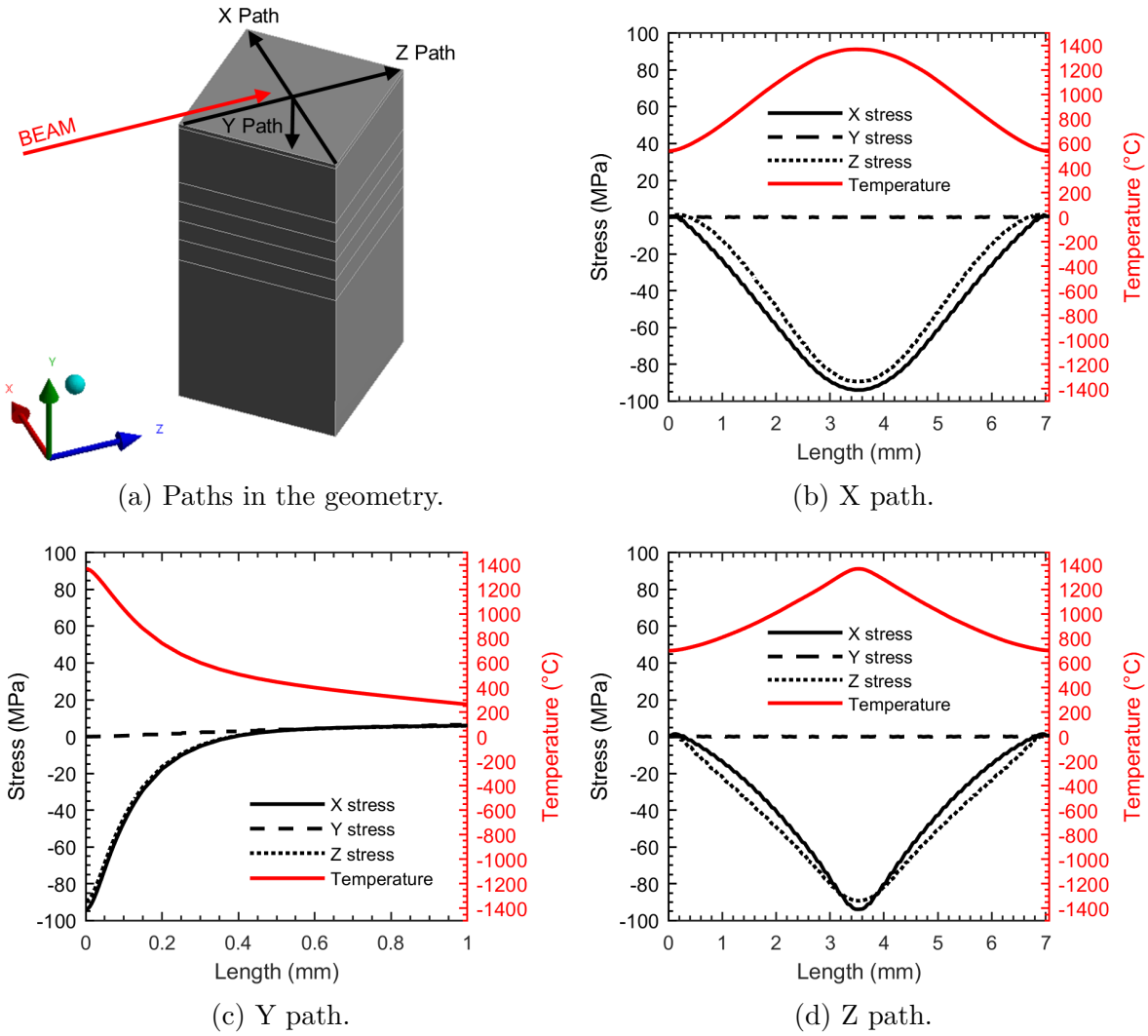

(a) Paths in the geometry.

(b) X path.

(c) Y path.

(d) Z path.

Figure 63. Temperature and stress path results in the graphite block model at 4.65 ms during the dumping of one pulse of HL–LHC beam.

The results of interest for the graphite block model are presented in Table 11 for the dumping of one pulse of HL–LHC and Highest Intensity beams. The results are compared against the results from the full model. A slight increase in the maximum temperature is observed, while the minimum principal stress is significantly reduced. The safety factors are moderately increased, and a safety factor above one is achieved for the Highest Intensity beam scenario.

Table 11. Simulation results in graphite with slicing (graphite block model) and without slicing (full model) for the dumping of one pulse of HL–LHC and Highest Intensity beams.

		HL–LHC		Highest Intensity	
		Without slicing	With slicing	Without slicing	With slicing
Maximum temperature	[°C]	1341	1369 (+2.1%)	1593	1633 (+2.5%)
Maximum principal stress	[MPa]	3.96	8.61 (+117%)	5.13	14.65 (+186%)
Minimum principal stress	[MPa]	−118	−93.9 (−20%)	−160	−110 (−31%)
Safety factor $SF_{M\text{-}C}$	[-]	1.10	1.38 (+25%)	0.81	1.18 (+46%)

7 Discussion

7.1 New Dump Core Design

A preliminary design of the new Proton Synchrotron Internal Dump core was presented, consisting of graphite SGL SIGRAFINE® R7550 and a precipitation hardened copper alloy CuCrZr. The core weighs 13 kg and has the dimensions of 180 mm × 40 mm × 230 mm (width × height × length). The dump core is moved into the beam path by an electromagnet and spring-based actuation mechanism. The circulating proton beam is shaved by the core surface during thousands of beam revolutions. The particle shower generated by the dumping deposits energy in the materials, leading to a temperature increase and mechanical stresses. Both the graphite and the CuCrZr are sliced to allow thermal expansion to alleviate the stresses.

The design objective of the dump core is to ensure the mechanical integrity of the materials in beam impact: The maximum temperatures should stay within the allowable temperatures and the stresses should stay within the elastic regime. Additionally, the core should not suffer fatigue failure or critical radiation damage.

The dump core behavior in beam impact was studied with transient thermal and structural finite element simulations using ANSYS Workbench 17.1 software coupled with FLUKA heat generation input. Temperature dependent isotropic elastic material models were implemented for all the materials, although graphite exhibits nonlinear elastic–plastic behavior. The highly localized energy deposition generated by the beam shaving presented several simulation challenges. Layered two-dimensional shell elements were used on the shaving surface to import the heat generation from FLUKA simulations. The initial proton impact location in graphite required a small mesh size for convergence, which in turn lead to the need for small time steps. While no significant dynamic effects in the material are expected, the time steps used were too large to capture any possible dynamic effects.

7.2 Thermal Analysis Results

The thermal contacts and boundary conditions in the model were based on analytical calculations and are considered estimates. They will be refined and adjusted based on tests performed during prototyping and commissioning. The graphite and CuCrZr were clamped together on the sides of the core, with an assumed uniform contact pressure and heat transfer coefficient throughout the surface. The cooling pipes are planned to be diffusion bonded with the CuCrZr by hot isostatic pressing, resulting in a perfect thermal contact.

Averaged maximum steady-state temperatures of 112 °C in CuCrZr and 109 °C in graphite were reached. A power deposition corresponding to the dumping of a HL–LHC beam pulse every 3.6 s was used. This is considered as a pessimistic upper limit. The dumping of four pulses of HL–LHC after steady-state was simulated and maximum temperatures of 1390 °C in graphite and 157 °C in CuCrZr were reached. The highest temperatures were reached during the dumping of a single pulse of the Highest Intensity beam, reaching 1593 °C in graphite and 144 °C in CuCrZr. The maximum temperatures in all the simulation cases stay below the considered limits of 2000 °C for graphite and

300 °C for CuCrZr. The dumping of an accidental beam pulse after steady-state was not simulated, which might result in a higher peak temperature. The temperatures reached in the other beam scenarios, LHC 25ns HL–BCMS and SFTPRO, were significantly lower and therefore not expected to be critical for the core design.

7.3 Structural Analysis Results

The von Mises safety factors in CuCrZr were 4.69 for the dumping of one pulse of HL–LHC, 4.91 for the dumping of the fourth pulse of HL–LHC after steady-state, and 3.33 for the dumping of one pulse of the Highest Intensity beam. The safety factors are large and do not indicate a failure of the CuCrZr. Some stress concentrations were observed at the bottom of the gaps, risking crack formation or fatigue, but the finite element model was not detailed enough in this region for further study.

The Mohr–Coulomb safety factors in graphite were calculated with a full model geometry, which did not include the slicing in graphite. The resulting safety factors were 1.10 for the dumping of one pulse of HL–LHC, 0.977 for the dumping of the fourth pulse of HL–LHC after steady-state, and 0.81 for the dumping of the Highest Intensity beam. The safety factors are low and even below one, indicating failure of the graphite.

The safety factors can be improved moderately by slicing the graphite. The effect of the slicing was studied by simulating a single block of graphite in the most critical location. The simulations yielded safety factors of 1.38 for the dumping of one pulse of HL–LHC and 1.18 for the dumping of one pulse of the Highest Intensity beam. The safety factors are improved by the slicing, but still remain low. Additionally, the slicing might introduce new problems, such as fracture of the brittle graphite at the bottom of the gaps.

The stress state in graphite is biaxial compression on the surface plane in an area of a few square millimeters that is limited to less than a millimeter in thickness. The peak stresses occur at the location of the peak power deposition, which is artificially sharp due to approximation of the shaving edge with straight planes in FLUKA. Additionally, the Christensen failure criterion suggests that the compressive strength of a material is higher in multiaxial than uniaxial compression, which is supported by measurements performed for NBG18 graphite. In addition, the material model used for graphite is linear elastic and a conservative dynamic Young's modulus was used. Finally, the strength of graphite increases with temperature, while the strength for the calculations of safety factors was considered at room temperature, even though the peak stress coincides with the peak temperature. Considering these points brings additional safety not considered in the calculated safety factors.

7.4 Fatigue

The exact number of beams to be dumped and their types are not well known or defined. As such no specific requirements for the fatigue lifetime of the core has been set. A few hundred or thousand high intensity beams can be expected to be dumped per year. The stresses in CuCrZr are far below the yield stress and therefore fatigue is not expected to be a problem based on fatigue life curves found in literature. No fatigue data was found for the specific graphite type used, but fatigue in graphite may be a limiting factor in the core lifetime, as the stresses are close to the material strength.

The fatigue studies presented in this thesis are not comprehensive, but rather a first look into the subject. Fatigue is a complicated subject due to the complex stress state and fatigue behavior that is affected by both the temperature and the irradiation of the materials.

7.5 Radiation Damage

Radiation damage has not been considered in the material model of the simulations. To evaluate the material damage caused by irradiation, an estimated yearly DPA value of 0.03 for graphite and 0.002 for CuCrZr was calculated with FLUKA. After 20 years of operation the accumulated DPA values are 0.6 DPA in graphite and 0.04 in CuCrZr. The peak values are localized on the surface and calculated assuming a beam impact always in the same location. The damage is also accumulated towards the end of the lifetime. The DPA levels are fairly low, but in CuCrZr some hardening, embrittlement and a slight decrease in thermal conductivity may occur. No significant swelling is expected. Quantifying the damage in graphite is more difficult since no comparable data in literature was found. While the DPA value is low, radiation damage in graphite may pose a problem as the safety factors in graphite are already low.

8 Conclusions and Future Work

The preliminary dump core design was presented including its function, geometry, materials and cooling system. The mechanical integrity of the dump core under beam impact induced thermal shock was studied. A finite element model was produced and aspects relating to the FLUKA heat generation import, mesh sensitivity, boundary conditions, contacts, and time stepping were studied. The simulation results show that the materials stay below their maximum allowable temperature. The stresses stay within the elastic regime, providing that the graphite is sliced. A first look into fatigue and radiation damage of the core was presented. In conclusion, the core was studied from the perspective of the objectives set in the functional specifications document, and while some open questions remain, the design objectives were overall fulfilled and no critical problems preventing further work towards prototyping were discovered.

The dump core design presented in this thesis is preliminary and further work is needed before achieving prototyping, manufacturing and eventually installation readiness. A review panel was held on 4th October 2017, aimed at verifying the design of the dump, including the core. The review panel raised several points related to the dump core design. Some of the main points are as follows.

Attention should be devoted to the study of the graphite to CuCrZr interface and its reliability over time, especially to the simulations and optimization of the contact pressure along the interface. The stress distribution due to the acceleration of the core and the relaxation of residual stresses over time should be considered. Different clamping solutions or other bonding methods should also be considered. Alternatively the intermediate CuCrZr could be removed and the graphite could be joined directly to the cooling pipes.

The possibility of surface texturing or different shaving surface geometries was suggested as an alternative to the slicing of the graphite. Different surface textures and geometries were considered during the design, but simulating such small scale features in ANSYS ,coupled with FLUKA inputs, poses significant technical challenges. So while the concept is promising, verifying it through simulations is difficult.

The panel considered the DPA values in both graphite and CuCrZr low, but nevertheless recommended the consideration of degradation of the thermal and physical properties in the simulations. Correlating the simulated DPA values with qualitative change in material properties from literature is challenging due to the lack of data and different irradiation conditions. An approach could be taken to reduce the material properties, such as the thermal conductivity, by an estimated set amount. For now the radiation damage has been studied separately from the simulations.

A direct impact on the dump core should be studied at beam injection when the core is in the beam path. Special attention should be paid to the interface between graphite and CuCrZr. A direct impact at injection is considered a rare and intended use of the dump. While the beam momentum at injection is low, the scenario nevertheless poses risks for the core integrity and is planned to be studied in the future.

In addition to the comments raised by the review panel, several other aspects of the dump core design remain open. Studying the manufacturability of the design is ongoing and some changes are foreseen. The diffusion bonding of the stainless steel cooling pipes to CuCrZr is especially critical and some changes are foreseen in the design of the cooling circuits.

One objective of the core design was to minimize the escaping beam energy from the dump core. The core design presented absorbs only approximately 10% of the beam energy during dumping. Increasing the percentage of energy absorbed in the core is difficult due to the beam shaving operation, as well as the space and mass restrictions. While the current dumps are estimated to absorb a similar fraction of the energy, the beam energies will be higher after the LHC Injectors Upgrade project, risking damage to the downstream accelerator equipment or a high radioactivation the surroundings. Studies on the effects of the dumping on the dump mechanism, the radiation shielding, and the downstream equipment are ongoing.

The Proton Synchrotron Internal Dump project is entering prototyping phase, where a prototype of the actuation mechanism and the dump core will be produced. While testing the dump core in beam operation is impossible before installation, the prototype can be used to test manufacturing processes and the cooling performance to refine the simulations. Based on the feedback from the prototypes, several dumps will be manufactured. Two dumps will be installed in the Proton Synchrotron and the others will be kept as spares. The new dumps are foreseen to be installed in 2020.

References

[1] About CERN. Retrieved 21 May 2017, from https://home.cern/about

[2] Convention for the establishment of a European organization for nuclear research: Paris, 1st July, 1953. Retrieved 28 October 2017, from https://cds.cern.ch/record/480837?ln=en

[3] Fabjan, C. (ed.), Taylor, T. (ed.), Treille, D. (ed.) & Wenninger, H. (ed.) (2017). *Technology meets research: 60 years of CERN technology: selected highlights.* New Jersey, USA: World Scientific. 457 p. (Advanced series on directions in high energy physics, Vol. 27). ISBN: 978-981-4749-15-2 (ebook)

[4] Damerau, H. (ed.) et al. (2014). *LHC Injectors Upgrade, Technical Design Report, Vol. I: Protons.* Geneva, Switzerland: CERN. 613 p. (CERN report number CERN-ACC-2014-0337)

[5] Schmidt, R. (2006). Introduction to Machine Protection. In R. Schmidt (ed.), *Proceedings of the Joint International Accelerator School: Beam Loss and Accelerator Protection, Newport Beach, United States, 5-14 November 2014* (pp. 1-20). Geneva, Switzerland: CERN. DOI: https://doi.org/10.5170/CERN-2016-002.1

[6] Rossi, L. (ed.) & Brüning, O. (ed.) (2015). *The High Luminosity Large Hadron Collider: the new machine for illuminating the mysteries of Universe.* New Jersey, USA: World Scientific. 393 p. (Advanced series on directions in high energy physics, Vol. 24). ISBN: 978-981-4678-14-8 (print)

[7] Mobs, E. (2016). The CERN accelerator complex. Complexe des accélérateurs du CERN. Retrieved 30 September 2017, from https://cds.cern.ch/record/2225847?ln=en

[8] Gilardoni, S. (ed.) & Manglunki, D. (ed.) (2011). *Fifty years of the CERN Proton Synchrotron: Volume 1.* Geneva, Switzerland: CERN. 172 p. DOI: https://doi.org/10.5170/CERN-2011-004

[9] Mokhov, N.V. & Cerutti, F. (2016). Beam–Material Interactions. In R. Schmidt (ed.), *Proceedings of the Joint International Accelerator School: Beam Loss and Accelerator Protection, Newport Beach, United States, 5-14 November 2014* (pp. 83-110). Geneva, Switzerland: CERN. DOI: https://doi.org/10.5170/CERN-2016-002.83

[10] Bertarelli, A. (2016). Beam-Induced Damage Mechanisms and their Calculation. In R. Schmidt (ed.), *Proceedings of the Joint International Accelerator School: Beam Loss and Accelerator Protection, Newport Beach, United States, 5-14 November 2014* (pp. 159-227). Geneva, Switzerland: CERN. DOI: https://doi.org/10.5170/CERN-2016-002.159

[11] Nuiry, F.-X. & Romagnoli, G. (2017). *PS Ring Internal Dumps Functional Specifications.* CERN EDMS Document number 1582110 Rev. 2.1

[12] Patrignani, C. et al. (2016). Review of Particle Physics, 2016-2017. *Chinese Physics C.* Vol. 40:10. pp. 1-1808. DOI: https://doi.org/10.1088/1674-1137/40/10/100001. ISSN 1674-1137 (print). Available at: https://pdg.lbl.gov/

[13] Tecker, F. (2014). Longitudinal Beam Dynamics. In W. Herr (ed.), *Proceedings of the CAS-CERN Accelerator School: Advanced Accelerator Physics, Trondheim, Norway, 19–29 August 2013* (pp. 1-21). Geneva, Switzerland: CERN. DOI: https://doi.org/10.5170/CERN-2014-009.1

[14] Steerenberg, R. & Cotte, D. (2017). *PS Beam spot sizes for the design of New internal Beam dumps.* CERN EDMS Document number 1612293 Rev. 1.3

[15] Kain, V. (2016). Beam Dynamics and Beam Losses – Circular Machines. In R. Schmidt (ed.), *Proceedings of the Joint International Accelerator School: Beam Loss and Accelerator Protection, Newport Beach, United States, 5-14 November 2014* (pp. 21-38). Geneva, Switzerland: CERN. DOI: https://doi.org/10.5170/CERN-2016-002.21

[16] Battistoni, G. et al. (2007). The FLUKA code: description and benchmarking. *AIP Conference Proceedings.* Vol. 896:1. pp. 31-49. DOI: https://doi.org/10.1063/1.2720455. ISSN 0094-243X (print)

[17] Nuiry, F.-X., Romagnoli, G., Esala, J. & Briz, J. (2017). *Upgrade of the PS Internal Dump in the Framework of the LHC Injectors Upgrade Project.* CERN EDMS Document number 1845424 v.0.2

[18] Martin, B.R. & Shaw, G. (2013). *Particle Physics.* 3rd ed. West Sussex, United Kingdom: John Wiley & Sons. 464 p. (Manchester Physics Series). ISBN: 978-1-118-68166-4 (ebook)

[19] Mokhov, N.V. (2013). Beam–Materials Interactions. *Reviews of Accelerator Science and Technology.* Vol. 6. pp. 275-290. DOI: https://doi.org/10.1142/S1793626813300132. ISSN 1793-8058 (online)

[20] International Atomic Energy Agency. (1994). *Atomic and Plasma–Material Interaction Data for Fusion, Vol. 5.* Vienna, Austria: IAEA. 268 p. (Supplement to the Journal Nuclear Fusion).

[21] Ammigan, K. et al. (2017). The RaDIATE High-Energy Proton Materials Irradiation Experiment at the Brookhaven Linac Isotope Producer Facility, In, *Proceedings of IPAC2017, Copenhagen, Denmark* (pp. 3593-3596). ISBN 978-3-95450-182-3 (online)

[22] Fabritsiev, S.A., Zinkle, S.J. & Singh, B.N. (1996). Evaluation of copper alloys for fusion reactor divertor and first wall components. *Journal of Nuclear Materials.* Vol. 233-237:1. pp. 127-137. DOI: https://doi.org/10.1016/S0022-3115(96)00091-8. ISSN 0022-3115 (online)

[23] Li, M., Sokolov, M.A. & Zinkle, S.J. (2009). Tensile and fracture toughness properties of neutron-irradiated CuCrZr. *Journal of Nuclear Materials.* Vol. 393:1.

pp. 36-46. DOI: https://doi.org/10.1016/j.jnucmat.2009.05.003. ISSN 0022-3115 (online)

[24] Barabash, V.R., Kalinin, G.M., Fabritsiev, S.A. & Zinkle, S.J. (2011). Specification of CuCrZr alloy properties after various thermo-mechanical treatments and design allowables including neutron irradiation effects. *Journal of Nuclear Materials*. Vol. 417:1-3. pp. 904-907. DOI: https://doi.org/10.1016/j.jnucmat.2010.12.158. ISSN 0022-3115

[25] Simmons, J.H.W. (1965). *Radiation Damage in Graphite*. 1st ed. Pergamon Press. 243 p.

[26] Zazula, J. (1995). From particle cascade simulations (FLUKA) to finite element heat transfer and structural deformation analyses (ANSYS). In G.R. Stevenson (ed.), *2nd Workshop on Simulating Accelerator Radiation Environments: SARE-2, CERN, Geneva, Switzerland, 9-11 Oct 1995* (pp. 26-34). Geneva, Switzerland: CERN.

[27] ANSYS, Inc. (2016). *ANSYS Documentation for release 17.1*

[28] Christensen, R. (2006). A Comparative Evaluation of Three Isotropic, Two Property Failure Theories. *Journal of Applied Mechanics*. Vol. 73:5. pp. 852-859. DOI: https://doi.org/10.1115/1.2173007. ISSN 1528-9036 (online)

[29] Lewis, D.M. & Steinbach, C. (1974). *Efficiencies of internal dump targets in the CPS.* CERN Report CERN/MPS/OP 74-4

[30] Szeless, B. (1975). *PS internal dump.* CERN Report MPS/ML/Tech. Note 75-2

[31] Steinbach, C. (1985). *Utilisation des cibles dump 47 et 48.* CERN Report SR14 18.09.1985

[32] Kozłowska, W. (2015). *PS Internal Dump in the FLUKA Monte Carlo simulations.* CERN EDMS Document number 1403161 v.1

[33] Romagnoli, G., Nuiry, F.-X. & Polzin, T. (2017). *Proposed Design of the New PS Internal Dump based on EDMS 1582110 v.1.0.* CERN EDMS Document number 1771786 v.0.2

[34] Nuiry, F.-X. (2017). *Preliminary Thermo-Mechanical Simulations Applied to the New PS Internal Dump.* CERN EDMS Document number 1539643 v.0.2

[35] Madhusudana, C.V. (2014). *Thermal Contact Conductance*. Springer Cham. 260 p. (Mechanical Engineering Series). ISBN 978-3-319-01276-6 (ebook)

[36] Perillo-Marcone, A. (2017). *Bonding between cuprous materials and stainless steel tubes.* CERN EDMS Document number 1838803 v.2

[37] Guglielmini, P. (2006). *Corrosion phenomena in demineralized water cooling circuits.* CERN EDMS Document number 718814 v.1

[38] Rios-Rodriguez, P. (2017). *TIDVG#4 in LSS1 For Operation in 2017 & 2018.* CERN EDMS Document number 1720876 Rev. 1.0

[39] SGL Group. *SGL SIGRAFINE® R7550 Data Sheet and measurements.*

[40] Beitel, G. (1971). The Use of Graphite in High and Ultrahigh Vacuum: A Review. *Journal of Vacuum Science and Technology.* Vol. 8:5. pp. 647-657. DOI: https://doi.org/10.1116/1.1316380. ISSN 0022-5355

[41] De Segovia, J.L. (1999). Physics of outgassing. In S. Turner (ed.), *Proceedings of the CAS-CERN Accelerator School: Vacuum Technology, Snekersten, Denmark, 28 May - 3 Jun 1999* (pp. 99-109). Geneva, Switzerland: CERN. DOI: https://doi.org/10.5170/CERN-1999-005.99

[42] Jousten, K. (1999). Thermal outgassing. In S. Turner (ed.), *Proceedings of the CAS-CERN Accelerator School: Vacuum Technology, Snekersten, Denmark, 28 May - 3 Jun 1999* (pp. 111-125). Geneva, Switzerland: CERN. DOI: https://doi.org/10.5170/CERN-1999-005.111

[43] Singh, B.N., Li, M., Stubbins, J.F. & Johansen, B.S. (2005). *Creep-fatigue deformation behaviour of OFHC-copper and CuCrZr alloy with different heat treatments and with and without neutron irradiation.* 55 p. (Denmark. Forskningscenter Risoe. Risoe-R; No. 1528(EN)). ISBN: 87-550-3465-9 (print)

[44] Roberts, J.G. (2007). *Determination of fatigue characteristics of NBG18 graphite.* (Doctoral dissertation, North-West University, South Africa). Retrieved from https://hdl.handle.net/10394/1894

[45] *VDI Heat Atlas.* (2010). Springer-Verlag Berlin Heidelberg. 1585 p. (VDI-Buch). ISBN: 978-3-540-79999-3 (ebook)

[46] Granta Design. (2017). CES Selector 2017 Update 1 Version: 17.2.0 (material database software).

[47] JAHM Software, Inc. (2017). MPDB v8.35 (material database software).

[48] Yovanovich, M. (2005). Four decades of research on thermal contact, gap, and joint resistance in microelectronics. *IEEE Transactions on Components and Packaging Technologies.* Vol. 28:2. pp. 182-206. DOI: https://doi.org/10.1109/TCAPT.2005.848483. ISSN 1557-9972 (online)

[49] Marotta, E.E., Mazzuca, S.J. & Norley, J. (2005). Thermal joint conductance for flexible graphite materials: analytical and experimental study. *IEEE Transactions on Components and Packaging Technologies.* Vol. 28:1. pp. 102-110. DOI: https://doi.org/10.1109/TCAPT.2004.843153. ISSN 1557-9972 (online)

[50] Bahrami, M., Culham, J., Yovanovich, M. & Schneider, G. (2006). Review of Thermal Joint Resistance Models for Nonconforming Rough Surfaces. *Applied Mechanics Reviews.* Vol. 59:1. pp. 1-12. DOI: https://doi.org/10.1115/1.2110231. ISSN 2379-0407 (online)

List of Appendices

Appendix 1: Material Data Tables

The temperature dependent material data implemented in ANSYS is presented in Table 1.1 for Graphite R7550, in Table 1.2 for CuCrZr and in Table 1.3 for stainless steel 316L. At temperatures between the specified temperature points the values are interpolated linearly from the nearest temperatures. At temperatures outside the specified temperature range the value at the closest temperature is used. The references for the materials properties are shown in the tables.

Graphite exhibits nonlinear elastic behavior [25] but in ANSYS a linear elastic material model is used. A measured dynamic Young's modulus of 12.8 GPa is used instead of a measured static Young's modulus of 8.5 GPa. The dynamic Young's modulus at elevated temperatures is scaled by the relative change of Young's modulus with temperature.

The material data for the multilinear isotropic hardening model implemented in ANSYS for CuCrZr and stainless steel 316L is presented in Table 1.4.

Table 1.1. Material data implemented in ANSYS for graphite SGL SIGRAFINE® R7550.

Density		Thermal conductivity		Specific heat		Mean coefficient of thermal expansion		Young's modulus and Poisson's ratio		
T [°C]	ρ [kg/m^3]	T [°C]	λ [W/(m K)]	T [°C]	c_p [J/(kg K)]	T [°C]	α [ppm/K]	T [°C]	E [GPa]	ν [-]
20	1830	21	107	−23.15	568.1	$T_{\text{ref}} = 22$ °C		22	12.8	0.14
250	1825	228	88	26.85	721.4	200	4	233.5	13.151	0.14
500	1818	429	73	76.85	875	300	4.2	426.7	13.543	0.14
750	1810	611	65	126.85	1025.8	400	4.35	502.4	13.756	0.14
1000	1802	824	56	176.85	1155.5	500	4.5	696.9	14.397	0.14
1250	1794	1005	52	226.85	1268.6	600	4.65	874.4	15.161	0.14
1500	1785	1265	48	276.85	1352.3	700	4.77	1002.3	15.818	0.14
1750	1776	1491	44	326.85	1423.5	800	4.88	1143.3	16.671	0.14
2000	1767	1741	43	376.85	1490.5	900	4.99	1271.2	17.63	0.14
2250	1758	2000	43	426.85	1549.1	1000	5.09	1374.3	18.376	0.14
2500	1748			476.85	1599.3	1100	5.17	1444.8	18.837	0.14
				526.85	1645.4	1200	5.25	1502.2	19.139	0.14
				576.85	1683.1	1300	5.34	1551.8	19.317	0.14
				626.85	1712.4	1400	5.42	1587	19.371	0.14
				676.85	1737.5	1500	5.5	1618.4	19.389	0.14
				726.85	1762.6	1600	5.57	1656.2	19.336	0.14
				826.85	1808.7	1700	5.64	1694.1	19.265	0.14
				926.85	1854.7	1800	5.71	1758.1	19.142	0.14
				1026.85	1892.4	1900	5.78	1837.7	19.036	0.14
				1126.85	1925.9	2000	5.85	1900.4	18.877	0.14
				1226.85	1959.4	2100	5.92			
				1326.85	1984.5	2200	5.99			
				1526.85	2034.8	2300	6.06			
				1726.85	2076.6	2400	6.13			
				1926.85	2110.1	2500	6.2			
				2126.85	2139.4					
				2326.85	2160.4					
				2526.85	2181.3					

References:

Material data sheets for SGL SIGRAFINE® R7550 and similar fine-grain graphites from the manufacturer SGL Group and specific measurements performed for CERN.

Table 1.2. Material data implemented in ANSYS for CuCrZr.

Density		Thermal conductivity		Specific heat		Mean coefficient of thermal expansion		Young's modulus and Poisson's ratio		
T [°C]	ρ [kg/m^3]	T [°C]	λ [W/(m K)]	T [°C]	c_p [J/(kg K)]	T [°C]	α [ppm/K]	T [°C]	E [GPa]	ν [-]
24.8	8898	26	330	50	418	T_{ref} = 20 °C		25	137	0.34
		50	330	100	424	24.1	15.2	100	134	0.34
		80	331	200	435	26.1	15.6	200	129	0.34
		100	331	300	443	28.1	16.2	300	116	0.34
		150	333	400	451	30.1	16.7			
		200	335	500	455	32.1	17			
		250	334	600	460	34.1	17.2			
		300	334	700	467	36.1	17.4			
		350	333	800	486	38.1	17.5			
		400	331			40.1	17.6			
		500	325			42.1	17.7			
		600	324			44.1	17.7			
		700	312			46.1	17.8			
		800	295			48.1	17.8			
						50.1	17.9			
						76.1	18			
						100.1	18.1			
						150.1	18.2			
						200.1	18.3			
						300.1	18.4			
						400.1	18.5			
						500.1	18.7			
						600.1	18.9			
						700.1	19.2			
						800.1	19.6			

References:

Characterization campaign of 3D forged CuCrZr at CERN in 2017.

Thermal conductivity calculated from thermal diffusivity and reduced slightly to be in line with the reported value at room temperature.

Poisson's ratio from CES Selector 2017 material database software. Material: Copper-Cr-Zr alloy, C18100, wp (h.c. copper). [46]

Table 1.3. Material data implemented in ANSYS for stainless steel 316L.

Density		Thermal conductivity		Specific heat		Mean coefficient of thermal expansion		Young's modulus and Poisson's ratio		
T [°C]	ρ [kg/m^3]	T [°C]	λ [W/(m K)]	T [°C]	c_p [J/(kg K)]	T [°C]	α [ppm/K]	T [°C]	E [GPa]	ν [-]
0	7977	0	12.9	0	475	T_{ref} = 22 °C		0	195.4	0.3
20	7969	20	13.2	20	485	0	16	20	193.8	0.3
50	7957	50	13.7	50	500	20	16.1	50	191.3	0.3
100	7937	100	14.5	100	521	50	16.3	100	187.1	0.3
150	7916	150	15.2	150	539	100	16.4	150	182.9	0.3
200	7895	200	16	200	554	150	16.6	200	178.7	0.3
250	7873	250	16.7	250	566	200	16.8	250	174.6	0.3
300	7851	300	17.4	300	577	250	17	300	170.4	0.3
						300	17.2			

References:

MPDB v.8.35 material database software. Material: 316L (UNS S31603). [47]

Table 1.4. Material data for the multilinear isotropic hardening model implemented in ANSYS for CuCrZr and stainless steel 316L.

	CuCrZr			Stainless steel 316L		
Temperature [°C]	Yield strength [MPa]	Tensile strength [MPa]	Elongation at break [%]	Yield strength [MPa]	Tensile strength [MPa]	Elongation at break [%]
25	282	400	34	297	602	54
100	275	367	29	249	532	49
200	259	335	28	224	481	42
300	230	294	34	198	462	36
400	207	260	41	185	458	31

References:

Characterization campaign of 3D forged CuCrZr at CERN in 2017.

MPDB v.8.35 material database software. Material: 316L (UNS S31603). [47]

Appendix 2: Analytical Heat Transfer Coefficient Calculations

Heat transfer coefficient between cooling pipes and water

The heat transfer coefficient h_w from cooling pipe walls to water (at steady-state) is solved iteratively in the following steps: [45, pp. 693–699]

1. An inlet water temperature of $T_\mathrm{i} = 26\,^\circ\mathrm{C}$ and an estimated outlet water temperature of $T_\mathrm{o} = 36\,^\circ\mathrm{C}$ of the cooling circuit is specified.

2. Cooling system parameters are defined according the geometry presented in Figure 26. The cooling circuit in the dump core is divided into three parallel circuits. The inner diameter d_i of the pipe is 4 mm. Each circuit passes through the dump core four times: $4 \times 0.18\,\mathrm{m} = 0.72\,\mathrm{m}$. A longer pipe length $L = 3\,\mathrm{m}$ is selected for the calculations to account for the bends and other features in the pipes. Smooth pipes are assumed.

3. A mean flow velocity w is specified. A volumetric flow rate of $Q = 1.5\,\mathrm{l/min}$ has been measured in the cooling circuit of the current PS Internal Dump core. This value is used as a starting point. The mean flow velocity is calculated through the cross-sectional area A of three circuits with the equation

$$w = \frac{Q}{A} = \frac{Q}{3 \cdot \pi \cdot \left(\frac{d_\mathrm{i}}{2}\right)^2} = \frac{1.5\,\mathrm{l/min}}{3 \cdot \pi \cdot \left(\frac{4\,\mathrm{mm}}{2}\right)^2} = 0.66\,\mathrm{m/s} \tag{2.1}$$

4. An average water temperature $T_\mathrm{m} = (T_\mathrm{i} + T_\mathrm{o})/2$ is calculated. Properties of water at this temperature at 1 bar are read from a table [45, p. 154]. The properties are kinematic viscosity ν_visc, thermal conductivity λ, density ρ, specific heat c_p, and the Prandtl number Pr.

5. Reynolds number Re is calculated

$$Re = \frac{w \cdot d_\mathrm{i}}{\nu_\mathrm{visc}} \approx 3400 \tag{2.2}$$

6. The calculated Reynolds number is in the transition regime between laminar and turbulent flow ($2300 < Re < 10000$). The Nusselt number Nu in the transition regime is calculated with the equation

$$Nu = (1 - \gamma) Nu_{\mathrm{lam},2300} + \gamma Nu_{\mathrm{turb},10^4} \tag{2.3}$$

where γ is the intermittency factor ($\gamma = 0$ for fully laminar flow, $\gamma = 1$ for fully turbulent flow) defined as

$$\gamma = \frac{Re - 2300}{10^4 - 2300} \tag{2.4}$$

The laminar portion of the Nusselt number is calculated assuming a constant pipe wall temperature with the equations

$$Nu_{\mathrm{lam},2300} = \left[49.371 + \left(Nu_{\mathrm{lam},2,2300} - 0.7\right)^3 + Nu^3_{\mathrm{lam},3,2300}\right]^{1/3} \tag{2.5}$$

$$Nu_{\mathrm{lam},2,2300} = 1.615 \cdot \left(2300 \cdot Pr \cdot d_\mathrm{i}/L\right)^{1/3} \tag{2.6}$$

$$Nu_{\mathrm{lam},3,2300} = \left(\frac{2}{1 + 22 \cdot Pr}\right)^{1/6} \left(2300 \cdot Pr \cdot d_\mathrm{i}/L\right)^{1/2} \tag{2.7}$$

The turbulent portion of the Nusselt number is calculated assuming constant wall temperature or constant heat flux and smooth pipes with the equation

$$Nu_{\mathrm{turb},10^4} = \frac{(0.0308/8) \cdot 10^4 \cdot Pr}{1 + 12.7\sqrt{0.0308/8}(Pr^{2/3} - 1)} \left[1 + \left(d_\mathrm{i}/L\right)^{2/3}\right] \tag{2.8}$$

The equation is valid for $0.1 \leq Pr \leq 1000$ and $d_\mathrm{i}/L \leq 1$.

7. The heat transfer coefficient h_w can now be calculated with the equation

$$h_\mathrm{w} = \frac{Nu \cdot \lambda}{d_\mathrm{i}} \tag{2.9}$$

8. The previous steps were calculated using an estimated outlet temperature. Since the power deposited in the dump core is known from FLUKA, a more accurate outlet temperature can be calculated. The energy deposition depends on the beam type but for steady-state simulations a LHC 25ns HL-LHC beam pulse every 3.6 s is used (See Section 6.5). The energy deposited per pulse is known to be 8068 J (see Table 7). A heating power P_heat of 2240 W is obtained by dividing the energy by the pulse period 3.6 s. Since at steady-state the input power is equal to the output power, a new outlet temperature is calculated using the equation

$$P = c_p \cdot \rho \cdot Q \cdot \Delta T = c_p \cdot \rho \cdot A \cdot w \cdot \left(T_\mathrm{o} - T_\mathrm{i}\right) \tag{2.10}$$

$$T_\mathrm{o} = \frac{P_\mathrm{heat}}{c_p \cdot \rho \cdot w \cdot 3 \cdot \pi \cdot \left(\frac{d_\mathrm{i}}{2}\right)^2} \tag{2.11}$$

9. A new iteration step is started using the calculated new T_o. The steps are repeated until the heat transfer coefficient h_w converges.

With the aforementioned steps, a heat transfer coefficient of 2928 W/(m^2 K) and an outlet water temperature of 48 °C can be calculated. The iteration steps are presented in Table 2.1.

Table 2.1. Cooling pipe to water heat transfer coefficient calculations.

			1. Iteration	2. Iteration	3. Iteration
Cooling system parameters					
Inlet water temperature	T_i	[°C]	26	26	26
Outlet water temperature	T_o	[°C]	36	47.58	47.58
Number of circuits		[-]	3	3	3
Pipe inner diameter	d_i	[m]	0.004	0.004	0.004
Pipe length	L	[m]	3	3	3
Mean flow velocity	w	[m/s]	0.663	0.663	0.663
Heating power	P_heat	[W]	2247	2247	2247
Water properties					
Average temperature	T_m	[°C]	31	36.77	36.79
Kinematic viscosity	$\nu_\mathrm{visc}(T_\mathrm{m})$	$\times\ 10^{-6}$ [m^2/s]	0.7854	0.6243	0.6243
Thermal conductivity	$\lambda(T_\mathrm{m})$	[W/(m K)]	0.6164	0.6243	0.6244
Density	$\rho(T_\mathrm{m})$	[kg/m^3]	995.3	993.4	993.4
Specific heat	$c_p(T_\mathrm{m})$	[J/(kg K)]	4180	4179	4179
Prandtl number	$Pr(T_\mathrm{m})$	[-]	5.301	4.657	4.655
Reynolds number	Re	[-]	3377	3789	3791
Calculation of the Nusselt number					
Intermittency factor	γ	[-]	0.1399	0.1934	0.1936
$Nu_{\mathrm{lam},2,2300}$		[-]	4.091	3.918	3.918
$Nu_{\mathrm{lam},3,2300}$		[-]	2.045	1.958	1.957
$Nu_{\mathrm{lam},2300}$		[-]	4.593	4.485	4.484
$Nu_{\mathrm{turb},10^4}$		[-]	80.90	75.31	75.30
Nusselt number	Nu	[-]	15.27	18.20	18.21
Results					
Outlet water temperature	T_o	[°C]	47.58	47.58	**47.58**
Heat transfer coefficient	h_w	[W/(m^2 K)]	2458	2922.9	**2925**

Thermal contact conductance between CuCrZr and graphite

The thermal contact conductance (TCC) h_s of the graphite to CuCrZr contact is calculated analytically using the Mikic equations. They are analytical formulas to calculate the contact conductances of two surfaces pressed together considering their surface asperities, contact pressure and material properties.

The deformation of the asperities is elastic until a certain load value is exceeded, after which the deformation is plastic. The tendency for plastic deformation is represented by the plasticity index ψ. For values greater than one the deformation is plastic even under light loads and for values below 0.7 the deformation is elastic even under heavy loads. The plasticity index is defined as [35]

$$\psi = \left(\frac{E'}{H}\right) m_\mathrm{r} \tag{2.12}$$

$$E' = 2\left(\frac{1-\nu_1^2}{E_1} + \frac{1-\nu_2^2}{E_2}\right)^{-1} \tag{2.13}$$

$$m_\mathrm{r} = \sqrt{m_1^2 + m_2^2} \tag{2.14}$$

where E' is the reduced modulus of elasticity depending on the Young's moduli E_i and Poisson's ratios ν_i of the materials in contact. H is the microhardness of the

softer material and m_r is effective mean absolute asperity slope depending on the mean absolute asperity slopes m_i of the two contacting surfaces. Gaussian distribution of profile heights and a contact in vacuum is assumed. [35]

The Mikic equations for calculating the TCC of elastic and plastic contacts are

$$\text{Elastic: } h_\mathrm{s} = 1.55 \left(\frac{\lambda' m_\mathrm{r}}{R_\mathrm{r}}\right) \left(\frac{\sqrt{2}P}{E' m_\mathrm{r}}\right)^{0.94} \tag{2.15}$$

$$\text{Plastic: } h_\mathrm{s} = 1.13 \left(\frac{\lambda' m_\mathrm{r}}{R_\mathrm{r}}\right) \left(\frac{P}{H}\right)^{0.94} \tag{2.16}$$

$$\lambda' = \frac{2\lambda_1 \lambda_2}{\lambda_1 + \lambda_2} \tag{2.17}$$

$$R_\mathrm{r} = \sqrt{R_{\mathrm{RMS},1}^2 + R_{\mathrm{RMS},2}^2} \tag{2.18}$$

where P is the contact pressure and λ' is the effective thermal conductivity depending the thermal conductivities λ_i of the materials in contact [35]. R_r is the effective RMS surface roughness depending on the RMS surface roughnesses $R_{\mathrm{RMS},i}$ of the surfaces in contact [48].

Additionally, for graphite to graphite contact an equation is found in [49]

$$\text{Graphite: } h_\mathrm{s} = 1.49 \left(\frac{\lambda' m_\mathrm{r}}{R_\mathrm{r}}\right) \left(\frac{2.3P}{E_\mathrm{g} m_\mathrm{r}}\right)^{0.935} \tag{2.19}$$

where E_g is the Young's modulus of graphite [49].

Calculations for contact pressure dependent equations for the thermal contact conductances are presented in Table 2.2. The TCCs are plotted with respect to pressure in Figure 2.1. A worst-case (rough surfaces, $R_\mathrm{a} = 12.5\,\mu\mathrm{m}$) and best case (smooth surfaces, $R_\mathrm{a} = 0.8\,\mu\mathrm{m}$) contact is studied with specified arithmetic mean roughnesses R_a. RMS roughness is related to the average roughness with the relation $R_\mathrm{RMS} = 1.25 R_\mathrm{a}$ [35, 50]. Since no data for the mean absolute asperity slopes of the surfaces is available, an approximated correlation of $m_i = 0.076(R_{\mathrm{RMS},i} \times 10^6)^{0.52}$ is used [50]. The material values at room temperature are taken from Table 3.

The hardness of CuCrZr is taken as HV 110 and multiplied by 9.807 to obtain a hardness of 1080 MPa in SI units. CES Selector 2017 material database software lists values of HV 113–138 for CuCrZr (material: Copper-Cr-Zr alloy, C18100, wp (h.c. copper). [46]

The hardness of Graphite is $\mathrm{HR}_{5/100}$ 90 according to the data sheet [39]. An estimated Vickers hardness of HV 40 is taken instead from CES Selector 2017 software (material: Graphite (1.82)) [46]. The Vickers hardness number is multiplied by 9.807 to obtain a hardness of 392 MPa in SI units.

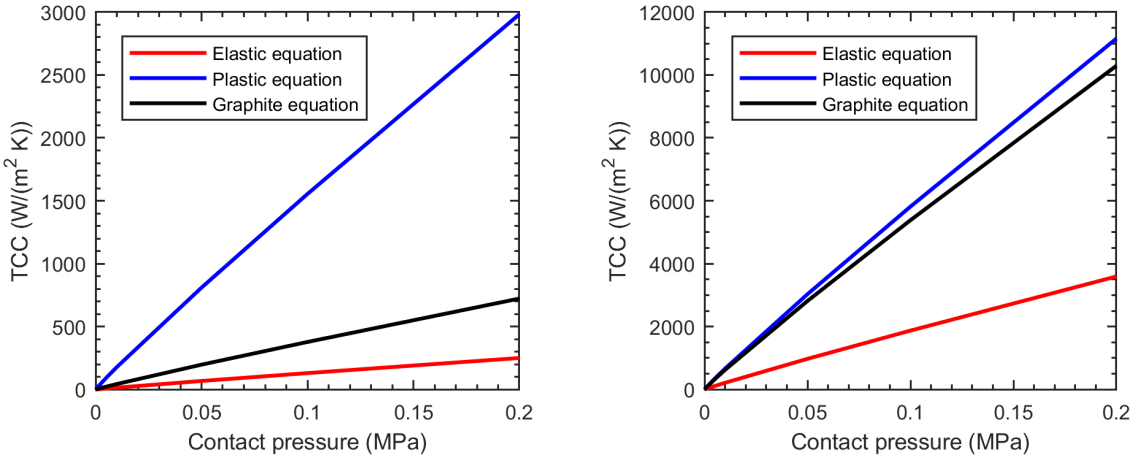

(a) Rough contact. (b) Smooth contact.

Figure 2.1. Analytically calculated thermal contact conductance with respect to contact pressure.

Table 2.2. Analytical thermal contact conductance calculations for pressed contacts.

			Rough contact		Smooth contact	
			Graphite	CuCrZr	Graphite	CuCrZr
Inputs						
Arithmetic mean surface roughness	R_a	[µm]	12.5	12.5	0.8	0.8
RMS surface roughness	R_{RMS}	[µm]	15.6	15.6	1.0	1.0
Mean absolute asperity slope	m	[rad]	0.317	0.317	0.076	0.076
Young's modulus	E	[GPa]	137	12.8	137	12.8
Poisson's ratio	ν	[-]	0.34	0.14	0.34	0.14
Thermal conductivity	λ	[W/(m K)]	330	107	330	117
Microhardness	H	[MPa]	1080	392	1080	392
Calculated parameters						
Reduced Young's modulus	E'	[GPa]	24.1		24.1	
Effective mean absolute asperity slope	m_r	[rad]	0.449		0.0107	
Plasticity index	ψ	[-]	27.6		6.6	
Effective thermal conductivity	λ'	[W/(m K)]	162		162	
Effective RMS surface roughness	R_r	[µm]	22.1		1.41	
Analytical thermal contact conductances						
TCC (elastic equation)	h_s	[W/(m^2 K)]	$2.61 \times 10^{-3} P^{0.94}$		$3.74 \times 10^{-2} P^{0.94}$	
TCC (plastic equation)	h_s	[W/(m^2 K)]	$3.10 \times 10^{-3} P^{0.94}$		$1.16 \times 10^{-1} P^{0.94}$	
TCC (graphite equation)	h_s	[W/(m^2 K)]	$7.99 \times 10^{-3} P^{0.935}$		$1.14 \times 10^{-3} P^{0.935}$	

Appendix 3: ANSYS APDL Commands

The following ANSYS APDL scripts were used to perform the simulations of the dumping of one pulse of the HL–LHC beam. The scripts are inserted as Commands in ANSYS Workbench in the Transient Thermal and Transient Structural modules.

Thermal Simulation

```
!-----Element definition-----

/prep7

*set,nlayers,30                 ! Number of layers
*set,mtid,191                   ! Shell body material id
et,mtid,131                     ! Element type SHELL131
keyo,mtid,3,1                   ! 0=quadratic, 1=linear temp distribution
keyo,mtid,4,nlayers             ! Assigns nlayers layers through the thickness
keyo,mtid,6,0                   ! 0 = paint option off
sectype,mtid,SHELL
*do,i,1,nlayers                 ! Command is repeated for every layer
secdata,5e-6,mtid,0             ! Setting layer thickness
*enddo
secoffset,bottom                ! Shell offset

fini
/solu

!-----Setting beam and simulation parameters-----

np=2.4e13                       ! Intensity
pulseperiod=3.6                 ! Pulse period

MaxSubsPulse=1                  ! Substes
MinSubsPulse=1
MaxSubsCool=30
MinSubsCool=20
MaxSubsWave=100
MinSubsWave=30
MaxSubsAvg=10
MinSubsAvg=10

*set,scale_length,1e-2
pcharge=1.602176487e-19
*set,scale_edensity,1e9*pcharge*np*1e6
*set,loadsteps,40               ! Number of load steps (and FLUKA files)
*set,stepsize,1.5e-4            ! Time step size
*set,scale_avg,stepsize/pulseperiod ! Scaling factor for averaged heat generation

!-----Coupling SHELL131 to Solids------

ALLSEL
cmsel,s,interface               ! interface = named selection containing
esln                            ! the faces on Shell/Solid interface
*get,num,node,,count
nn=0
*do,i,1,num
nn=ndnext(nn)
CE,i,0,nn,TEMP,-1,nn,TBOT,1      ! Sets TEMP = TBOT
*enddo
ALLSEL

!-----Creating the load tables for the "fine" FLUKA binning (shell)-----

FILENAME1 = 'D:\PSDump\FLUKA\ps-HL_27'
!FILENAME1 = '\\rsm170\RSMTEMP\ps-HL_27'
TABLENAME1 = 'load_table1'
*dim,bins,array,3,4
*set,NSKIP,8
*sread,header,FILENAME1,,,,,NSKIP
```

```
bins(1,1)=valchr(strsub(header(1,3),25,12))
bins(2,1)=valchr(strsub(header(1,4),25,12))
bins(3,1)=valchr(strsub(header(1,5),25,12))
bins(1,3)=valchr(strsub(header(1,3),56,6))
bins(2,3)=valchr(strsub(header(1,4),56,6))
bins(3,3)=valchr(strsub(header(1,5),56,6))
bins(1,4)=valchr(strsub(header(1,3),69,11))
bins(2,4)=valchr(strsub(header(1,4),69,11))
bins(3,4)=valchr(strsub(header(1,5),69,11))
*set,nx1,bins(1,3)
*set,ny1,bins(2,3)
*set,nz1,bins(3,3)
*set,x1,bins(1,1)*scale_length
*set,y1,bins(2,1)*scale_length
*set,z1,bins(3,1)*scale_length
*set,dx,bins(1,4)*scale_length
*set,dy,bins(2,4)*scale_length
*set,dz,bins(3,4)*scale_length
*dim,fine1,array,nx1,ny1,nz1,x,y,z,12

*do,i,1,ny1
*dim,fine1_%i%,table,nx1,1,nz1,x,y,z,12
*dim,fine1avg_%i%,table,nx1,1,nz1,x,y,z,12
*enddo

*do,K,1,nz1
        zz = z1 + (K-1)*dz + 0.5*dz
        *do,J,1,ny1
        *set,fine1_%J%(0,0,K),zz
        *set,fine1avg_%J%(0,0,K),zz
        *enddo
*enddo
*do,I,1,nx1
        xx = x1 + (I-1)*dx + 0.5*dx
        *do,J,1,ny1
        *set,fine1_%J%(I,0,1),xx
        *set,fine1avg_%J%(I,0,1),xx
        *enddo
*enddo
*do,J,1,ny1
        yy = y1 + (J-1)*dy + 0.5*dy
        *set,fine1_%J%(0,1,1),yy
        *set,fine1avg_%J%(0,1,1),yy
*enddo

!-----Creating the load tables for the "ff" FLUKA binning (shell)-----

FILENAME2 = 'D:\PSDump\FLUKA\ps-HL_26'
!FILENAME2 = '\\rsm170\RSMTEMP\ps-HL_26'
TABLENAME2 = 'load_table2'
*dim,bins,array,3,4
*set,NSKIP,8
*sread,header,FILENAME2,,,,,NSKIP
bins(1,1)=valchr(strsub(header(1,3),25,12))
bins(2,1)=valchr(strsub(header(1,4),25,12))
bins(3,1)=valchr(strsub(header(1,5),25,12))
bins(1,3)=valchr(strsub(header(1,3),56,6))
bins(2,3)=valchr(strsub(header(1,4),56,6))
bins(3,3)=valchr(strsub(header(1,5),56,6))
bins(1,4)=valchr(strsub(header(1,3),69,11))
bins(2,4)=valchr(strsub(header(1,4),69,11))
bins(3,4)=valchr(strsub(header(1,5),69,11))
*set,nx2,bins(1,3)
*set,ny2,bins(2,3)
*set,nz2,bins(3,3)
*set,x1,bins(1,1)*scale_length
*set,y1,bins(2,1)*scale_length
*set,z1,bins(3,1)*scale_length
*set,dx,bins(1,4)*scale_length
*set,dy,bins(2,4)*scale_length
*set,dz,bins(3,4)*scale_length
*dim,fine2,array,nx2,ny2,nz2,x,y,z,13
```

```
134
135 *do,i,1,ny2
136 *dim,fine2_%i%,table,nx2,1,nz2,x,y,z,13
137 *dim,fine2avg_%i%,table,nx2,1,nz2,x,y,z,13
138 *enddo
139
140 *do,K,1,nz2
141         zz = z1 + (K-1)*dz + 0.5*dz
142         *do,J,1,ny2
143         *set,fine2_%J%(0,0,K),zz
144         *set,fine2avg_%J%(0,0,K),zz
145         *enddo
146 *enddo
147 *do,I,1,nx2
148         xx = x1 + (I-1)*dx + 0.5*dx
149         *do,J,1,ny2
150         *set,fine2_%J%(I,0,1),xx
151         *set,fine2avg_%J%(I,0,1),xx
152         *enddo
153 *enddo
154 *do,J,1,ny2
155         yy = y1 + (J-1)*dy + 0.5*dy
156         *set,fine2_%J%(0,1,1),yy
157         *set,fine2avg_%J%(0,1,1),yy
158 *enddo
159
160 !-----Creating the load tables for the "fc" FLUKA binning (shell)-----
161
162 FILENAME3 = 'D:\PSDump\FLUKA\ps-HL_25'
163 !FILENAME3 = '\\rsm170\RSMTEMP\ps-HL_25'
164 TABLENAME3 = 'load_table3'
165 *dim,bins,array,3,4
166 *set,NSKIP,8
167 *sread,header,FILENAME3,,,,,NSKIP
168 bins(1,1)=valchr(strsub(header(1,3),25,12))
169 bins(2,1)=valchr(strsub(header(1,4),25,12))
170 bins(3,1)=valchr(strsub(header(1,5),25,12))
171 bins(1,3)=valchr(strsub(header(1,3),56,6))
172 bins(2,3)=valchr(strsub(header(1,4),56,6))
173 bins(3,3)=valchr(strsub(header(1,5),56,6))
174 bins(1,4)=valchr(strsub(header(1,3),69,11))
175 bins(2,4)=valchr(strsub(header(1,4),69,11))
176 bins(3,4)=valchr(strsub(header(1,5),69,11))
177 *set,nx3,bins(1,3)
178 *set,ny3,bins(2,3)
179 *set,nz3,bins(3,3)
180 *set,x1,bins(1,1)*scale_length
181 *set,y1,bins(2,1)*scale_length
182 *set,z1,bins(3,1)*scale_length
183 *set,dx,bins(1,4)*scale_length
184 *set,dy,bins(2,4)*scale_length
185 *set,dz,bins(3,4)*scale_length
186 *dim,fine3,array,nx3,ny3,nz3,x,y,z,4
187
188 *do,i,1,ny3
189 *dim,fine3_%i%,table,nx3,1,nz3,x,y,z,14
190 *dim,fine3avg_%i%,table,nx3,1,nz3,x,y,z,14
191 *enddo
192
193 *do,K,1,nz3
194         zz = z1 + (K-1)*dz + 0.5*dz
195         *do,J,1,ny3
196         *set,fine3_%J%(0,0,K),zz
197         *set,fine3avg_%J%(0,0,K),zz
198         *enddo
199 *enddo
200 *do,I,1,nx3
201         xx = x1 + (I-1)*dx + 0.5*dx
202         *do,J,1,ny3
203         *set,fine3_%J%(I,0,1),xx
204         *set,fine3avg_%J%(I,0,1),xx
205         *enddo
```

```
206 *enddo
207 *do,J,1,ny3
208         yy = y1 + (J-1)*dy + 0.5*dy
209         *set,fine3_%J%(0,1,1),yy
210         *set,fine3avg_%J%(0,1,1),yy
211 *enddo
212
213 !-----Creating the load tables for the "Coarse" FLUKA binning (3D)-----
214
215 FILENAME4 = 'D:\PSDump\FLUKA\ps-HL_29'
216 !FILENAME4 = '\\rsm170\RSMTEMP\ps-HL_29'
217 TABLENAME4 = 'load_table4'
218 *dim,bins,array,3,4
219 *set,NSKIP,8
220 *sread,header,FILENAME4,,,,,NSKIP
221 bins(1,1)=valchr(strsub(header(1,3),25,12))
222 bins(2,1)=valchr(strsub(header(1,4),25,12))
223 bins(3,1)=valchr(strsub(header(1,5),25,12))
224 bins(1,3)=valchr(strsub(header(1,3),56,6))
225 bins(2,3)=valchr(strsub(header(1,4),56,6))
226 bins(3,3)=valchr(strsub(header(1,5),56,6))
227 bins(1,4)=valchr(strsub(header(1,3),69,11))
228 bins(2,4)=valchr(strsub(header(1,4),69,11))
229 bins(3,4)=valchr(strsub(header(1,5),69,11))
230 *set,nx4,bins(1,3)
231 *set,ny4,bins(2,3)
232 *set,nz4,bins(3,3)
233 *set,x1,bins(1,1)*scale_length
234 *set,y1,bins(2,1)*scale_length
235 *set,z1,bins(3,1)*scale_length
236 *set,dx,bins(1,4)*scale_length
237 *set,dy,bins(2,4)*scale_length
238 *set,dz,bins(3,4)*scale_length
239 *dim,%TABLENAME4%,table,nx4,ny4,nz4,x,y,z,12
240 *dim,%TABLENAME4%d,table,nx4,ny4,nz4,x,y,z,21
241 *dim,%TABLENAME4%u,table,nx4,ny4,nz4,x,y,z,22
242 *set,NSKIP,8
243
244 *do,K,1,nz4
245         zz = z1 + (K-1)*dz + 0.5*dz
246         *set,%TABLENAME4%(0,0,K),zz
247         *set,%TABLENAME4%d(0,0,K),zz
248         *set,%TABLENAME4%u(0,0,K),zz
249 *enddo
250 *do,I,1,nx4
251         xx = x1 + (I-1)*dx + 0.5*dx
252         *set,%TABLENAME4%(I,0,1),xx
253         *set,%TABLENAME4%d(I,0,1),xx
254         *set,%TABLENAME4%u(I,0,1),xx
255 *enddo
256 *do,J,1,ny4
257         yy = y1 + (J-1)*dy + 0.5*dy
258         *set,%TABLENAME4%(0,J,1),yy
259         *set,%TABLENAME4%d(0,J,1),yy
260         *set,%TABLENAME4%u(0,J,1),yy
261 *enddo
262
263 *dim,load_table4_W,table,nx4,ny4,nz4,x,y,z,12
264 *dim,load_table4_avg,table,nx4,ny4,nz4,x,y,z,12
265 *TOPER,load_table4_avg,load_table4,add,load_table4,1,0,0
266
267 *dim,load_table4d_W,table,nx4,ny4,nz4,x,y,z,21
268 *dim,load_table4d_avg,table,nx4,ny4,nz4,x,y,z,21
269 *TOPER,load_table4d_avg,load_table4d,add,load_table4d,1,0,0
270
271 *dim,load_table4u_W,table,nx4,ny4,nz4,x,y,z,22
272 *dim,load_table4u_avg,table,nx4,ny4,nz4,x,y,z,22
273 *TOPER,load_table4u_avg,load_table4u,add,load_table4u,1,0,0
274
275 !-----Creating the load tables for the "Intermediate" FLUKA binning (3D)-----
276
277 FILENAME5 = 'D:\PSDump\FLUKA\ps-HL_28'
```

```
!FILENAME5 = '\\rsm170\RSMTEMP\ps-HL_28'
TABLENAME5 = 'load_table5'
*dim,bins,array,3,4
*set,NSKIP,8
*sread,header,FILENAME5,,,,,NSKIP
bins(1,1)=valchr(strsub(header(1,3),25,12))
bins(2,1)=valchr(strsub(header(1,4),25,12))
bins(3,1)=valchr(strsub(header(1,5),25,12))
bins(1,3)=valchr(strsub(header(1,3),56,6))
bins(2,3)=valchr(strsub(header(1,4),56,6))
bins(3,3)=valchr(strsub(header(1,5),56,6))
bins(1,4)=valchr(strsub(header(1,3),69,11))
bins(2,4)=valchr(strsub(header(1,4),69,11))
bins(3,4)=valchr(strsub(header(1,5),69,11))
*set,nx5,bins(1,3)
*set,ny5,bins(2,3)
*set,nz5,bins(3,3)
*set,x1,bins(1,1)*scale_length
*set,y1,bins(2,1)*scale_length
*set,z1,bins(3,1)*scale_length
*set,dx,bins(1,4)*scale_length
*set,dy,bins(2,4)*scale_length
*set,dz,bins(3,4)*scale_length
*dim,%TABLENAME5%,table,nx5,ny5,nz5,x,y,z,12
*dim,%TABLENAME5%d,table,nx5,ny5,nz5,x,y,z,23
*dim,%TABLENAME5%u,table,nx5,ny5,nz5,x,y,z,24
*set,NSKIP,8

*do,K,1,nz5
        zz = z1 + (K-1)*dz + 0.5*dz
        *set,%TABLENAME5%(0,0,K),zz
        *set,%TABLENAME5%d(0,0,K),zz
        *set,%TABLENAME5%u(0,0,K),zz
*enddo
*do,I,1,nx5
        xx = x1 + (I-1)*dx + 0.5*dx
        *set,%TABLENAME5%(I,0,1),xx
        *set,%TABLENAME5%d(I,0,1),xx
        *set,%TABLENAME5%u(I,0,1),xx
*enddo
*do,J,1,ny5
        yy = y1 + (J-1)*dy + 0.5*dy
        *set,%TABLENAME5%(0,J,1),yy
        *set,%TABLENAME5%d(0,J,1),yy
        *set,%TABLENAME5%u(0,J,1),yy
*enddo

*dim,load_table5_W,table,nx5,ny5,nz5,x,y,z,12
*dim,load_table5_avg,table,nx5,ny5,nz5,x,y,z,12
*TOPER,load_table5_avg,load_table5,add,load_table5,1,0,0

*dim,load_table5d_W,table,nx5,ny5,nz5,x,y,z,23
*dim,load_table5d_avg,table,nx5,ny5,nz5,x,y,z,23
*TOPER,load_table5d_avg,load_table5d,add,load_table5d,1,0,0

*dim,load_table5u_W,table,nx5,ny5,nz5,x,y,z,24
*dim,load_table5u_avg,table,nx5,ny5,nz5,x,y,z,24
*TOPER,load_table5u_avg,load_table5u,add,load_table5u,1,0,0

!-----Creating the load tables for the "fs" FLUKA binning (shell)-----

FILENAME6 = 'D:\PSDump\FLUKA\ps-HL_24'
!FILENAME6 = '\\rsm170\RSMTEMP\ps-HL_24'
TABLENAME6 = 'load_table6'
*dim,bins,array,3,4
*set,NSKIP,8
*sread,header,FILENAME6,,,,,NSKIP
bins(1,1)=valchr(strsub(header(1,3),25,12))
bins(2,1)=valchr(strsub(header(1,4),25,12))
bins(3,1)=valchr(strsub(header(1,5),25,12))
bins(1,3)=valchr(strsub(header(1,3),56,6))
bins(2,3)=valchr(strsub(header(1,4),56,6))
```

```
bins(3,3)=valchr(strsub(header(1,5),56,6))
bins(1,4)=valchr(strsub(header(1,3),69,11))
bins(2,4)=valchr(strsub(header(1,4),69,11))
bins(3,4)=valchr(strsub(header(1,5),69,11))
*set,nx6,bins(1,3)
*set,ny6,bins(2,3)
*set,nz6,bins(3,3)
*set,x1,bins(1,1)*scale_length
*set,y1,bins(2,1)*scale_length
*set,z1,bins(3,1)*scale_length
*set,dx,bins(1,4)*scale_length
*set,dy,bins(2,4)*scale_length
*set,dz,bins(3,4)*scale_length
*dim,fine6,array,nx6,ny6,nz6,x,y,z,15

*do,i,1,ny6
*dim,fine6_%i%,table,nx6,1,nz6,x,y,z,15
*dim,fine6avg_%i%,table,nx6,1,nz6,x,y,z,15
*enddo

*do,K,1,nz6
        zz = z1 + (K-1)*dz + 0.5*dz
        *do,J,1,ny6
        *set,fine6_%J%(0,0,K),zz
        *set,fine6avg_%J%(0,0,K),zz
        *enddo
*enddo
*do,I,1,nx6
        xx = x1 + (I-1)*dx + 0.5*dx
        *do,J,1,ny6
        *set,fine6_%J%(I,0,1),xx
        *set,fine6avg_%J%(I,0,1),xx
        *enddo
*enddo
*do,J,1,ny6
        yy = y1 + (J-1)*dy + 0.5*dy
        *set,fine6_%J%(0,1,1),yy
        *set,fine6avg_%J%(0,1,1),yy
*enddo

!-----------------------------------------------------------
! Load application and solving
!-----------------------------------------------------------

*do,pulse,1,1           ! Iterate over number of pulses

!~~~~~~~~~~~~~~~~~~~~~~~~~~~~~~~~~~~~~~~~~~~~~~~~~~~~~~~~~~~
! 1. DUMPING ONE PULSE
!~~~~~~~~~~~~~~~~~~~~~~~~~~~~~~~~~~~~~~~~~~~~~~~~~~~~~~~~~~~

*do,i,1,loadsteps                       ! Loop over the loadsteps
TIME,(pulse-1)*pulseperiod+i*stepsize   ! Specify the end time of the load step

!-----Reading new load table for "fine" binning-----

*set,NSKIP,8+(i-1)*36011
*vread,fine1(1,1,1),FILENAME1,,,IJK,nx1,ny1,nz1,NSKIP
(5x,10E12.4)

*DO,J,1,ny1
        *DO,II,1,nx1
                *DO,K,1,nz1
                        *set,fine1_%J%(II,1,K),fine1(II,J,K)*scale_edensity
                *ENDDO
        *ENDDO
        *TOPER,fine1avg_%J%,fine1avg_%J%,add,fine1_%J%,1,scale_avg,0
*ENDDO

!-----Reading new load table for "ff" binning-----

*set,NSKIP,8+(i-1)*18011
*vread,fine2(1,1,1),FILENAME2,,,IJK,nx2,ny2,nz2,NSKIP
```

```
(5x,10E12.4)

*DO,J,1,ny2
        *DO,II,1,nx2
                *DO,K,1,nz2
                        *set,fine2_%J%(II,1,K),fine2(II,J,K)*scale_edensity
                *ENDDO
        *ENDDO
        *TOPER,fine2avg_%J%,fine2avg_%J%,add,fine2_%J%,1,scale_avg,0
*ENDDO

!-----Reading new load table for "fc" binning-----

*set,NSKIP,8+(i-1)*18011
*vread,fine3(1,1,1),FILENAME3,,,IJK,nx3,ny3,nz3,NSKIP
(5x,10E12.4)

*DO,J,1,ny3
        *DO,II,1,nx3
                *DO,K,1,nz3
                        *set,fine3_%J%(II,1,K),fine3(II,J,K)*scale_edensity
                *ENDDO
        *ENDDO
        *TOPER,fine3avg_%J%,fine3avg_%J%,add,fine3_%J%,1,scale_avg,0
*ENDDO

!-----Reading new load table for "coarse" binning-----

*set,NSKIP,8+(i-1)*121451
*vread,%TABLENAME4%(1,1,1),FILENAME4,,,IJK,nx4,ny4,nz4,NSKIP
(5x,10E12.4)
*vread,%TABLENAME4%d(1,1,1),FILENAME4,,,IJK,nx4,ny4,nz4,NSKIP
(5x,10E12.4)
*vread,%TABLENAME4%u(1,1,1),FILENAME4,,,IJK,nx4,ny4,nz4,NSKIP
(5x,10E12.4)

*TOPER,load_table4_W,load_table4,add,load_table4,scale_edensity,0,0
*TOPER,load_table4_avg,load_table4_avg,add,load_table4_W,1,scale_avg,0

*TOPER,load_table4d_W,load_table4d,add,load_table4d,scale_edensity,0,0
*TOPER,load_table4d_avg,load_table4d_avg,add,load_table4d_W,1,scale_avg,0

*TOPER,load_table4u_W,load_table4u,add,load_table4u,scale_edensity,0,0
*TOPER,load_table4u_avg,load_table4u_avg,add,load_table4u_W,1,scale_avg,0

!-----Reading new load table for "intermediate" binning-----

*set,NSKIP,8+(i-1)*44171
*vread,%TABLENAME5%(1,1,1),FILENAME5,,,IJK,nx5,ny5,nz5,NSKIP
(5x,10E12.4)
*vread,%TABLENAME5%d(1,1,1),FILENAME5,,,IJK,nx5,ny5,nz5,NSKIP
(5x,10E12.4)
*vread,%TABLENAME5%u(1,1,1),FILENAME5,,,IJK,nx5,ny5,nz5,NSKIP
(5x,10E12.4)

*TOPER,load_table5_W,load_table5,add,load_table5,scale_edensity,0,0
*TOPER,load_table5_avg,load_table5_avg,add,load_table5_W,1,scale_avg,0

*TOPER,load_table5d_W,load_table5d,add,load_table5d,scale_edensity,0,0
*TOPER,load_table5d_avg,load_table5d_avg,add,load_table5d_W,1,scale_avg,0

*TOPER,load_table5u_W,load_table5u,add,load_table5u,scale_edensity,0,0
*TOPER,load_table5u_avg,load_table5u_avg,add,load_table5u_W,1,scale_avg,0

!-----Reading new load table for "fs" binning-----

*set,NSKIP,8+(i-1)*18011
*vread,fine6(1,1,1),FILENAME6,,,IJK,nx6,ny6,nz6,NSKIP
(5x,10E12.4)

*DO,J,1,ny6
        *DO,II,1,nx6
```

```
                *DO,K,1,nz6
                        *set,fine6_%J%(II,1,K),fine6(II,J,K)*scale_edensity
                *ENDDO
        *ENDDO
        *TOPER,fine6avg_%J%,fine6avg_%J%,add,fine6_%J%,1,scale_avg,0
*ENDDO

!-----Applying the load tables-----

! fine FLUKA binning
ALLSEL
CMSEL,S,fineElem
BFE,all,hgen,1,%fine1_1%
BFE,all,hgen,2,%fine1_2%
BFE,all,hgen,3,%fine1_3%
BFE,all,hgen,4,%fine1_4%
BFE,all,hgen,5,%fine1_5%
BFE,all,hgen,6,%fine1_6%
BFE,all,hgen,7,%fine1_7%
BFE,all,hgen,8,%fine1_8%
BFE,all,hgen,9,%fine1_9%
BFE,all,hgen,10,%fine1_10%
BFE,all,hgen,11,%fine1_11%
BFE,all,hgen,12,%fine1_12%
BFE,all,hgen,13,%fine1_13%
BFE,all,hgen,14,%fine1_14%
BFE,all,hgen,15,%fine1_15%
BFE,all,hgen,16,%fine1_16%
BFE,all,hgen,17,%fine1_17%
BFE,all,hgen,18,%fine1_18%
BFE,all,hgen,19,%fine1_19%
BFE,all,hgen,20,%fine1_20%
BFE,all,hgen,21,%fine1_21%
BFE,all,hgen,22,%fine1_22%
BFE,all,hgen,23,%fine1_23%
BFE,all,hgen,24,%fine1_24%
BFE,all,hgen,25,%fine1_25%
BFE,all,hgen,26,%fine1_26%
BFE,all,hgen,27,%fine1_27%
BFE,all,hgen,28,%fine1_28%
BFE,all,hgen,29,%fine1_29%
BFE,all,hgen,30,%fine1_30%

! ff FLUKA binning
ALLSEL
CMSEL,S,ffElem
BFE,all,hgen,1,%fine2_1%
BFE,all,hgen,2,%fine2_2%
BFE,all,hgen,3,%fine2_3%
BFE,all,hgen,4,%fine2_4%
BFE,all,hgen,5,%fine2_5%
BFE,all,hgen,6,%fine2_6%
BFE,all,hgen,7,%fine2_7%
BFE,all,hgen,8,%fine2_8%
BFE,all,hgen,9,%fine2_9%
BFE,all,hgen,10,%fine2_10%
BFE,all,hgen,11,%fine2_11%
BFE,all,hgen,12,%fine2_12%
BFE,all,hgen,13,%fine2_13%
BFE,all,hgen,14,%fine2_14%
BFE,all,hgen,15,%fine2_15%
BFE,all,hgen,16,%fine2_16%
BFE,all,hgen,17,%fine2_17%
BFE,all,hgen,18,%fine2_18%
BFE,all,hgen,19,%fine2_19%
BFE,all,hgen,20,%fine2_20%
BFE,all,hgen,21,%fine2_21%
BFE,all,hgen,22,%fine2_22%
BFE,all,hgen,23,%fine2_23%
BFE,all,hgen,24,%fine2_24%
BFE,all,hgen,25,%fine2_25%
BFE,all,hgen,26,%fine2_26%
```

```
BFE,all,hgen,27,%fine2_27%
BFE,all,hgen,28,%fine2_28%
BFE,all,hgen,29,%fine2_29%
BFE,all,hgen,30,%fine2_30%

! fc FLUKA binning
ALLSEL
CMSEL,S,fcElem
BFE,all,hgen,1,%fine3_1%
BFE,all,hgen,2,%fine3_2%
BFE,all,hgen,3,%fine3_3%
BFE,all,hgen,4,%fine3_4%
BFE,all,hgen,5,%fine3_5%
BFE,all,hgen,6,%fine3_6%
BFE,all,hgen,7,%fine3_7%
BFE,all,hgen,8,%fine3_8%
BFE,all,hgen,9,%fine3_9%
BFE,all,hgen,10,%fine3_10%
BFE,all,hgen,11,%fine3_11%
BFE,all,hgen,12,%fine3_12%
BFE,all,hgen,13,%fine3_13%
BFE,all,hgen,14,%fine3_14%
BFE,all,hgen,15,%fine3_15%
BFE,all,hgen,16,%fine3_16%
BFE,all,hgen,17,%fine3_17%
BFE,all,hgen,18,%fine3_18%
BFE,all,hgen,19,%fine3_19%
BFE,all,hgen,20,%fine3_20%
BFE,all,hgen,21,%fine3_21%
BFE,all,hgen,22,%fine3_22%
BFE,all,hgen,23,%fine3_23%
BFE,all,hgen,24,%fine3_24%
BFE,all,hgen,25,%fine3_25%
BFE,all,hgen,26,%fine3_26%
BFE,all,hgen,27,%fine3_27%
BFE,all,hgen,28,%fine3_28%
BFE,all,hgen,29,%fine3_29%
BFE,all,hgen,30,%fine3_30%

! Coarse FLUKA binning
ALLSEL
CMSEL,S,coaNodes,NODE
BF,all,hgen,%load_table4_W%
ALLSEL
CMSEL,S,coaNodesDown,NODE
BF,all,hgen,%load_table4d_W%
ALLSEL
CMSEL,S,coaNodesUp,NODE
BF,all,hgen,%load_table4u_W%
ALLSEL

! Intermediate FLUKA binning
ALLSEL
CMSEL,S,intNodes,NODE
BF,all,hgen,%load_table5_W%
ALLSEL
CMSEL,S,intNodesDown,NODE
BF,all,hgen,%load_table5d_W%
ALLSEL
CMSEL,S,intNodesUp,NODE
BF,all,hgen,%load_table5u_W%
ALLSEL

! fs FLUKA binning
ALLSEL
CMSEL,S,fsElem
BFE,all,hgen,1,%fine6_1%
BFE,all,hgen,2,%fine6_2%
BFE,all,hgen,3,%fine6_3%
BFE,all,hgen,4,%fine6_4%
BFE,all,hgen,5,%fine6_5%
BFE,all,hgen,6,%fine6_6%
```

```
BFE,all,hgen,7,%fine6_7%
BFE,all,hgen,8,%fine6_8%
BFE,all,hgen,9,%fine6_9%
BFE,all,hgen,10,%fine6_10%
BFE,all,hgen,11,%fine6_11%
BFE,all,hgen,12,%fine6_12%
BFE,all,hgen,13,%fine6_13%
BFE,all,hgen,14,%fine6_14%
BFE,all,hgen,15,%fine6_15%
BFE,all,hgen,16,%fine6_16%
BFE,all,hgen,17,%fine6_17%
BFE,all,hgen,18,%fine6_18%
BFE,all,hgen,19,%fine6_19%
BFE,all,hgen,20,%fine6_20%
BFE,all,hgen,21,%fine6_21%
BFE,all,hgen,22,%fine6_22%
BFE,all,hgen,23,%fine6_23%
BFE,all,hgen,24,%fine6_24%
BFE,all,hgen,25,%fine6_25%
BFE,all,hgen,26,%fine6_26%
BFE,all,hgen,27,%fine6_27%
BFE,all,hgen,28,%fine6_28%
BFE,all,hgen,29,%fine6_29%
BFE,all,hgen,30,%fine6_30%
ALLSEL

! Solving the model
ALLSEL
NSUBST,MaxSubsPulse,MaxSubsPulse,MinSubsPulse,OFF
SOLVE

*enddo

!~~~~~~~~~~~~~~~~~~~~~~~~~~~~~~~~~~~~~~~~~~~~~~~~~~~~~~~~~~~~
! 2. COOLDOWN
!~~~~~~~~~~~~~~~~~~~~~~~~~~~~~~~~~~~~~~~~~~~~~~~~~~~~~~~~~~~~

*if,1,EQ,1,THEN ! To activate change to *if,1,EQ,1,THEN

TIME,(pulse-1)*pulseperiod+1/25*pulseperiod
ALLSEL
BFDELE,all,all
BFEDELE,all,all
NSUBST,MaxSubsCool,MaxSubsCool,MinSubsCool,OFF
SOLVE

TIME,pulse*pulseperiod
ALLSEL
BFDELE,all,all
BFEDELE,all,all
NSUBST,MaxSubsCool,MaxSubsCool,MinSubsCool,OFF
SOLVE

*endif
*enddo
```

Structural Simulation

```
!-----Element definition-----

/prep7

*set,nlayers,30                 ! Number of layers
*set,mtid,191                   ! Shell body material id
et,mtid,181                     ! Element type SHELL181
keyo,mtid,1,0                   ! 0=Bending and membrane stifness 1=Membrane stiffness only
keyo,mtid,3,0                   ! 0=reduced integration 2=Full integration
keyo,mtid,8,1                   ! 1=Store data for TOP & BOTTOM of every layer
sectype,mtid,SHELL
*do,i,1,nlayers                 ! Command is repeated for every layer
secdata,150e-6/nlayers,mtid,0   ! Setting layer thickness
*enddo
```

```
15 secoffset,bottom                ! Shell offset
16
17 fini
18 /solu
19
20 !-----Importing temperatures and solving the model-----
21
22 FILENAME='\\rsm170\RSMTEMP\psdhl' !Path of the thermal result file
23 !FILENAME='D:\PSDump\RES\psdhl'   !Path of the thermal result file
24
25 *set,loadsteps,40               ! Number of load steps (equal to thermal)
26 *set,stepsize,1.5e-4            ! Time step size
27 *set,npulse,1                   ! Number of pulses
28 *set,pulseperiod,3.6            ! Pulse period
29
30 MaxSubsPulse=1                  ! Substeps
31 MinSubsPulse=1
32 MaxSubsCool=1
33 MinSubsCool=1
34
35 ALLSEL
36 *DO,j,1,loadsteps
37         *set,nexttime,(pulse-1)*pulseperiod+j*stepsize
38         LDREAD,TEMP,,,nexttime,0,FILENAME,RTH
39         TIME,nexttime
40         KBC,0                   ! ramped
41         NSUBST,1,MaxSubsPulse,MinSubsPulse,OFF
42         SOLVE                   !Solve for each substep
43 *ENDDO
```